DISSERTATION

AEROSOL PARAMETERIZATIONS IN SPACE-BASED NEAR-INFRARED RETRIEVALS OF CARBON DIOXIDE

Submitted by

Robert Roland Nelson

Department of Atmospheric Science

In partial fulfillment of the requirements

For the Degree of Doctor of Philosophy

Colorado State University

Fort Collins, Colorado

Spring 2019

Doctoral Committee:

Advisor: Christian D. Kummerow
Co-Advisor: Christopher W. O'Dell

A. Scott Denning
Jeffrey R. Pierce
Jennifer A. Hoeting

ABSTRACT

AEROSOL PARAMETERIZATIONS IN SPACE-BASED NEAR-INFRARED RETRIEVALS OF CARBON DIOXIDE

The scattering effects of clouds and aerosols are one of the primary sources of error when making space-based measurements of carbon dioxide. This work describes multiple investigations into optimizing how aerosols are parameterized in retrievals of the column-averaged dry-air mole fraction of carbon dioxide ($X_{\mathrm{CO_2}}$) performed on near-infrared measurements of reflected sunlight from the Orbiting Carbon Observatory-2 (OCO-2). The primary goal is to enhance both the precision and accuracy of the $X_{\mathrm{CO_2}}$ measurements by improving the way aerosols are handled in the NASA Atmospheric CO_2 Observations from Space (ACOS) retrieval algorithm. Two studies were performed: one on using better informed aerosol priors in the retrieval and another on reducing the complexity of the aerosol parameterization. It was found that using ancillary aerosol information from the Goddard Earth Observing System Model, Version 5 (GEOS-5) resulted in a small improvement against multiple validation sources but that the improvements were restricted by the accuracy and limitations of the model. Implementing simplified aerosol parameterizations that allowed for the retrieval of fewer parameters sometimes resulted in small improvements in $X_{\mathrm{CO_2}}$, but further work is needed to determine the optimal way to handle the scattering effects of clouds and aerosols in near-infrared measurements of $X_{\mathrm{CO_2}}$. With several multi-million dollar space-based greenhouse gas measurement missions scheduled and in development, the massive amount of measurements will be an incredible boon to the global scientific community, but only if the precision and accuracy of the data are sufficient.

ACKNOWLEDGEMENTS

These six and a half years in Colorado have been an amazing experience for me both academically and professionally. It would not have happened if Chris O'Dell had not been willing to take a chance on someone who did not know the difference between a passive and active instrument. I am forever indebted to Chris for taking me on as his first student and mentoring me through both a master's and doctoral degree here at Colorado State University (CSU). It was a learning process for the both of us but, in the end, a success.

I would like to thank Dr. Chris Kummerow for acting as my academic advisor for the past few years and for providing advice on how to navigate both graduate school and the professional world. Additionally, I wish to thank Jamie Schmidt, Sarah Tisdale, Holli Knutson, and the entire past and present CSU and Cooperative Institute for Research in the Atmosphere (CIRA) administrative staff for their endless patience and knowledge.

I am extremely grateful to have worked with an outstanding set of individuals during my time here. Thank you to Tommy Taylor for always being available to chat about research and for fostering my new cycling addiction, thanks to Andy Manaster and Emily Bell for being great officemates, and thanks to Andy Schuh, Heather Cronk, David Baker, Natalie Tourville, Hannakaisa Lindqvist, Michael Cheeseman, and Greg McGarragh for the thoughtful discussions and mentorship. Additionally, my committee has been patient and supportive throughout my graduate program. Thank you Chris O'Dell, Chris Kummerow, Scott Denning, Jeff Pierce, and Jennifer Hoeting.

The OCO-2 team at the NASA Jet Propulsion Laboratory (JPL) has been extremely supportive of my work over the years and I could not have asked for a more friendly, enthusiastic group of scientists to call my co-workers and friends. I thank them all, especially Annmarie Eldering and Dave Crisp, for acting as mentors as I continue to grow as a young scientist.

Finally, I would like to thank my friends and family. My loving girlfriend, Ariel, has supported me this past year as I worked to finish my studies. The number of friends I have made in Colorado is too large to list here, but thank you all for being a part of my life. I am fortunate to have a mother who, despite us not agreeing on many things, has always been supportive.

This work was supported by NASA JPL grant number 5359007.

TABLE OF CONTENTS

ABSTRACT ii
ACKNOWLEDGEMENTS iii
LIST OF TABLES vii
LIST OF FIGURES viii

Chapter 1 Introduction 1
1.1 Greenhouse Gases and Climate 1
1.2 Understanding Carbon Dioxide Absorption Mechanisms 3
1.3 The Importance of Carbon Dioxide Measurements 6
1.3.1 The Orbiting Carbon Observatory-2 11
1.3.2 Future Missions 13
1.4 Retrieving Carbon Dioxide from Satellites 15
1.4.1 Optimal Estimation 17
1.5 Cloud and Aerosol Errors in X_{CO_2} Retrievals 20
1.5.1 Scattering Effects of Clouds and Aerosols 21
1.5.2 Screening Methods 22
1.6 Aerosol Parameterizations in Near-Infrared Measurements of GHGs 24
1.6.1 ACOS Aerosol Parameterization 25
1.7 Outline 26

Chapter 2 The Impact of Improved Aerosol Priors on Near-Infrared Measurements of Carbon Dioxide 29
2.1 ACOS Aerosol Parameterization 29
2.2 Validation Datasets 30
2.2.1 TCCON and AERONET Validation Dataset 30
2.2.2 Model Validation Dataset 32
2.3 Filtering and Bias Correction 32
2.4 Modeled Aerosol Priors 34
2.4.1 Types and Optical Depths 37
2.4.2 Types and Gaussian Fits 37
2.4.3 Types and Scale Factors 37
2.4.4 Aerosol Prior Uncertainties 39
2.5 Results 42
2.5.1 TCCON Validation Results 42
2.5.2 Model Validation Results 44
2.6 Conclusions 54

Chapter 3 Simplified Aerosol Parameterizations in Near-Infrared Retrievals of Carbon Dioxide 57
3.1 Simplified Aerosol Parameterizations 57
3.2 Validation Datasets 61

3.2.1 Synthetic Dataset 61
3.2.2 TCCON Validation Dataset 63
3.3 Synthetic OCO-2 Observation Results 64
3.4 OCO-2 Observation Results 70
3.4.1 Non-Scattering Retrieval 71
3.4.2 One Layer Model 71
3.4.3 Two Layer Model 72
3.5 Retrieving Aerosol Properties 74
3.6 Conclusions 75

Chapter 4 Conclusions and Discussion 78
4.1 Summary of Results 78
4.2 The Future of Space-Based Measurements of CO_2 80

Bibliography 82

Appendix A High-Accuracy Measurements of Total Column Water Vapor from the Orbiting Carbon Observatory-2 107
A.1 The Importance of Water Vapor 107
A.2 Theoretical Basis 108
A.3 Data 113
A.4 Validation 118
A.5 Water Vapor Conclusions 125

LIST OF TABLES

1.1 Spectral Band Properties 16
1.2 ACOS B8 State Vector Elements 19

2.1 TCCON Site Details 31
2.2 Aerosol Prior Uncertainties 41

3.1 Simplified Aerosol Parameterization Setups 61
3.2 Synthetic OCO-2 Observation Setup 62

A.1 OCO-2 Prior TCWV Validation: Simulations 112
A.2 OCO-2 Retrieved TCWV Validation: Simulations 112
A.3 OCO-2 TCWV Validation Statistics 117
A.4 ECMWF TCWV Validation Statistics 121
A.5 MERRA-2 TCWV Validation Statistics 121

LIST OF FIGURES

1.1 Global Average Surface Temperature Change 2
1.2 Carbon Budget Diagram 4
1.3 Uncertainty Reduction from GOSAT 5
1.4 WMO GAW Network 7
1.5 Rayner and O'Brien $X_{\mathrm{CO_2}}$ Uncertainty 8
1.6 GOSAT $X_{\mathrm{CO_2}}$ 10
1.7 OCO-2 Footprints and Radiances 12
1.8 OCO-2 Observation Modes 13
1.9 GHG Satellite Timeline 14
1.10 Light Path Conceptual Diagram 15
1.11 Measured Radiances 16
1.12 Non-Scattering $X_{\mathrm{CO_2}}$ Retrieval Errors 21
1.13 OCO-2 and MODIS Cloud Screening Agreement 24
1.14 ACOS B8 Prior Aerosol Profiles 27

2.1 TCCON and AERONET site map 31
2.2 AERONET AOD Comparisons 35
2.3 MERRA-2 and GEOS-5 Primary Aerosol Type Map 36
2.4 GEOS-5 Aerosol Gaussians 38
2.5 GEOS-5 Aerosol Prior TCCON Results 43
2.6 GEOS-5 Types and AODs with Low Uncertainty Model Comparison Results 45
2.7 GEOS-5 Types and AODs with Low Uncertainty Model Comparison Results, Difference Maps 46
2.8 MERRA-2 and GEOS-5 Prior AOD Maps 49
2.9 MERRA-2 and GEOS-5 Retrieved AOD Maps 51
2.10 GEOS-5 Aerosol Type Test Map 52
2.11 Retrieved Stratospheric Aerosol Impact on $X_{\mathrm{CO_2}}$ 53
2.12 Prior AOD Uncertainty Impact on $X_{\mathrm{CO_2}}$ 55

3.1 Frankenberg Aerosol Averaging Kernels 58
3.2 Two Layer Model Diagram 60
3.3 Simplified Aerosol Parameterization Synthetic $X_{\mathrm{CO_2}}$ Results 65
3.4 Simplified Aerosol Parameterization Synthetic $X_{\mathrm{CO_2}}$ Results, Sulfate Only 68
3.5 Simplified Aerosol Parameterization Synthetic $X_{\mathrm{CO_2}}$ Results, Iterations 69
3.6 Simplified Aerosol Parameterization $X_{\mathrm{CO_2}}$ Compared to TCCON 70
3.7 Two Layer Model Difference Maps Against Model Validation 73
3.8 Effective Radius Retrieval Results 75

A.1 OCO-2 H_2O Spectra 109
A.2 Simulated OCO-2 Prior and Retrieved TCWV Heatmaps 111
A.3 OCO-2 TCWV RMSD as a Function of Distance from SuomiNet 115
A.4 OCO-2 TCWV Validation Source Map 118

A.5 OCO-2 TCWV Validation Heatmap 119
A.6 ECMWF TCWV Validation Heatmap 120
A.7 MERRA-2 TCWV Validation Heatmap 122
A.8 TCWV Validation RMSDs 123
A.9 OCO-2 AMSR2 TCWV Percent Difference Map 124

Chapter 1

Introduction

1.1 Greenhouse Gases and Climate

The radiative balance of Earth is governed by a number of factors. One such factor is the composition of the atmosphere. Despite representing a relatively small fraction of the total number of molecules in the air, gases such as carbon dioxide (CO_2) and methane (CH_4) have the ability to trap a substantial amount of heat [1, 2]. This results in Earth being warmer than if there were no atmosphere at all, which has been likened to a "greenhouse effect."

Since the industrial revolution, humans have directly contributed to a substantial rise in the concentration of greenhouse gases (GHGs) in Earth's atmosphere [2]. This, in turn, has resulted in an imbalance in the radiative budget of Earth, the direct consequence of which is rising global temperatures. The atmospheric concentration of CO_2 has increased by around 46% from pre-industrial times to 2017, from 280 parts per million (ppm) to around 405 ppm, with humans emitting about 37 billion tons of CO_2 to the atmosphere each year [3]. This has happened primarily because of the burning of fossil fuels, biomass burning, cement production, and land use change. As of 2011, anthropogenic CO_2 represents 1.82 Wm^{-2} of radiative forcing [2]. However, this forcing and the year-to-year CO_2 concentrations are not constant and the mechanisms behind what drives this variability are not fully understood.

Our current trajectory is likely to result in an increase in natural disasters such as heat waves, droughts, and floods [2]. There have been a number of attempts by the global community to try and limit future emissions, including the Kyoto Protocol, Copenhagen Accord, and more recently the Paris Agreement. However, how humans will act in the future is difficult to predict. This means there is considerable uncertainty surrounding the future of Earth's climate and the world must be prepared for a wide range of potential scenarios. Figure 1.1 shows future warming predictions, based on the Intergovernmental Panel on Climate Change (IPCC) Representative Concentration Pathways (RCPs).

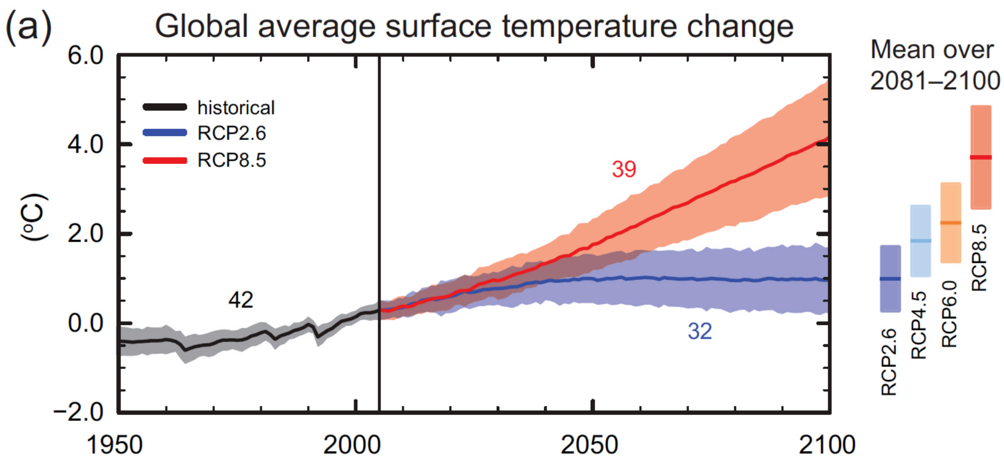

Figure 1.1: Coupled Model Intercomparison Project Phase 5 (CMIP5) multi-model simulated time series from 1950 to 2100 for the change in global annual mean surface temperature relative to 1986-2005. Time series of projections and a measure of uncertainty (shading) are shown for scenarios RCP2.6 (blue) and RCP8.5 (red). Black (grey shading) is the modeled historical evolution using historical reconstructed forcings. The mean and associated uncertainties averaged over 2081-2100 are given for all RCP scenarios as colored vertical bars. The numbers of CMIP5 models used to calculate the multi-model mean is indicated. Taken from [2].

In an attempt to limit GHG emissions, the United Nations Framework Convention on Climate Change (UNFCCC) was created in 1994. The first major effort to address global emissions was the UNFCCC's Kyoto Protocol, adopted in 1997. This committed numerous countries to limit their emissions to “a level that would prevent dangerous anthropogenic interference with the climate system." However, one of the largest emitters, the United States of America, did not ratify the Protocol. Since then, there has been an amendment (the Doha Amendment) to extend those commitments that has been signed by a fraction of the original countries. At the 21st session of the Conference of the Parties (COP21) of the UNFCCC in 2015, the Paris Agreement was implemented in order to limit the increase in globally averaged temperatures to less than 2 degrees Celsius (°C) above pre-industrial levels. Each party at COP21, representing more than 200 countries, defined and submitted their own nationally determined contribution (NDC) and agreed to report their GHG emissions to the UNFCCC. These NDCs represent each party's emission reduction goals and contributions to the global effort to stay under 2 °C.

1.2 Understanding Carbon Dioxide Absorption Mechanisms

Carbon dioxide measurements represent one of the primary sources of information that the scientific community has at its disposal to study the current state of Earth's atmosphere as well as predict potential climate scenarios. CO_2 measurements are fed into carbon transport inversion models, which are used to track the gas as it is transported around the atmosphere and subsequently estimate carbon sources and sinks and their associated uncertainty. That is, where CO_2 is emitted and absorbed on the surface of the earth, as CO_2 does not have sources or sinks in the atmosphere itself. The natural carbon cycle is driven primarily by photosynthesis and respiration by plants [4] and the solubility of CO_2 in the ocean [5]. The magnitude of these natural processes is much larger than that of the anthropogenically emitted CO_2 but on average the natural sources emit about the same as the natural sinks, creating a balance. Although many of the processes that govern the lifecycle of CO_2 are known, the exact locations, magnitudes, and mechanisms behind these sources and sinks remains unknown. About half of the anthropogenically emitted CO_2 remains in the atmosphere. The other half is absorbed by net carbon sinks. Figure 1.2 shows that for 2007-2016 it is estimated that 10.7 gigatons of carbon (GtC, where one GtC is equivalent to 3.67 gigatons of CO_2) per year are emitted into the atmosphere from fossil fuel burning, industry, and land-use change. About 4.7 GtC yr^{-1} of this stays in the atmosphere, while the land sink absorbs around 3.0 GtC yr^{-1} and the ocean sink absorbs 2.4 GtC yr^{-1}.

The partition between oceanic and terrestrial sinks is uncertain and can vary significantly from year to year. Carbon sources and sinks on land, specifically, likely vary more than the oceanic sink and thus have an even higher degree of uncertainty associated with them [7]. Several factors influence the atmosphere-land CO_2 exchange including CO_2 fertilization, changes in nitrogen deposition, forest regrowth, deforestation, and changes in forest management. Currently, it is thought that the European and North American carbon sinks are the result of forest regrowth in abandoned

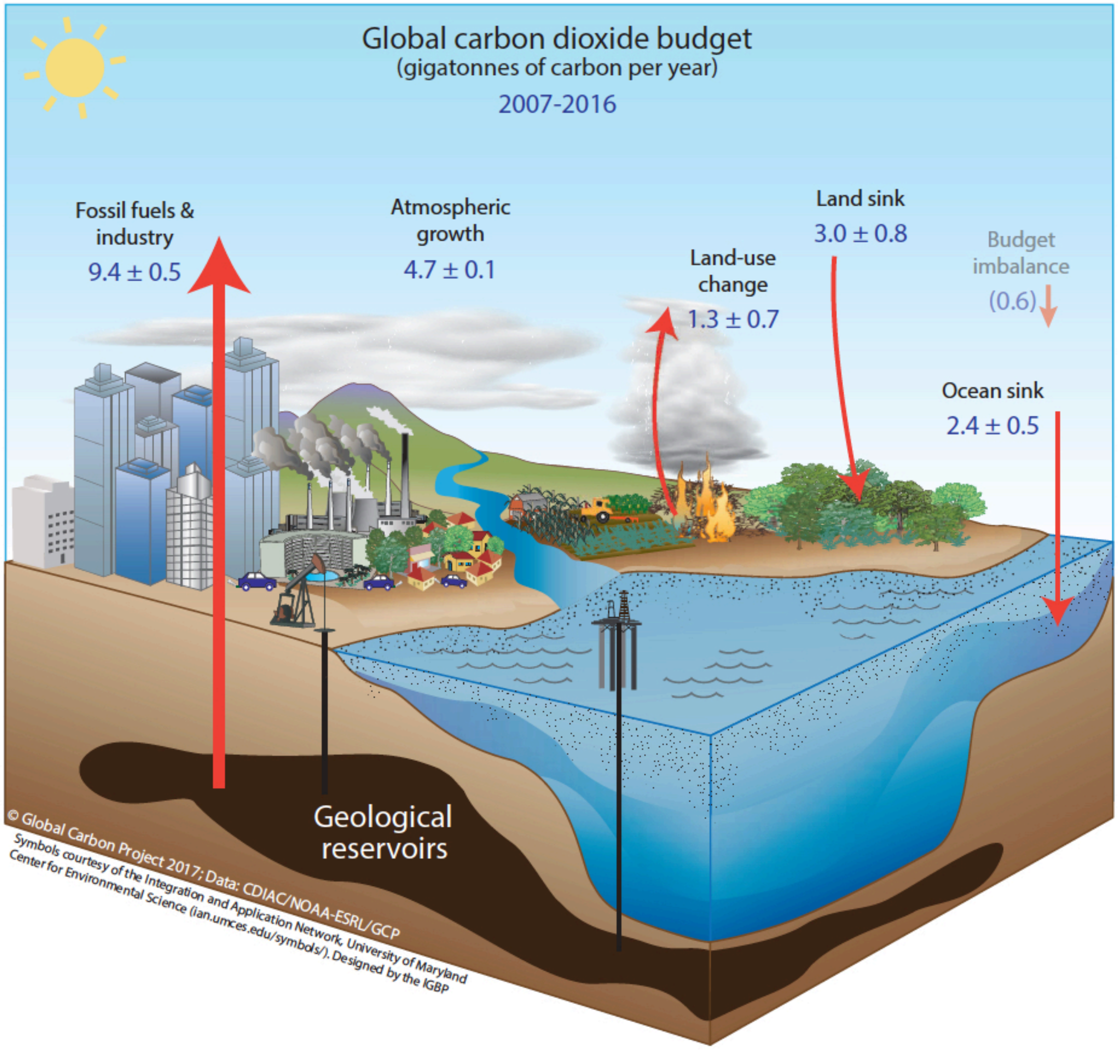

Figure 1.2: Carbon budget for 2007-2016. Fluxes are given in GtC yr^{-1} with 1-sigma uncertainties. Taken from [6].

lands, a decrease in forest harvest, boreal warming, and CO_2 and NO_2 fertilization. There is some evidence that the tropics are influenced by CO_2 fertilization as well [2]. However, there remains considerable uncertainty in estimates of the current flux patterns and, importantly, the exact mechanisms behind these sources and sinks and how they will act in the future. CO_2 measurements help reduce the uncertainty surrounding these sources and sinks because carbon transport inversion models become more accurate when they ingest accurate and precise CO_2 measurements [8–11]. Space-based measurements, specifically, provide vastly more global coverage than the currently available network of ground-based measurements. Figure 1.3 demonstrates the expected reduction in uncertainty for eight-day-mean CO_2 surface fluxes when space-based measurements of the column-averaged dry-air mole fraction of carbon dioxide ($X_{\mathrm{CO_2}}$) from the Japanese Greenhouse gas Observing SATellite (GOSAT; [12]) measurements are ingested.

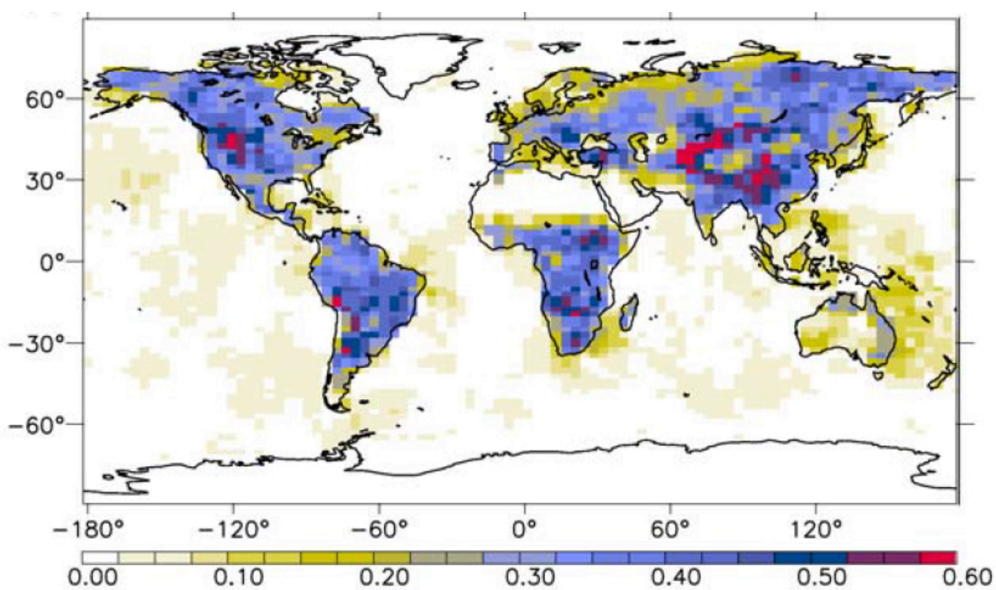

Figure 1.3: Expected uncertainty reduction provided by GOSAT for the estimation of eight-day-mean CO_2 surface fluxes. Values are (1 - σ_a/σ_b) where σ_a is the posterior error standard deviation and σ_b is the prior error standard deviation. Taken from [11].

In addition to answering questions about the fundamental processes that govern the global carbon cycle, space-based CO_2 measurements have the potential to improve anthropogenic GHG emission estimates. Emission reduction goals are traditionally based on “bottom-up" inventories, created by aggregating data from a multitude of sectors and industries that impact the carbon budget for a given nation. Current global inventories include the Emission Database for Global Atmospheric Research (EDGAR; [13]), Carbon Dioxide Information Analysis Centre (CDIAC; [14]), and the Open-source Data Inventory for Anthropogenic CO_2 (ODIAC; [15, 16]). However, these inventories contain considerable uncertainty. Global estimates are thought to be accurate to within 6-10%, but for individual countries, especially in the developing world, those uncertainties can be much larger as they lack the resources to adequately track emissions [17]. Additionally, emissions from the developing world represent an ever-growing fraction of the total global emissions. A potentially more accurate way to constrain these estimates is by creating “top-down" emission estimates. That is, estimates from direct measurements of atmospheric CO_2.

1.3 The Importance of Carbon Dioxide Measurements

While well-calibrated ground-based networks of GHG measurements exist, including about 145 stations organized by the World Meteorological Organization (WMO) Global Atmospheric Watch (GAW) [18], they are insufficient when it comes to spatial resolution for CO_2 and CH_4. As shown in Figure 1.4, coverage is lacking in scientifically important regions including the tropics, much of the global oceans, much of Africa, and arctic and boreal regions. Additionally, they lack the coverage to identify or quantify emissions on national scales in order to produce top-down GHG inventories or to provide information about regional scale natural sources and sinks of CO_2 [19].

Satellites GHG measurements, however, have the potential to complement the existing in situ network. While there are technical limitations with space-based instruments, their measurements are not beholden to geographic or political boundaries and thus represent a significant improvement over in situ data in terms of global coverage. In order for space-based measurements to be of use to the scientific community, precision and accuracy requirements must be defined and subsequently met. Scientifically, high precision is necessary because even the largest CO_2 sources and sinks only produce small changes in the column CO_2.

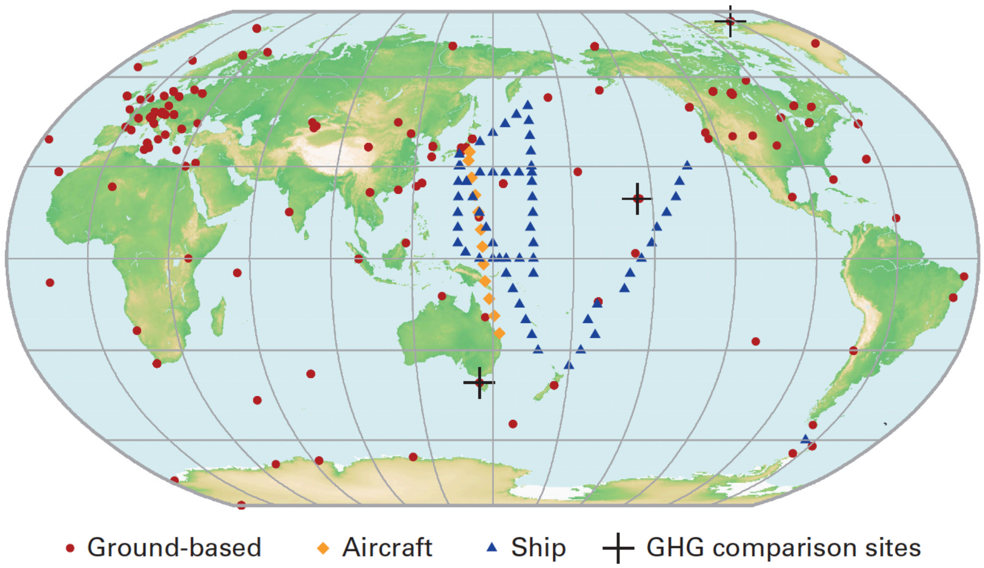

Figure 1.4: The GAW global network for CO_2 in the last decade. Taken from [18].

Early estimates of the required CO_2 precision demanded a monthly averaged column precision of better than 2.5 ppm for an 8° by 10° footprint in order for satellite measurements to be of more use to carbon transport inversion models than just having ground-based in situ measurements [8]. Figure 1.5 shows that the theoretical decrease in uncertainty in CO_2 fluxes is reduced as the precision of the X_{CO_2} measurements is improved.

More recent studies have estimated that an accuracy of better than about 0.5% ($\sim$2 ppm for CO_2) is required for space-based measurements to be of use in estimating regional carbon fluxes [9, 20–24]. In terms of precision, even a bias of a few tenths of a ppm can be detrimental to carbon transport inversion models [9, 10, 25]. For example, [10] showed that a few tenths of a ppm bias in X_{CO_2} on a regional scale introduced a carbon flux error of over 0.7 GtC yr^{-1} over temperate Eurasia. Retrievals of X_{CO_2} are constantly improving and are beginning to approach the level of precision and accuracy needed to study regional sources and sinks [26–31], individual power plants [32], cities [33], etc. However, current single measurement random errors of 0.4 to 1.2 ppm and systematic biases between 1 to 2 ppm still exist over much of the globe [34–36]. Thus, further work is needed to maximize the quality of these data in order for current and future missions to be able to properly answer questions about the carbon cycle.

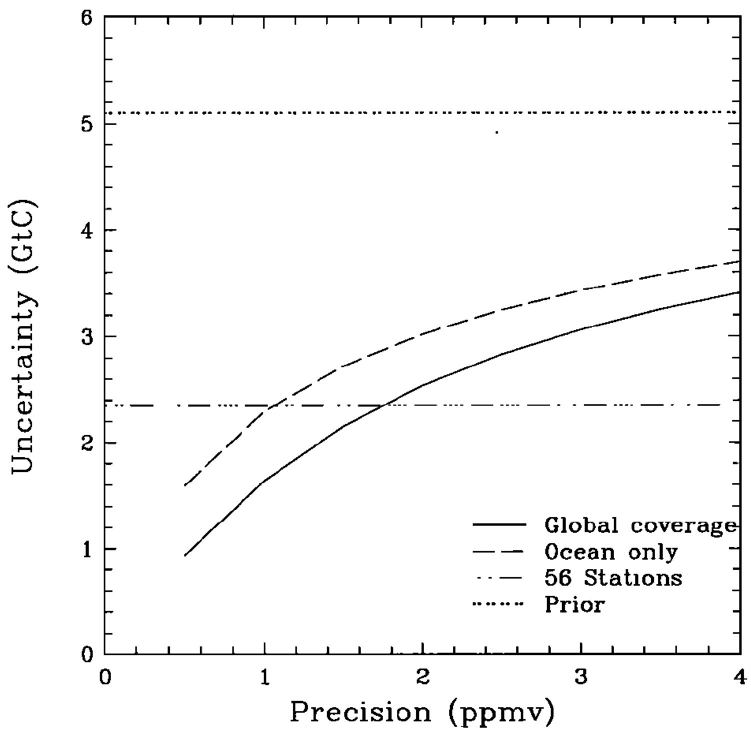

Figure 1.5: Plot of uncertainty in GtC yr^{-1} against the precision (in ppm) of column-integrated data. The dotted horizontal line shows the prior uncertainty while the dash-dot horizontal line shows the case for the in situ surface network. Taken from [8].

The first space-based instrument to be able to detect CO_2 from space was the High-Resolution Infrared Radiation Sounder (HIRS-2; [37]) onboard the Television and Infrared Operational Satellite Next Generation (TIROS-N) Operational Vertical Sounder (TOVS; [38]), launched in 1978. However, the estimated accuracy on these thermal infrared measurements was around 10 ppm, which is about the same magnitude as the entire natural seasonal cycle of CO_2 [39].

The first dedicated instrument to measure CO_2 from space was the SCanning Imaging Absorption SpectroMeter for Atmospheric CHartographY (SCIAMACHY, [40]). It was launched by the European Space Agency (ESA) in March of 2002 on board the Environmental Satellite (ENVISAT) and functioned until May of 2012, when communication with ENVISAT was lost. SCIAMACHY had a 30 by 60 km^2 footprint and measured in eight spectral bands, spanning from the ultraviolet to the shortwave infrared. SCIAMACHY made observations that resulted in continental and seasonal scale variations of CO_2 to be observed for the first time [41, 42].

The first mission whose primary objective was to measure GHGs was the Greenhouse gas Observing SATellite (GOSAT), launched on 23 January 2009 by the Japan Aerospace Exploration Agency (JAXA), National Institute of Environmental Science (NIES), and the Ministry of the Environment (MOE) of Japan. It contains the Thermal and Near Infrared Sensor for Carbon Observation-Fourier Transform Spectrometer (TANSO-FTS), which allows for near-infrared measurements of CO_2 and CH_4, among other things. Near-infrared measurements have a nearly uniform sensitivity to CO_2, from the surface up to the middle troposphere. This allows for the column average of CO_2 to be estimated. GOSAT also contains the Cloud and Aerosol Imager (TANSO-CAI) for use in cloud and aerosol screening. GOSAT represents a substantial improvement in footprint resolution over SCIAMACHY, with an approximate footprint size of 10.5 km. Figure 1.6 shows some of the early X_{CO_2} results from GOSAT.

While NASA had originally planned to launch their own GHG measuring satellite in February of 2009, known as the Orbiting Carbon Observatory (OCO), the launch failed. It took until 2 July 2014 before the spare instrument, named the Orbiting Carbon Observatory-2 (OCO-2), was launched into orbit at the head of the NASA Afternoon Train [43]. OCO-2 represents a further

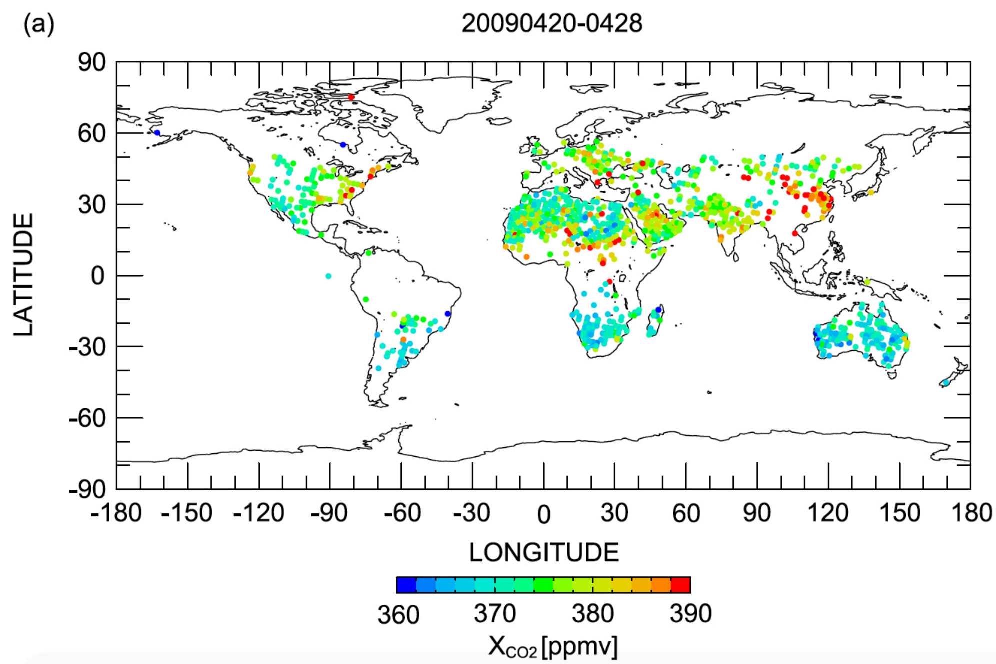

Figure 1.6: The global distribution of X_{CO_2} for 20-28 April 2009 from GOSAT TANSO-FTS spectra with signal-to-noise greater than 100 and for cloud-free scenes over land. Taken from [12].

improvement in near-infrared footprint resolution, coming in at approximately 1.29 km by 2.25 km with eight footprints contained along a 10 km swath. Further details about OCO-2, the primary mission studied in this work, can be found in Section 1.3.1.

In December of 2016, the China Meteorological Administration (CMA), Ministry of Science and Technology of China (MOST), and the Chinese Academy of Sciences (CAS) launched TanSat [44], which contains the Atmospheric Carbon-dioxide Grating Spectrometer (ACGS) and Cloud and Aerosol Polarization Imager (CAPI). TanSat has similar geometric properties to OCO-2, including an 18 km swath containing nine footprints with 2 km by 3 km resolution. Chinese agencies have also launched the Feng-Yun 3D (FY-3D) Greenhouse gases Absorption Spectrometer (GAS) and the GaoFen-5 (GF-5) Greenhouse-gases Monitoring Instrument (GMI) satellites in November 2017 and May 2018, respectively. Little published information is currently available on these two missions.

Besides the current suite of near-infrared measurements of GHGs, thermal infrared instruments can also measure CO_2, but only in certain parts of the atmosphere as they are not typically sensitive to near the surface. This vertical weighting means that these measurements are unable to resolve surface fluxes and are thus of less use to carbon transport inversion models. Besides HIRS, discussed above, these instruments include the Atmospheric Infrared Sounder [45], the Infrared Atmospheric Sounding Interferometer [46], and the Tropospheric Emission Spectrometer [47]. Solar occultation measurements have also been taken by SCIAMACHY as well as a Fourier Transform Spectrometer (FTS) onboard the Atmospheric Chemistry Experiment (ACE) on SciSat [48]. These measurements produce profiles of GHGs, but the lack of measurements below approximately 5 km due to viewing and geometric restrictions again precludes them from studying surface carbon fluxes.

1.3.1 The Orbiting Carbon Observatory-2

OCO-2 is in a 98.8 minute sun synchronous orbit with a 13:36 local time equatorial crossing time for its ascending node. OCO-2 measures near-infrared reflected sunlight in three high-resolution spectral bands using a three-channel imaging grating spectrometer and, like other near-infrared instruments, is sensitive to the whole column of CO_2. It has a repeat cycle of typically 16 days, but because of the narrow footprint (eight adjacent footprints of 1.29 km by 2.25 km), does not actually measure much of the earth. OCO-2 is also unique in that its primary mission is only to measure CO_2. Along with GOSAT, OCO-2 is restricted to daytime measurements of near-infrared reflected sunlight. Figure 1.7 shows an example of the eight OCO-2 footprints and corresponding radiances, taken from the OCO-2 Algorithm Theoretical Basis Document (OCO-2 ATBD; [49]).

OCO-2 takes measurements in three primary modes: nadir, glint, and target. Nadir mode is when the satellite points directly down to make measurements below the satellite. This mode is effective over land, where the surface bidirectional reflectance distribution functions (BRDFs) allow for incoming sunlight to be scattered in a semi-lambertian manner and thus sufficient light is typically reflected straight upwards, regardless of sun angle. Glint mode, designed for use over ocean, follows the “glint spot" of sunlight reflected off of the liquid water surface. The reflectance of sunlight over water is primarily a function of wind speed and is well-characterized [50]. Target

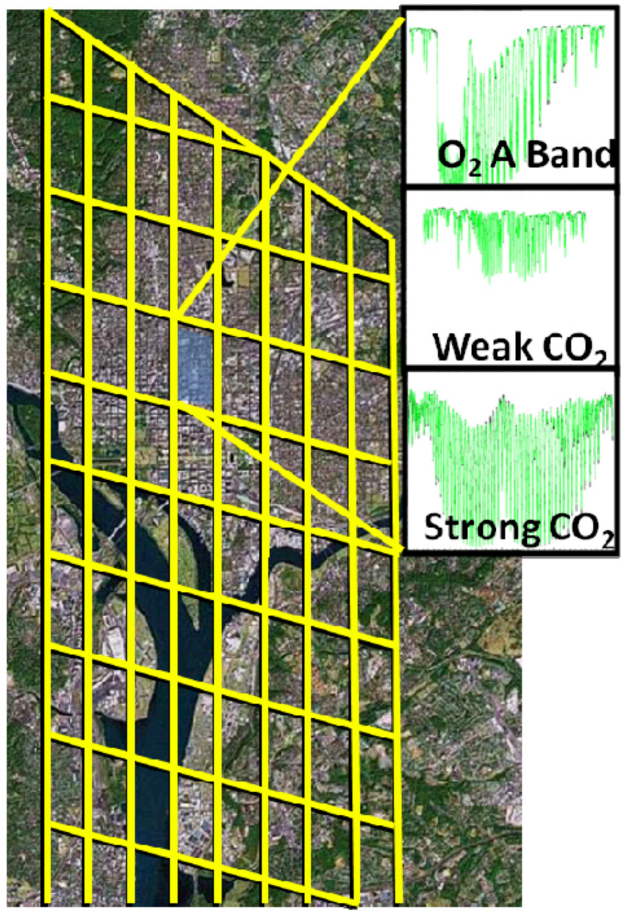

Figure 1.7: Spatial layout of 8 cross-track footprints for nadir observations over Washington, D.C. Taken from the OCO-2 ATBD [49].

mode is where OCO-2 dithers back and forth over a small target spot on the surface. This is used primarily to target Total Carbon Column Observing Network (TCCON; [51]) stations for use as validation. Figure 1.8 shows the setup of nadir, glint, and target mode observations. Full details of the instrument can be found in the OCO-2 ATBD.

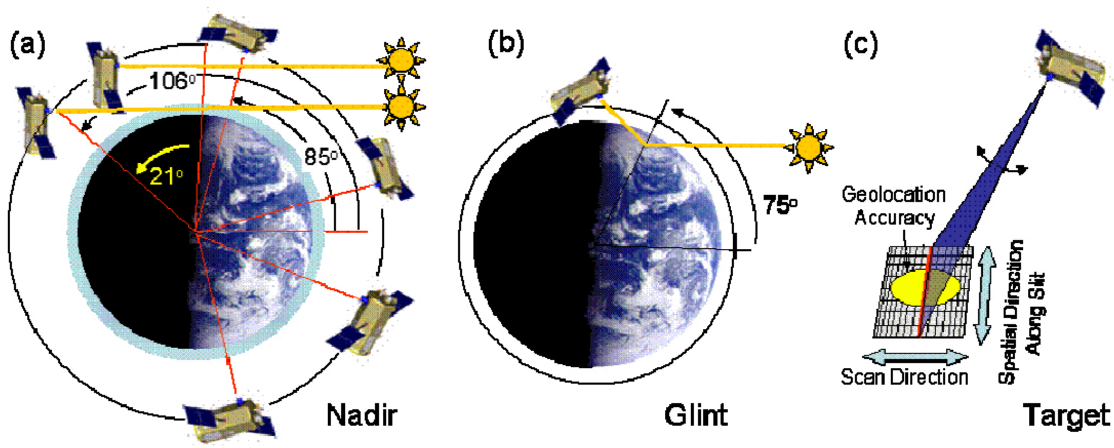

Figure 1.8: Schematic of the OCO-2 observation modes: nadir (a), glint (b), and target (c). Taken from the OCO-2 ATBD [49].

1.3.2 Future Missions

GOSAT-2 was launched on 29 October 2018 and carries TANSO-FTS-2 and TANSO-CAI-2. Both instruments have improved specifications compared to the original GOSAT mission including additional bands and an intelligent pointing algorithm. In March of 2019 the instrument backup to OCO-2 will be launched as the Orbiting Carbon Observatory-3 (OCO-3) to the International Space Station (ISS) [52]. It will have a different pointing system than OCO-2 which will allow for new opportunities to map large target areas including cities, forests, and coastlines. The ISS's low inclination orbit will also allow OCO-3 to make measurements of the same location at different times of the day, allowing for investigations into the daily variability of CO_2. Being on the ISS will also allow for the use of co-located measurements from other instruments on the platform, including the NASA Global Ecosystem Dynamics Investigation (GEDI, successfully launched on

5 December 2018), the NASA Ecosystem Spaceborne Thermal Radiometer Experiment on Space Station (ECOSTRESS), and the JAXA Hyperspectral Imager Suite (HISUI).

There are several CO_2 measuring satellites planned for the years 2019-2023, including MicroCarb, GeoCarb [53, 54], Feng-Yun 3G, and GOSAT-3. MicroCarb is being developed by the Centre National d'Etudes Spatiales (CNES) of France. It is similar to other near-infrared sensors but will have an additional oxygen absorption band for better aerosol detection. NASA's GeoCarb will be the first satellite dedicated to measuring GHGs from geostationary orbit. This will allow for imaging of the Americas potentially multiple times a day. Little is known about Feng-Yun 3G, but it is supposed to be a broad-swath (100 km) imaging grating spectrometer. GOSAT-3 will be an upgraded version of GOSAT-2, with enhanced precision and additional channels. Figure 1.9 shows a timeline of the past, current, and future missions for both CO_2 and CH_4.

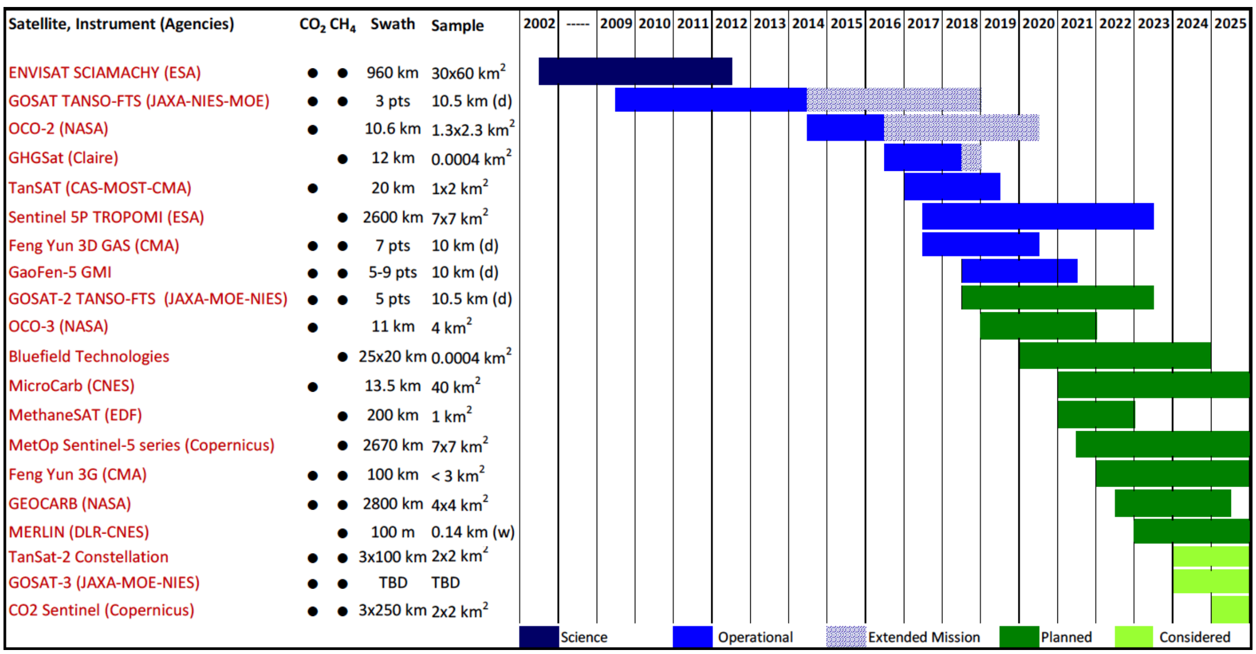

Figure 1.9: Timeline of space-based greenhouse gas measurement satellites.

The current and planned space-based GHG missions will be an incredible boon to the scientific community, but only if the data are precise and accurate. The number of global measurements will soon no longer be the limiting factor, but rather the quality of the data itself.

1.4 Retrieving Carbon Dioxide from Satellites

As discussed in Section 1.3, one of the primary ways to measure CO_2 concentrations from space is by detecting sunlight that has been reflected off the earth's surface with hyper-spectral resolution instruments. The number of CO_2 molecules in the column of air seen by the instrument, or the "light path", is then estimated and eventually converted to a column-average CO_2. This method is conceptually shown in Figure 1.10.

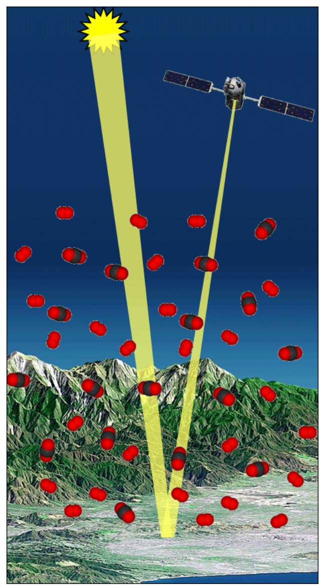

Figure 1.10: The light path is conceptually shown as the yellow beam emitting from the sun, getting reflected off the surface of the Earth, and being detected by the satellite.

OCO-2 makes use of this method using its three-channel imaging grating spectrometer. The three channels are: a band centered on an oxygen absorption feature at 0.76 μm (the O_2 A-band), a relatively weak CO_2 absorption band located in the near-infrared around 1.61 μm (the weak CO_2 band), and a stronger CO_2 absorption band in the near-infrared at 2.06 μm (the strong CO_2 band). These three bands are used in conjunction to deduce the average amount of CO_2 in the column of air seen by the instrument's sensors. The single value of CO_2 in the column of air is specifically known as the column-averaged dry-air mole fraction of carbon dioxide, or $X_{\mathrm{CO_2}}$:

$$X_{\mathrm{CO_2}} = \frac{\int_0^\infty N_{\mathrm{CO_2}}(z)dz}{\int_0^\infty N_{\mathrm{d}}(z)dz} \tag{1.1}$$

where $N_{CO_2}(z)$ is the molecular number density of CO_2 with respect to dry air at altitude z and $N_d(z)$ is the molecular number density of dry air at altitude z. Because the fraction of oxygen in air is well known (0.20935 parts per part) and near uniform globally, Equation 1.1 can be simplified to:

$$X_{\mathrm{CO_2}} = 0.20935\frac{\int_0^\infty N_{\mathrm{CO_2}}(z)dz}{\int_0^\infty N_{\mathrm{O_2}}(z)dz} \tag{1.2}$$

where the number density of O_2 and CO_2 can be estimated using measurements of reflected sunlight in the O_2 A-band, weak CO_2 band, and strong CO_2 band. An example of the measured spectra of all three near-infrared bands from OCO-2 is shown in Figure 1.11.

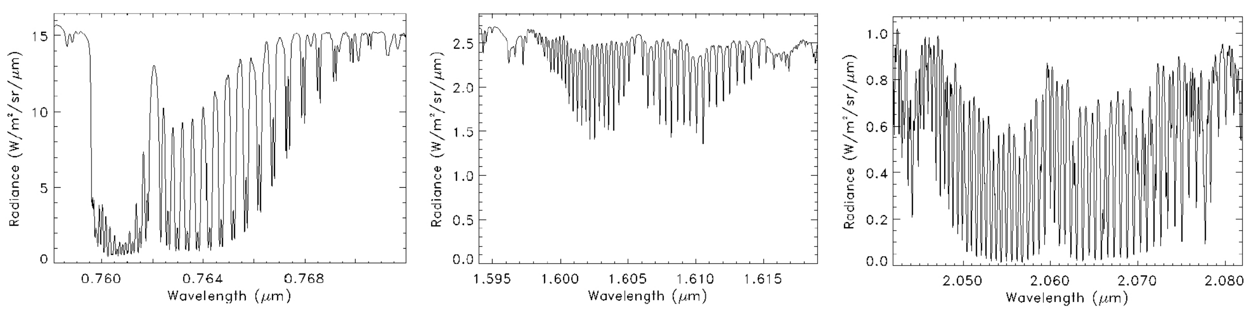

Figure 1.11: An example of measured radiances from OCO-2 in the O_2 A-band (left), weak CO_2 band (center), and strong CO_2 band (right). Taken from [55].

The properties of the three near-infrared bands for OCO-2 are given in Table 1.1.

Table 1.1: Properties of the three near-infrared bands used by OCO-2 to retrieve $X_{\mathrm{CO_2}}$.

Band	Spectral Range (cm^{-1})	Spectral Range (μm)	# Channels	Resolving Power ($\lambda/\delta\lambda$)
O_2 A	12950-13190	0.758-0.772	1016	>17,000
Weak CO_2	6166-6286	1.594-1.619	1016	>20,000
Strong CO_2	4810-4897	2.042-2.082	1016	>20,000

The X_{CO_2} retrieval algorithm used in this study was the NASA Atmospheric CO_2 Observations from Space (ACOS) algorithm (see [56] and [49] for details). It is currently on build 9 (B9), but the majority of this work was done using the previous version (B8). The differences between B8 and B9 were minor and only impacted a small number of retrievals. B10 is currently in development, with an expected public release in spring of 2020.

1.4.1 Optimal Estimation

The ACOS algorithm employs optimal estimation to retrieve X_{CO_2} [57]. This method is useful for combining observations and prior knowledge about a given measurement ("*a priori*" information). In near-infrared measurements of GHGs, the detected radiances alone are insufficient to properly constrain all the parameters that impact the estimated variables of interest. This is known as an "under-constrained" problem. Thus, prior information about a given measurement is employed to help guide the estimates. Complete details of the algorithm can be found in the OCO-2 ATBD [49]. Optimal estimation of X_{CO_2} uses a set of variables, or a "state vector", to create a modeled set of radiances, described in Section 1.4, that match the radiances measured by the satellite, moderated by prior knowledge of the different state vector elements. This is done by using the state vector parameters found in the forward model, **F**:

$$\mathbf{y} = \mathbf{F}(\mathbf{x}, \mathbf{b}) + \boldsymbol{\epsilon} \tag{1.3}$$

where **y** is a vector of the simulated radiances, **F** is the forward model, **x** is the state vector, **b** is a set of other fixed input parameters, and $\boldsymbol{\epsilon}$ is instrument and forward model errors. The OCO-2 forward model is designed to simulate radiances using a solar model, radiative transfer (RT) model, and instrument model [49, 58, 59].

The state vector elements are listed in Table 1.2. The parameters selected for inclusion in the state vector typically represent physical quantities to which the measured spectra are sensitive. The exact parameters included in the current ACOS state vector have been refined over the past several years and details on many of them can be found in [56] and [49], with various updates contained in [60]. Of note, a CO_2 profile of 20 layers is retrieved by the algorithm and then used to calculate the total $X_{\mathrm{CO_2}}$. Other retrieval algorithms use their own unique covariance matrices and CO_2 profile parameterizations, discussed in Section 1.6. Aerosols, surface characteristics, and Empirical Orthogonal Functions (EOFs), etc. are all included in the state vector to allow the retrieval to optimally fit the measured radiances. Certain parameters that impact the measured radiances are not retrieved, either because their impact is negligible, e.g. ozone absorption, or the impact is very well characterized, e.g. Rayleigh scattering.

The simulated radiances, **y**, are used in an inverse model to try and minimize the χ^2 cost function given by:

$$\chi^2 = (\mathbf{F}(\mathbf{x}) - \mathbf{y})^{\mathrm{T}} \mathbf{S}_\epsilon^{-1} (\mathbf{F}(\mathbf{x}) - \mathbf{y}) + (\mathbf{x} - \mathbf{x}_a)^{\mathrm{T}} \mathbf{S}_a^{-1} (\mathbf{x} - \mathbf{x}_a) \tag{1.4}$$

where $\mathbf{S}_\epsilon$ is the observation error covariance matrix, $\mathbf{x}_a$ is the *a priori* state vector, and $\mathbf{S}_a$ is the *a priori* error covariance matrix. The *a priori* state vector and its corresponding error covariance matrix are derived from several sources including the Goddard Earth Observing System Model, Version 5 Forward Processing for Instrument Teams (GEOS-5 FP-IT; [62]) for the meteorological variables and zonally averaged seasonal cycles coupled with a typical atmospheric growth rate for CO_2. In optimal estimation, the prior and posterior errors are assumed to be Gaussian. The expected value, $\hat{\mathbf{x}}$, is given by:

$$\hat{\mathbf{x}} = \mathbf{x}_a + (\mathbf{K}^{\mathrm{T}} \mathbf{S}_y^{-1} \mathbf{K} + \mathbf{S}_a^{-1})^{-1} \mathbf{K}^{\mathrm{T}} \mathbf{S}_y^{-1} (\mathbf{y} - \mathbf{K}\mathbf{x}_a) \tag{1.5}$$

where $\mathbf{S}_y$ is the *a posteriori* error covariance matrix and $\mathbf{K}$ is the Jacobian, which is the partial derivative of the radiance spectrum for each state vector element:

$$\mathbf{K}_{ij} = \frac{\partial \mathbf{F}_i(\mathbf{x})}{\partial \mathbf{x}_j} \tag{1.6}$$

The Levenberg-Marquardt modification of the Gauss-Newton method [57] is then used to iteratively minimize the cost function described by 1.4:

Table 1.2: State vector elements of the ACOS X_{CO_2} retrieval algorithm, adapted from [60].

Name	Quantities	*A Priori* Value	*A Priori* 1σ Error	Notes
CO_2	20	TCCON	[56]	On sigma pressure levels[1]
Temperature Offset	1	0 K	5 K	Offset to prior profile
Surface Pressure	1	GEOS-5 FP-IT	4 hPa	
H_2O Scale Factor	1	1.0	0.5	Multiplier on prior profile
Aerosol Type 1,2 OD[2]	2	MERRA-2[3]	$\pm$ factor of 7.39	
Water, Ice Cloud OD[2]	2	0.0125	$\pm$ factor of 6.05	
Aerosol Type 1,2 Height[4]	2	0.9	0.2	
Water Cloud Height[4]	1	0.75	0.4	
Ice Cloud Height[4]	1	Tropopause[5]	0.2	
Aerosol Type 1,2 Width	2	0.05	0.01	
Water Cloud Width	1	0.1	0.01	
Ice Cloud Width	1	0.04	0.01	
UTLS Aerosol OD[2]	1	0.006	$\pm$ factor of 6.05	
Albedo Mean Land	1/band	Prior Calc.	1.0	
Albedo Slope Land	1/band	0.0	0.0005	
Albedo Mean Ocean	1/band	0.02	{0.2,0.2,1e-3}	
Albedo Slope Ocean	1/band	0.0	1.0	
SIF Mean[6]	1	Prior Calc.	0.008	Land only
SIF Slope	1	0.0018	0.0007	Land only
Wind Speed	1	GEOS-5 FP-IT	5 m/s	Ocean only
Dispersion Shift	1/band	0.0	0.4 of channel FWHM	
Dispersion Stretch	1/band	0.0	1 pm/channel	
EOF Amplitudes	3/band	0.0	10.0	

[1] CO_2 profile contain 20 or fewer elements, depending on the surface pressure.

[2] Optical Depth at 0.76 μm.

[3] Monthly climatology from 2006.

[4] Peak heights of the Gaussian distributions.

[5] Estimate from GEOS-5 FP-IT parameters.

[6] See [61].

$$\mathbf{x}_{i+1} = \mathbf{x}_i + (\mathbf{K}_i^{\mathrm{T}}\mathbf{S}_\epsilon{}^{-1}\mathbf{K}_i + (1+\gamma)\mathbf{S}_a^{-1})^{-1}[\mathbf{K}_i^{\mathrm{T}}\mathbf{S}_\epsilon^{-1}(\mathbf{y} - \mathbf{F}(\mathbf{x}_i)) + \mathbf{S}_a^{-1}(\mathbf{x}_a - \mathbf{x}_i)] \qquad (1.7)$$

where $\mathbf{x}_i$ is the initial state vector, $\mathbf{x}_{i+1}$ is the updated state vector, and $\mathbf{S}_\epsilon$ is the observation error covariance matrix. $\mathbf{x}_{i+1}$ is then re-run through the forward model and the result is used to try and again find the minimum χ^2. This iterative process is repeated until certain thresholds are reached that indicate the algorithm has converged to a state vector containing optimal values that minimize the cost function.

1.5 Cloud and Aerosol Errors in X_{CO_2} Retrievals

While there are many issues that can result in reduced accuracy and precision in near-infrared estimates of CO_2, including calibration errors, spectroscopic errors [63], instrument noise, improper forward model assumptions, etc., one of the most significant issues that arises when measuring X_{CO_2} is the presence of clouds and aerosols. The main reason clouds and aerosols can ruin a retrieval is due to light path modification. In order to precisely measure the light path, as described in Section 1.4, the number of molecules in the column must be established. If clouds and aerosols are present they can scatter the reflected sunlight in different directions which can drastically alter the length of the light path seen by the sensor and result in significant errors when calculating X_{CO_2} (see Section 1.5.1). Various screening methods are employed to remove scenes with measurements that are obviously contaminated by clouds and aerosols (see Section 1.5.2), but no scene is entirely free from scattering particles. It has been shown that not including state vector parameters relating to the scattering and absorption of these remaining aerosols and clouds can lead to significant errors in retrievals of X_{CO_2}. These errors often exceed 1% ($\sim$4 ppm) and can be tens of ppm for high optical depth scenes [64–66]. Figure 1.12 demonstrates the X_{CO_2} errors induced as a function of aerosol optical depth for a retrieval that does not include any state vector elements relating to cloud and aerosols, known as a “non-scattering" or “clear-sky" retrieval.

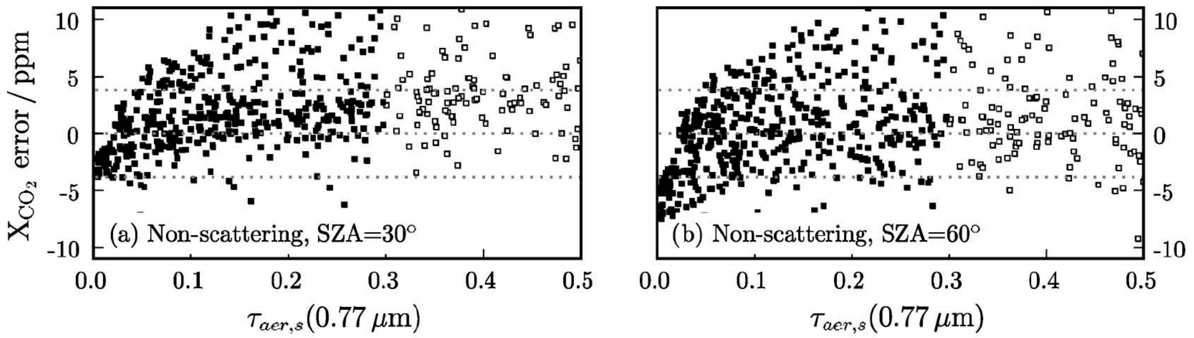

Figure 1.12: Residual aerosol-induced $X_{\mathrm{CO_2}}$ error as a function of aerosol optical thickness at 0.77 μm for a non-scattering retrieval at a solar zenith angle of 30° (left) and 60° (right). Filled and open boxes correspond to scenes with aerosol optical thickness less and greater than 0.3, respectively. Dotted gray lines indicate 1% error limits on $X_{\mathrm{CO_2}}$. Adapted from [66].

Even when scenes are heavily filtered to remove clouds and aerosols, a non-scattering $X_{\mathrm{CO_2}}$ retrieval performs about 20-40% worse than one that includes a way to account for scattering effects [67]. More specifically, errors in the optical properties or vertical distribution of optically thin clouds and aerosols, such as smog, smoke, sea salt, and dust, can result in biases in the retrieved CO_2 [68,69]. [70] notes that, "a more reliable treatment of the scattering by optically thin clouds and aerosols will be critical for retrieving $X_{\mathrm{CO_2}}$ and $X_{\mathrm{CH_4}}$ in the presence of fossil fuel or biomass plumes, since aerosols are co-emitted with CO_2 and CH_4." This is especially important over large cities, power plants, and tropical rainforests, which are all of scientific interest in the GHG community but typically associated with clouds and aerosol emissions. Thus, understanding the mechanistic behavior of carbon sources and sinks is dependent on a proper handling of clouds and aerosols.

1.5.1 Scattering Effects of Clouds and Aerosols

Aerosols suspended in the atmosphere are capable of scattering sunlight. Sources include natural sources such as dust blown up from the surface, sea salt spray from the ocean, and organic carbon from biomass burning. These aerosol originate from the surface and are typically confined to the troposphere with a lifetime on the order of a few weeks. Volcanic emissions can inject gases and aerosols into the stratosphere, where the lack of fast removal mechanisms results in a lifetime of a few years. Anthropogenic aerosols, usually created from the burning of fossil fuels, tend to be highly variable in their concentration and physical properties.

When light interacts with a particle it can be scattered, absorbed, or transmitted. Equation 1.8 describes the size parameter, x, that dictates what type of scattering occurs for a given particle size and light wavelength:

$$x = \frac{2\pi r}{\lambda} \tag{1.8}$$

where λ is the wavelength and r is the radius of a spheric particle. In the near-infrared, the interaction between typical atmospheric aerosols (with r ranging from approximately 0.1 to 10 μm) and photons from the sun is best described by Mie scattering (x $\gtrsim$ 1). Cloud droplets also fall in this range, with radii of approximately 5 to 50 μm and x $\gtrsim$ 1.

In addition to clouds and aerosol, air molecules themselves can result in Rayleigh scattering (x $\ll$ 1). This effect is most prominent in the O_2 A-band, due to the shorter wavelengths, but is included for all three bands in ACOS because it is easily and quickly calculated.

1.5.2 Screening Methods

The scattering and absorption effects of clouds and aerosols on near-infrared measurements of CO_2 are problematic for two reasons. First, the effects are difficult to quantify and light path modifications that are improperly accounted for can lead to large errors in the retrieved state vector (see Section 1.5). Second, the presence of thick cloud or aerosol layers, even if properly parameterized in the retrieval to avoid large biases, means that reflected sunlight is not reaching near the surface, where the primary sources and sinks of CO_2 are located. Thus, these above-cloud/aerosol measurements would be of less use anyways. Because of this, substantial effort has been put towards developing screening methods designed to remove measurements contaminated by cloud or aerosol layers. The two primary filters applied before running the ACOS retrieval on measured radiances from OCO-2 are known as the O_2 A-band Preprocessor (ABP; [71]) and the Iterative

Maximum A-Posteriori Differential Optical Absorption Spectroscopy (IMAP-DOAS) Preprocessor (IDP; [72]).

The ABP works by retrieving surface pressure using only the O_2 A-band with Rayleigh scattering. If this surface pressure deviates by several hectopascals (hPa) from the prior surface pressure, it is likely that a cloud or aerosol layer is present in the scene and is scattering photons back towards the satellite before they hit the surface. The ABP is extremely fast and not computationally expensive because it does not attempt to actually parameterize any clouds or aerosols. The primary weakness of the ABP is its lack of sensitivity to very low cloud and aerosol layers, which can have similar light path lengths to that of the surface and are thus difficult to detect.

The IDP attempts to remove contaminated scenes by independently estimating $X_{\mathrm{CO_2}}$ and $X_{\mathrm{H_2O}}$ from both the weak and strong CO_2 bands using a simple non-scattering retrieval. The ratio of these two measurements, for example $X_{\mathrm{CO_2}}$ from the weak CO_2 band divided by $X_{\mathrm{CO_2}}$ from the strong CO_2 band, is then used as a scattering metric. Because cloud and aerosol particles typically have wavelength-dependent absorption properties, the scattering effects modify the weak CO_2 band differently than the strong CO_2 band. This leads to a ratio that deviates from unity in the presence of a cloud or aerosol layer. In the absence of scattering, a non-scattering retrieval should produce ratios of near unity. While the ABP struggles to identify low-level contamination, the IDP excels at identifying aerosols at any height, due to their wavelength-dependent optical properties. Combining the ABP and IDP results in the ability to detect and remove most but not all scenes containing clouds or aerosols [71]. For example, Figure 1.13 demonstrates that the cloud detection algorithms developed for use on OCO-2 measurements agree well with the cloud determination algorithm from the Moderate Resolution Imaging Spectroradiometer (MODIS; [73]) on the NASA Terra satellite.

Because not all measurements contaminated by clouds and aerosols can be removed, near-infrared retrievals must therefore include scattering parameters in their state vectors in order to avoid errors.

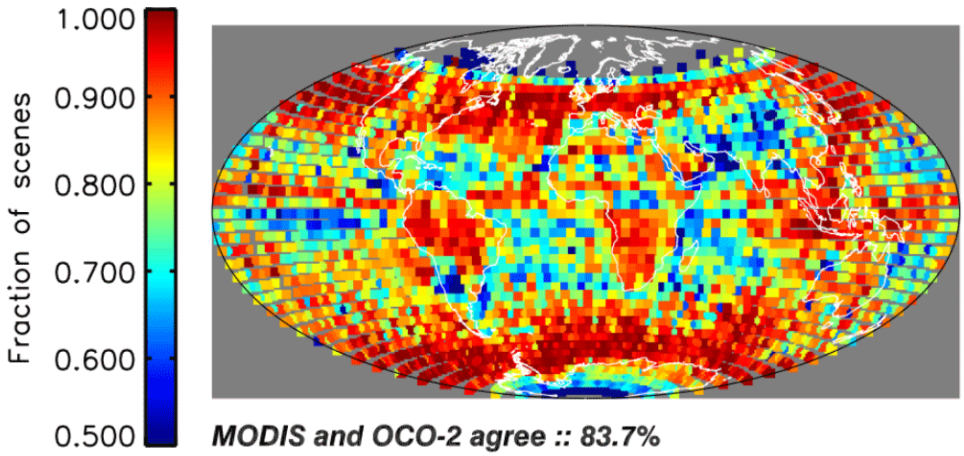

Figure 1.13: Combined glint and nadir gridded contingency table data for real OCO-2 measurements made in December 2014. Data are binned on a 4° by 4° lat/lon grid. Scenes for which MODIS and OCO-2 cloud screenings agree are shown. Adapted from [71].

1.6 Aerosol Parameterizations in Near-Infrared Measurements of GHGs

Typically, one or more pieces of information about clouds and aerosols are solved for in addition to X_{CO_2} in GHG retrieval algorithms applied to near-infrared measurements. Some common methods include retrieving various optical properties of an aerosol type [12, 74, 75], retrieving vertical aerosol information [49, 75–77], retrieving parameters directly related to the photon path length [78], and parameterizing aerosols with a single isotropic scattering layer [79]. All these methods are intended to act as proxies to the real scattering effects of clouds and aerosols in the column in order to allow an accurate X_{CO_2} to be retrieved. However, it is not clear that any one method is best and additional research, including robust intercomparison studies, is needed to determine the optimal setup.

The latest operational OCO-2 X_{CO_2} retrieval algorithms, ACOS B8 and B9, include nine parameters related to clouds and aerosols, which describe an ice cloud, water cloud, and three aerosol types. However, retrieved aerosol optical depths (AODs), a measure of the extinction of sunlight due to atmospheric scattering particles, from ACOS generally compare poorly to the highly accurate AErosol RObotic NETwork (AERONET, [67, 80]). This indicates that the way ACOS handles the scattering effects of clouds and aerosols can potentially be improved.

1.6.1 ACOS Aerosol Parameterization

The ACOS aerosol parameterization contains five atmospheric particle types: a water cloud, ice cloud, two aerosol types from a Modern-Era Retrospective analysis for Research and Applications, Version 2 (MERRA-2; [81]) climatology, and a stratospheric aerosol type. This MERRA-2 climatology is the monthly mean for one year (2006) for each of the five MERRA-2 aerosol types (dust, organic carbon, black carbon, sea salt, sulfate). The two types chosen to be included in the state vector are the two with the highest climatological mean AOD for a given month and location. For example, if dust and organic carbon are the two largest AODs of the possible five in the month of July for a given location, then they are selected as the two aerosol types to be retrieved for any July OCO-2 measurement for that location. MERRA-2 actually contains 15 different aerosol types with up to five size bins per type and a relative humidity dependence for some of the types. For simplicity, these are aggregated into the five types used in ACOS B8 (dust, organic carbon, black carbon, sea salt, sulfate). A typical fractional bin density and relative humidity were assumed for each type in order to aggregate them (see [49] for complete details).

The vertical profiles of these aerosol types are described by Gaussian distributions. The vertical height, described by the mean of the Gaussian distribution, and magnitude, described by the amplitude of the Gaussian distribution, are retrieved for each of the two aerosol types, the water cloud, and the ice cloud. The magnitude of the stratospheric aerosol type is solved for, but the height is fixed. The widths of the five Gaussian profiles are fixed, as it has been shown that the radiances are not especially sensitive to the width of a cloud or aerosol layer [66, 82]. The prior Gaussian profiles are shown in Figure 1.14 and described by Equation 1.9.

$$f(x) = \mathbf{A} * exp\left\{ -\frac{(\mathbf{x} - \mathbf{x_a})^2}{2\boldsymbol{\sigma}_\mathbf{a}{}^2} \right\} \tag{1.9}$$

where $\mathbf{x}_a$ is the vertical height of the peak of the Gaussian, $\mathbf{x}$ is the height at each level, and $\boldsymbol{\sigma}_\mathbf{a}$ is the Gaussian width. The magnitude, $\mathbf{A}$, is normalized such that the total aerosol or cloud optical depth value of the column equals the integrated optical depth of the Gaussian curve.

In all, nine variables are included in the state vector that are designed to parameterize the clouds and aerosols in the scene. Additionally, the natural log of the AOD is the parameter solved for that describes the magnitude of each Gaussian. This is to prevent the algorithm from attempting to retrieve a negative AOD, which would result in the retrieval crashing due to current algorithmic limitations. The retrieved height of the Gaussian represents the fraction of the surface pressure. For example, if the surface pressure is 1000 hPa and the retrieved height parameter is 0.5, the Gaussian profile will be centered at 500 hPa.

For each of the five aerosol types solved for in the retrieval, assumptions have been made about their physical properties. The ACOS forward model is designed to be sensitive to the absorption cross sections, single-scatter albedos, and phase matrices of the cloud and aerosol types. The optical properties for the water clouds are calculated from Mie theory, assuming a Gamma particle size distribution with an effective radius of 8 μm. The ice clouds are assumed to have an effective radius of 70 μm and were compiled from MODIS Collection 6 [83]. The method by which the MERRA-2 types are aggregated is described in detail in [49]. For example, the composite mass extinction coefficient ($\mathbf{k_e}$) is calculated by:

$$\mathbf{k_e} = \mathbf{k_{e,1} f_1} + \mathbf{k_{e,2} f_2} \tag{1.10}$$

where $\mathbf{f_1}$ and $\mathbf{f_2}$ are the fraction of each subtype by aerosol density, with $\mathbf{f_1}$ + $\mathbf{f_2}$ = 1. Thus, the aggregated mass extinction coefficient, mass scattering coefficient, single-scattering albedo, and phase function quantities can be trivially calculated.

1.7 Outline

Chapter 2 provides a summary of work done on improving the aerosol priors in retrievals of $X_{\mathrm{CO_2}}$ performed on near-infrared measurements [84]. Chapter 3 discusses simplified aerosol

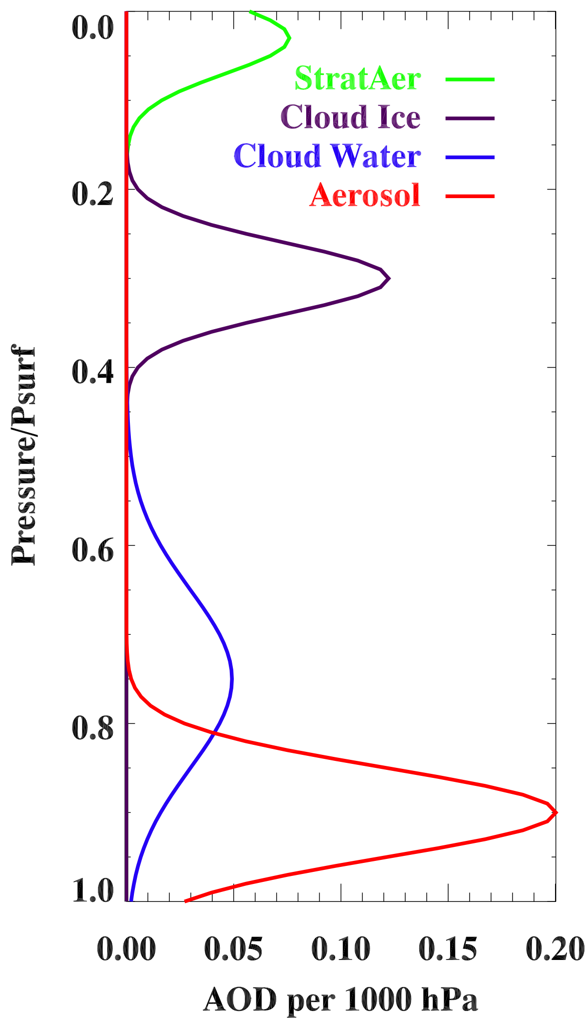

Figure 1.14: Prior Gaussian profiles of the lower tropospheric aerosol types (red), water cloud (blue), ice cloud (purple), and stratospheric aerosol (green). The local AOD per unit pressure at 755 nm is plotted as a function of the relative pressure. The lower tropospheric aerosol prior AOD is not fixed as for the other types, but rather is taken from a climatology described in the text. Taken from [60].

parameterizations in both synthetic and real retrievals of $X_{\mathrm{CO_2}}$ [85]. Chapter 4 draws conclusions and discusses the implications for future GHG missions. Appendix A presents a study on the retrieval and validation of the total column water vapor product from OCO-2 [86].

Chapter 2

The Impact of Improved Aerosol Priors on Near-Infrared Measurements of Carbon Dioxide

2.1 ACOS Aerosol Parameterization

As discussed in Section 1.6.1, the ACOS X_{CO_2} retrieval algorithm takes a prior state vector with associated uncertainties and uses optimal estimation to determine the posterior state vector that best minimizes the modeled radiance residuals as compared to the measured radiances. One choice that impacts how well the retrieved cloud and aerosol parameters perform, and subsequently how well X_{CO_2} is retrieved, is the use of prior information to constrain the problem by adding additional information beyond the spectra themselves. Often, a constant or climatological value with high uncertainty applied to it is used for the aerosol setup. Here, we test the hypothesis that using more realistic aerosol priors will allow the retrieved aerosol parameters to better represent the scattering of light in the column and thus reduce the error in retrieved X_{CO_2}. Specifically, we examine the impact of using co-located modeled aerosols from the Goddard Earth Observing System Model, Version 5 (GEOS-5; [62]) as prior information on the retrieved X_{CO_2} from real OCO-2 measurements. Global atmospheric models, such as GEOS-5, are highly sophisticated and contain many layers of complex physics to represent aerosol processes in the atmosphere including aerosol dynamic schemes and size-resolved aerosol microphysics [87]. However, atmospheric models do not perfectly represent reality. There are still large differences between individual models, which are restricted by uncertainties in aerosol emission source characteristics, knowledge of atmospheric processes, and the meteorological field data used [88]. Despite this, it is hypothesized that these models will still be of use in the X_{CO_2} retrievals. We also examine the uncertainties applied to the aerosol priors in the current OCO-2 X_{CO_2} retrieval algorithm to see if using a lower uncertainty, in conjunction with a more realistic aerosol prior, results in an improvement in X_{CO_2} against multiple validation sources. Finally, we test whether vertical aerosol information from GEOS-5 can be successfully ingested. These results, along with those of Chapter 3, impact not only OCO-2, but X_{CO_2} from GOSAT, TanSat, and several other future space-based GHG missions that will also be significantly influenced by the scattering effects of clouds and aerosols.

2.2 Validation Datasets

Here, we use two datasets to evaluate the quality of the OCO-2 X_{CO_2} retrievals in the context of testing the aerosol parameterization. While we expect the retrieved aerosol parameters to improve with the use of a more accurate prior, the retrieved aerosols are still only designed to be effective scattering parameters and thus we will not evaluate their quality. The first validation dataset is 32,175 retrievals co-located with 13 TCCON and AERONET sites across the globe. The second is 30,827 retrievals matched with an ensemble of global CO_2 models where we consider the truth the median of the CO_2 models in places where they agree to within 1 ppm. These two validation sets complement each other in that TCCON is known to be highly accurate, but with limited spatial coverage. The model validation dataset likely has larger uncertainty than TCCON, but provides excellent spatial coverage.

2.2.1 TCCON and AERONET Validation Dataset

The TCCON validation dataset contained 32,175 OCO-2 measurements taken from 17 September 2014 to 2 May 2016. We co-located the OCO-2 measurements in time and space with the AERONET and TCCON, which were required to both be present and operational at a given site. The co-location criteria was within 1° latitude/longitude and +/- 30 minutes and the sites selected for use are shown in Figure 2.1. As TCCON stations are all located on land, only a small fraction of co-located measurements are over water surfaces.

Table 2.1 lists the TCCON sites used in this study. The measurements were selected from a set of OCO-2 “lite" files [89] that had been pre-filtered (see Section 2.3). We then post-processed the

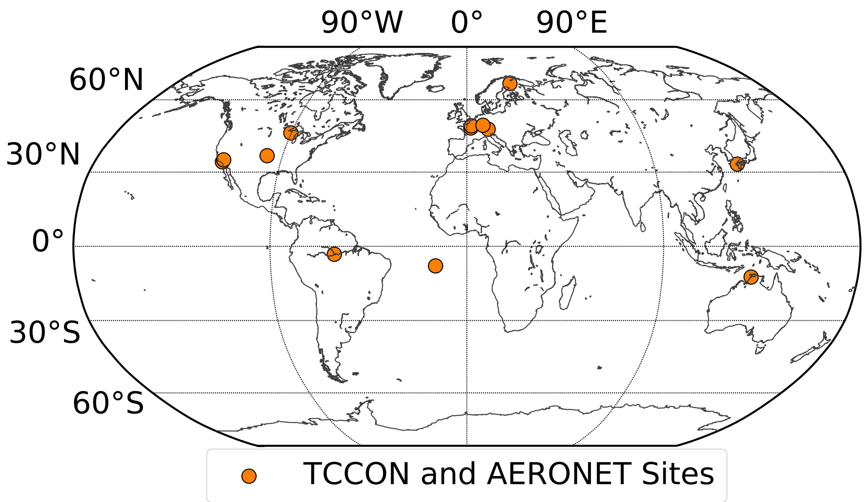

Figure 2.1: TCCON and AERONET sites used in this study.

retrievals with multiple custom filters in an attempt to remove all scenes contaminated by clouds or aerosols.

Table 2.1: TCCON stations used in this study.

TCCON station	Dates Used	Reference
Ascension Island	Sep 2014–Dec 2015	[90]
Caltech, Pasadena, CA, USA	Sep 2014–May 2016	[91]
Darwin, Australia	Sep 2014–May 2016	[92]
Edwards (Armstrong), CA, USA	Sep 2014–Mar 2016	[93]
Garmisch, Germany	Sep 2014–Nov 2015	[94]
Karlsruhe, Germany	Sep 2014–May 2016	[95]
Lamont, OK, USA	Sep 2014–May 2016	[96]
Manaus, Brazil	Oct 2014–Jun 2016	[97]
Orléans, France	Sep 2014–Nov 2015	[98]
Paris, France	Sep 2014–Sep 2015	[99]
Park Falls, WI, USA	Sep 2014–May 2016	[100]
Saga, Japan	Sep 2014–Feb 2016	[101]
Sodankylä, Finland	Sep 2014–Apr 2016	[102]

2.2.2 Model Validation Dataset

Besides validation against the highly accurate but sparsely located TCCON, a set of global CO_2 models was assembled in order to examine spatial errors. We co-located 30,827 OCO-2 measurements in time and space with a suit of nine global carbon models [9, 25, 31, 103–107]. Only points where all the models agreed to within 1 ppm of X_{CO_2} were used. Work by [60] has shown that using this methodology produces similar error statistics to that of the TCCON validation. The median X_{CO_2} of the nine models for each of the 30,827 measurements was used as the truth metric. The OCO-2 measurements were selected by sorting all the measurements into a 4° latitude by 4° longitude spatial grid and filling all grid boxes with up to 10 observations. This allowed for excellent global coverage while limiting the demand on the available computational resources needed to run the retrievals.

2.3 Filtering and Bias Correction

As OCO-2 struggles with scenes containing clouds and aerosols, multiple strategies are used to try and filter out any scene that is contaminated by scattering particles. For both validation datasets, the O_2 A-band Preprocessor (ABP; [71]) and Iterative Maximum A-Posteriori Differential Optical Absorption Spectroscopy (IMAP-DOAS) Preprocessor (IDP; [72]) were applied to every measurement before being selected to run through the retrieval. For each validation set, the approximately 30,000 measurements used in this study were those that had successfully passed through the preprocessors. These measurements were determined to be clear enough to be run through the retrieval. After removing measurements that failed to converge, post-processing filtering techniques were applied to remove additional low-quality retrievals that were not screened out by the preprocessors. These filters included the reduced χ^2, a delta pressure parameter (from ABP), and the CO_2 and H_2O ratios (from IDP). Thus, all tests are being done on a mostly clear dataset and conclusions cannot be drawn about how these retrieval modifications impact the results if scenes with thick cloud or aerosol layers are present. Additionally, as the TCCON stations are located on land, the final post-filtered TCCON validation dataset only contained land measurements and thus no conclusions can be made about OCO-2 measurements over ocean for the TCCON validation study.

Despite heavy pre- and post-filtering of the dataset to remove cloud and aerosol layers, no atmospheric column is truly free from scattering particles. Thus, a bias correction is typically applied to the final $X_{\mathrm{CO_2}}$ in an attempt to mitigate retrieval errors [60]. In the operational B8 product, considerable effort is put into developing a multi-parameter bias correction that reduces the $X_{\mathrm{CO_2}}$ bias against several independent truth metrics. In this work, a single parameter bias correction was selected for each validation dataset for simplicity and to ensure a fair comparison across different setups. Additionally, it is hypothesized that an improved aerosol setup might reduce the need for a complex bias correction. The parameter chosen was that which had the largest correlation with $X_{\mathrm{CO_2}}$ error. When comparing to TCCON, the retrieved $X_{\mathrm{CO_2}}$ was bias corrected by removing a linear fit between the $X_{\mathrm{CO_2}}$ error (retrieved $X_{\mathrm{CO_2}}$ - TCCON $X_{\mathrm{CO_2}}$) and the difference between the retrieved surface pressure and the prior surface pressure ("dp"). This was the most correlated parameter in the majority of our TCCON tests and thus was selected as the bias correction parameter. This parameter is correlated with $X_{\mathrm{CO_2}}$ biases because any unparameterized clouds and aerosols in the column can make the retrieval think there is a lower surface pressure than in reality. Thus, bias correcting this mistake out is designed to bring the retrieved surface pressures back to realistic values and can approximately account for the improperly parameterized clouds and aerosols. In the case of the model validation dataset, the bias correction parameter was the solar zenith angle. Physically, this represents the removal of artificial biases induced by longer air masses. The reason why this parameter was selected over dp is that the model dataset has excellent latitudinal coverage and thus the air mass is weighted more than dp. TCCON, however, is spatially limited and thus the air mass dependence is not as prevalent when searching for optimal bias correction parameters.

2.4 Modeled Aerosol Priors

As discussed in Section 1.6.1, the OCO-2 retrieval algorithm has several aerosol parameters in its state vector. The prior values for most of these parameters in B8 are fixed or taken from a monthly MERRA-2 climatology. Here, we discuss several methods in which we test the use of instantaneous, 3D modeled aerosol data as prior information to improve upon the current priors with the hope of increasing the precision and accuracy of the final OCO-2 $X_{\mathrm{CO_2}}$ product.

The GEOS-5 Forward Processing for Instrument Teams (GEOS-5 FP-IT; [62]) atmospheric model, created and maintained by the NASA Global Modeling and Assimilation Office, is designed specifically for instrument teams in that the entire period (2000-current) is run using the same GEOS-5 version to maintain consistency and avoid any unwanted biases from updates to the model. For this work, GEOS-5 FP-IT version 5.12.4, hereafter referred to as GEOS-5, was co-located in time and space with the OCO-2 measurements. GEOS-5 is on a 0.625° longitude by 0.5° latitude horizontal grid with 72 vertical layers extending to 0.01 hPa with a time-step of 3 hours. The model was linearly interpolated in space and the nearest 3-hour model update was chosen in time. For example, if the OCO-2 measurement was taken at 1900 UTC, the 1800 UTC model run was used. The GEOS-5 aerosol scheme contains 15 different types with up to five different size bins for each type, which we aggregate into five unique types: dust, organic carbon, black carbon, sea salt, sulfate. The aggregation process weights by the typical relative amount of optical depth contributed by each type at 760 nm and uses a typical relative humidity value for the hygroscopic types. Each type has a unique optical properties, including the single-scattering albedo, extinction coefficient, and refractive index. Further details can be found in [49]. GEOS-5 ingests Terra MODIS AOD, Aqua MODIS AOD, and Multi-angle Imaging SpectroRadiometer (MISR; [108]) aerosol information. AERONET measurements are not used for this product as the data latency is unacceptably large. Figure 2.2 shows that GEOS-5 AODs correlate better with AERONET compared to both the climatological MERRA-2 AODs and the corresponding retrieved AOD values from OCO-2 B8. Thus, using the model and assigning it some confidence should result in an improved correlation in retrieved OCO-2 AODs compared to AERONET.

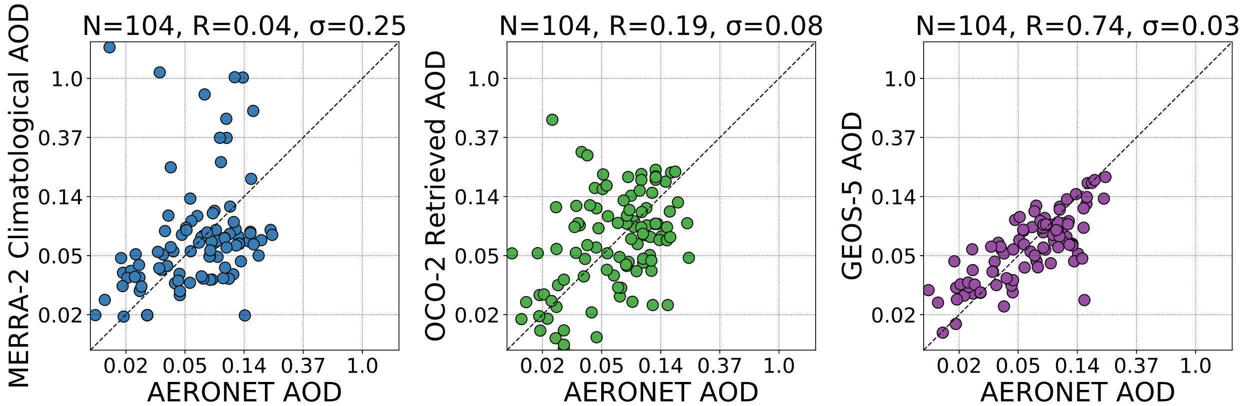

Figure 2.2: Left: MERRA-2 climatological AOD vs. AERONET AOD. Middle: OCO-2 B8 retrieved AOD vs. AERONET AOD. Right: GEOS-5 co-located AOD vs. AERONET AOD. The AERONET AODs are the means of the AODs at 675 nm and 870 nm. Overpass means are plotted.

Our primary hypothesis in this work is that using instantaneous modeled aerosol data as prior information will result in smaller X_{CO_2} errors when compared to the current operational setup that uses a monthly climatology. Figure 2.3 shows the first of the two aerosol types selected when using the MERRA-2 monthly climatology and when using the interpolated GEOS-5 model field. Certain features, such as Saharan dust and biomass burning, are generally realistically placed in the climatology but the day-to-day variations of the atmosphere are not present and thus the climatology is not representative of the true state of the atmosphere for a given OCO-2 measurement location. For example, dust is selected over large portions of the high northern latitudes in the GEOS-5 model field, but rarely in the MERRA-2 monthly climatology.

Three methods of varying complexity were chosen to ingest the instantaneous model data:

- Using the top two aerosol types and their corresponding AODs
- Using the top two aerosol types and fitting the amplitude, mean, and variance of a Gaussian distribution to the modeled vertical profile of both types
- Using the top two aerosol types and solving for a scale factor on an interpolated 20-layer modeled aerosol profile

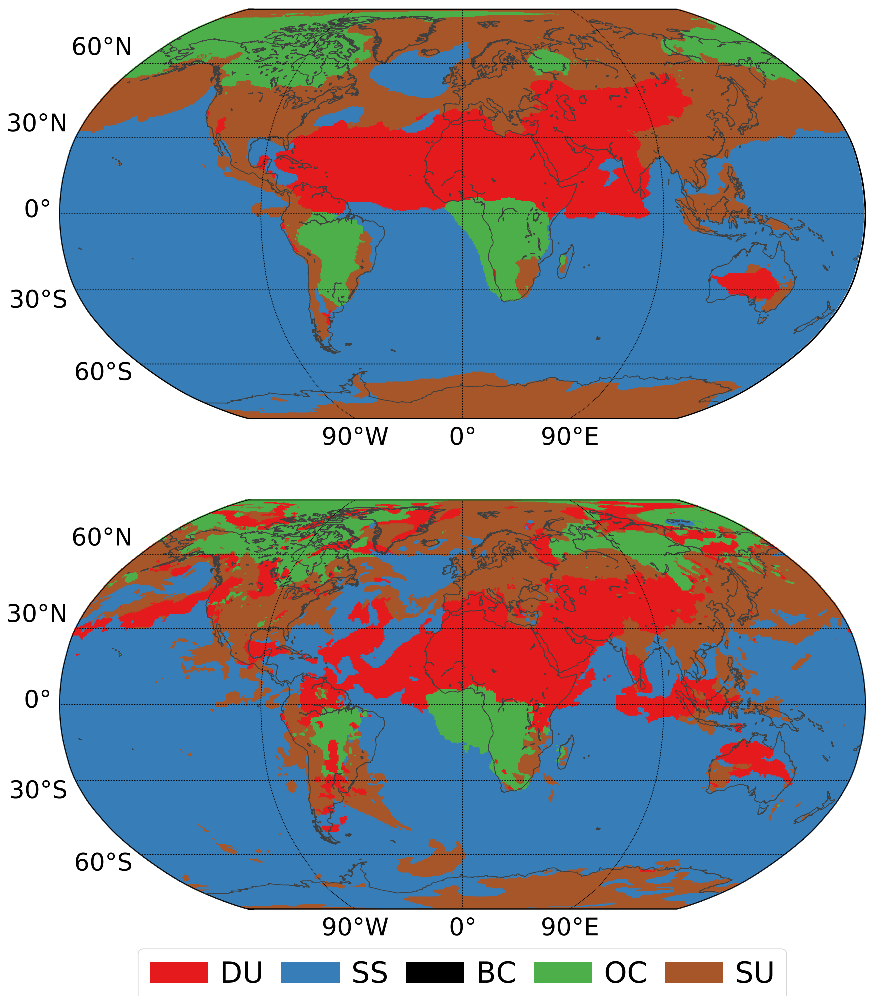

Figure 2.3: Top: primary aerosol type selected for the month of July using the MERRA-2 climatology. Bottom: primary GEOS-5 aerosol type selected for 1 July 2016 0Z. Aerosol types are dust (DU), sea salt (SS), black carbon (BC), organic carbon (OC), and sulfate (SU).

The methodology for selecting which two (of the five) aerosol types to be included in the state vector is simply sorting them by AOD at 760 nm and selecting the two largest values. The ice cloud, water cloud, and stratospheric aerosol type were always retrieved. The ice cloud and water cloud characteristics were kept the same as B8, while the stratospheric aerosol's optical depth prior and corresponding uncertainty were determined by our setups described below.

2.4.1 Types and Optical Depths

The first method simply takes the top two aerosol types based on sorting by each type's AOD and uses their corresponding AODs as prior information for each type. This method is the simplest of our tests and does not rely on any modeled vertical aerosol information.

2.4.2 Types and Gaussian Fits

The second method takes the largest two aerosol types, as before. The 72-layer GEOS-5 aerosol profiles for both types are then interpolated onto the 20-layer OCO-2 vertical grid. The amplitude, mean, and variance of a Gaussian curve are then fit to that 20-layer profile and the amplitude (optical depth), height, and width of that Gaussian are fed in to the retrieval as prior information. An example is shown in Figure 2.4. Occasionally, the fit is a poor representation of the vertical profile. This is often the case with the sulfate type, which can have both a lower tropospheric peak and a stratospheric peak, resulting in a profile that cannot be represented with a single Gaussian. To avoid this issue, the sulfate type, if selected, was fit to below 400 hPa and the stratospheric aerosol type (discussed in Section 1.6.1) was a separate Gaussian fit for the profile above 400 hPa. This method was chosen to test the hypothesis that ingesting vertical information from the model will lead to an improved parameterization of the scattering and, subsequently, a more accurate X_{CO_2}.

2.4.3 Types and Scale Factors

The third and most complex method takes the largest two aerosol types sorted by AOD, as before. The 72-layer GEOS-5 aerosol profiles for both types are then interpolated onto the 20-layer OCO-2 vertical grid. A scale factor applied to the interpolated profile is then solved for

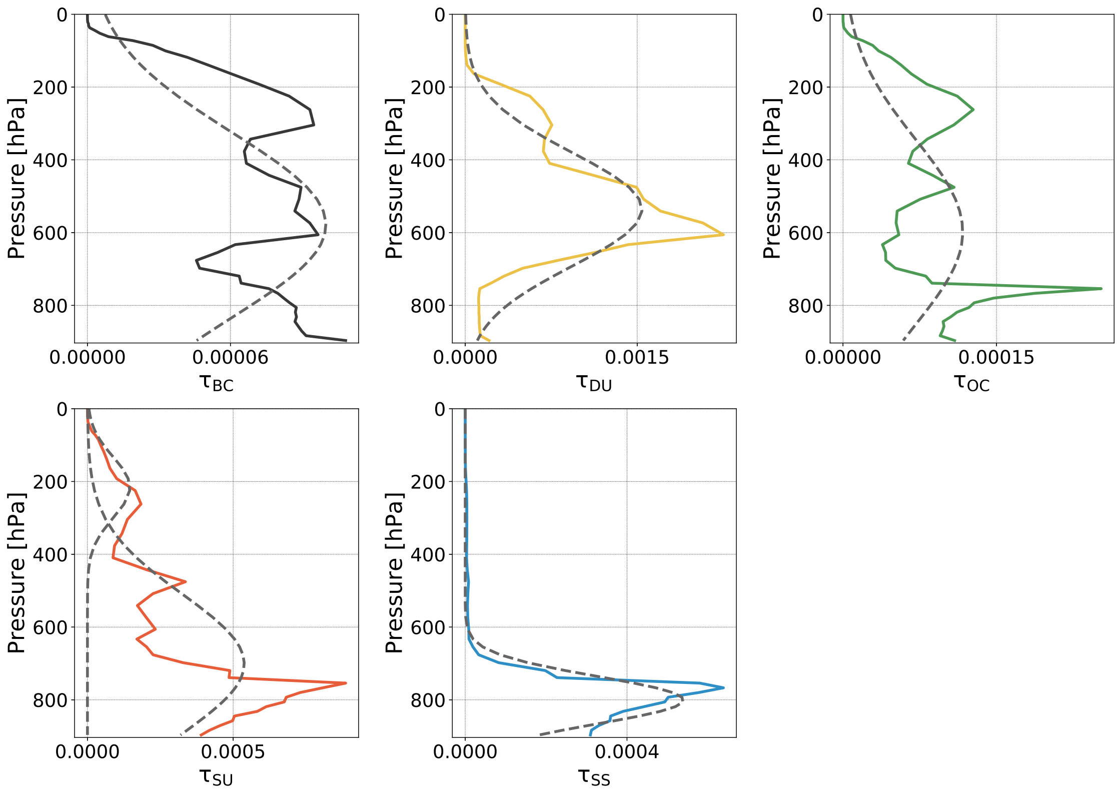

Figure 2.4: Example of fitting Gaussians to the GEOS-5 AOD profiles. Upper row is black carbon (black), dust (yellow), and organic carbon (green). Lower row is sulfate (orange) and sea salt (blue). Dashed grey lines are the Gaussian fits to the profiles.

by the retrieval. Because the ACOS retrieval solves for the natural log of the AOD, we solve for an additive scalar which acts as a multiplicative scaling factor when converted to AOD. This means that if the retrieval determines that the scale factor should be 1.5, the GEOS-5 AOD profile magnitude will be multiplied by 1.5. This method is similar to that of [76], except here we are using a vertical aerosol profile co-located in time and space as the prior, while they use a constant aerosol profile. This method was chosen to test the hypothesis that Gaussian fits are insufficient to realistically parameterize the shapes of true vertical aerosol profiles in the X_{CO_2} retrieval.

2.4.4 Aerosol Prior Uncertainties

In addition to these three techniques used to modify the aerosol priors, the prior uncertainty must also be considered when using optimal estimation. In the operational ACOS X_{CO_2} retrieval algorithm, the uncertainty on the aerosol parameters is typically very loose. For example, a prior AOD (τ) of 0.1 is approximately -2.3 in ln-space. Assigning the B8 uncertainty of 2.0 to ln(τ) gives 1-sigma values of -4.3 and -0.3 in ln-space, which equates to about 0.014 and 0.74 in optical depth. This large prior uncertainty is due to the lack of confidence in the monthly climatological priors and because it is believed that the radiances themselves should provide enough information to properly constrain the results. However, using this new instantaneous setup allows us to decrease the prior uncertainty because we have more confidence in the GEOS-5 model compared to the monthly climatology, as demonstrated by Figure 2.2. The three setups chosen to test are using the operational uncertainty (“high uncertainty"), 25% of the operational uncertainty (“low uncertainty"), and fixing the prior aerosol values (“no uncertainty"). For example, using our first method above (Section 2.4.1) with low uncertainty means solving for the AODs of the two selected aerosol types with 25% of the operational uncertainty assigned to the prior values. This means that instead of a 1-sigma uncertainty of 2.0 on ln(τ), we assign a value of 0.5. This equates to a 1-sigma uncertainty range of between 0.06 and 0.16 on a prior AOD of 0.1. Table 2.2 lists all the test setups and the corresponding uncertainties on the retrieved ln(τ) and, except for the scalar profile tests, the retrieved height. The third method, solving for a 20-layer profile (Section 2.4.3), does not lend itself to assigning single values of uncertainty equivalent to the other two setups. Thus, we assigned layer uncertainties of ln(10), 0.5, and 0.001 for each layer to represent the operational, low, and fixed setups. We also ran the operational retrieval with low and no uncertainty on the AODs in an attempt to isolate the impact of only modifying the prior uncertainties. When ingesting vertical information in the second and third methods, we also reduced the uncertainty of the retrieved height. The width was effectively never retrieved, as it was always assigned an uncertainty of 0.001.

Table 2.2: Prior uncertainties of retrieved ln(τ) and heights (H) for all retrieval variants. The first entry (B8 + MERRA-2 Climatological Types & AODs with high uncertainty) is equivalent to the operational ACOS retrieval uncertainties. The prior 1-sigma uncertainties on the natural log of the stratospheric AOD are slightly lower, at 1.8, 0.45, and 0.001 for the three uncertainty levels, respectively.

Retrieval Type	High Uncertainty	Low Uncertainty	No Uncertainty
B8 + MERRA-2 Climatological Types & AODs	σ_τ=2.0, σ_H=0.2	σ_τ=0.5, σ_H=0.2	σ_τ=0.001, σ_H=0.2
B8 + GEOS-5 Types & AODs	σ_τ=2.0, σ_H=0.2	σ_τ=0.5, σ_H=0.2	σ_τ=0.001, σ_H=0.2
B8 + GEOS-5 Types & Gaussian AODs/Heights	σ_τ=2.0, σ_H=0.2	σ_τ=0.5, σ_H=0.05	σ_τ=0.001, σ_H=0.0001
B8 + GEOS-5 Types & Scalar Profile	$\sigma_{\tau,\ layer}$=$\ln 10$	$\sigma_{\tau,\ layer}$=0.5	$\sigma_{\tau,\ layer}$=0.01

After processing all 12 retrieval variants, applying similar post-filtering, and matching retrievals to ensure a fair comparison, 19,471 retrievals remained in the TCCON validation dataset while 17,355 retrievals remained in the model validation dataset. For both datasets and all tests, there were no significant outliers when it came to the percentage of retrievals that converged or remained after post-filtering. Typically, the setups with loose priors had slightly more retrievals fail to converge and the more complex schemes lost more retrievals in post-filtering, but only by a few hundred.

2.5 Results

In this section we discuss the impact of using better informed aerosol priors in the OCO-2 $X_{\mathrm{CO_2}}$ retrieval by comparing our test setups to both TCCON and an ensemble of global $X_{\mathrm{CO_2}}$ models.

2.5.1 TCCON Validation Results

Figure 2.5 shows the results of our test setups alongside the operational retrieval variants (top row). Here, we can see the impact that different prior information and different prior uncertainties have on the retrieved $X_{\mathrm{CO_2}}$ when compared to TCCON.

For our nine GEOS-5 test setups, when examining the standard deviation of the error (σ), correlation coefficient (R), and mean absolute error (MAE) versus TCCON, the values are typically best for the setups where only the types and the AODs are ingested (second row). When we apply a Gaussian fit to the modeled profiles and use those heights and widths as priors (third row), we see an increase in the scatter against our validation source along with a worse MAE and R. Finally, when we solve for a scalar on the modeled aerosol profile (bottom row), we see the largest scatter in $X_{\mathrm{CO_2}}$ against TCCON, worst correlations, and highest MAEs. It therefore appears that trying to incorporate vertical information from the aerosol model leads to a worse $X_{\mathrm{CO_2}}$.

The only GEOS-5 test setup with errors and a correlation coefficient better than the operational retrieval is the middle panel of the second row (green triangles), where the types and AODs were ingested with low uncertainty. This may indicate that it is reasonable to assign some confidence

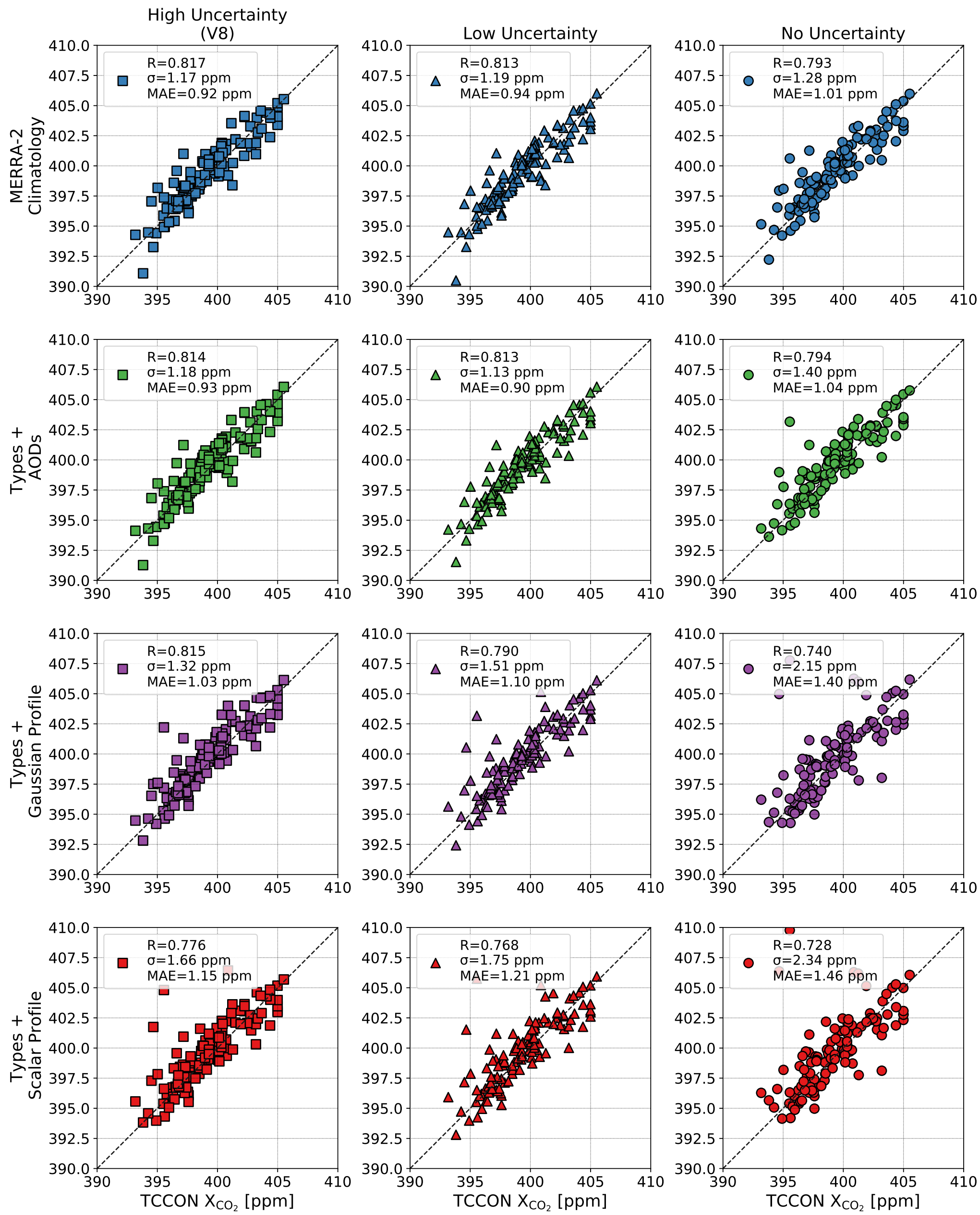

Figure 2.5: Retrieved OCO-2 X_{CO_2} (y-axes) against TCCON X_{CO_2} (x-axes). Overpass means are plotted. The first row is the operational retrieval (B8). The second row is ingesting GEOS-5 types and AODs, the third row is ingesting GEOS-5 types and Gaussian profile priors, and the fourth row is ingesting GEOS-5 types and solving for a scalar to the prior aerosol profile. The left column is high uncertainty, the middle column is low uncertainty, and the right column is no uncertainty (see Table 2.2). For each panel, R is the correlation coefficient, σ is the standard deviation of the error against TCCON, and MAE is the mean absolute error against TCCON.

in the modeled AODs from GEOS-5, rather than leaving it mostly unconstrained. The operational retrieval with low uncertainty (blue triangles) does relatively well, but slightly worse than the original B8 (blue squares).

For all retrieval setups, fixing the aerosol input (right column) results in worse error statistics. This is likely because models are not perfect and by entirely removing the retrieval's ability to fit for aerosol effects on the radiances it results in large errors in X_{CO_2}. Keeping the prior aerosol uncertainty the same as the operational retrieval (left column), however, appears to allow too much freedom and the aerosol parameters revert to the operational values, regardless of what the prior values are. This is because we are assigning almost no confidence to the prior, so all the information comes from the retrieval. This shows the utility of having semi-constrained aerosol priors to guide the X_{CO_2} retrieval algorithm. The only row where the low uncertainty test does better than the high uncertainty test is when we ingest types and AODs. This again indicates that it may be beneficial to use GEOS-5 modeled types and AODs and assign them some level of confidence that is greater than the B8 constraint.

2.5.2 Model Validation Results

While TCCON gives a robust estimate of the statistical errors for our test setups, it does not allow for regional analysis because of the sparsity of the network. The CO_2 model median validation technique, described in Section 2.2.2, allows for an assessment of regional errors in the test setups compared to a truth metric. For this work, the most promising aerosol setup in the TCCON validation study was selected for further analysis. That is, ingesting the GEOS-5 types and AODs with low uncertainty. Figure 2.6 shows the operational (B8) X_{CO_2} error and the GEOS-5 aerosol prior setup X_{CO_2} error while the top panel of Figure 2.7 shows the difference of the absolute value of the X_{CO_2} errors for the two setups.

Here, regional differences can be seen. Over Northern Africa and Central Asia the operational retrieval (top panel of Figure 2.6) is often biased high, which results in a large X_{CO_2} scatter in those regions. The GEOS-5 aerosol setup (bottom panel of Figure 2.6), however, shows that those high

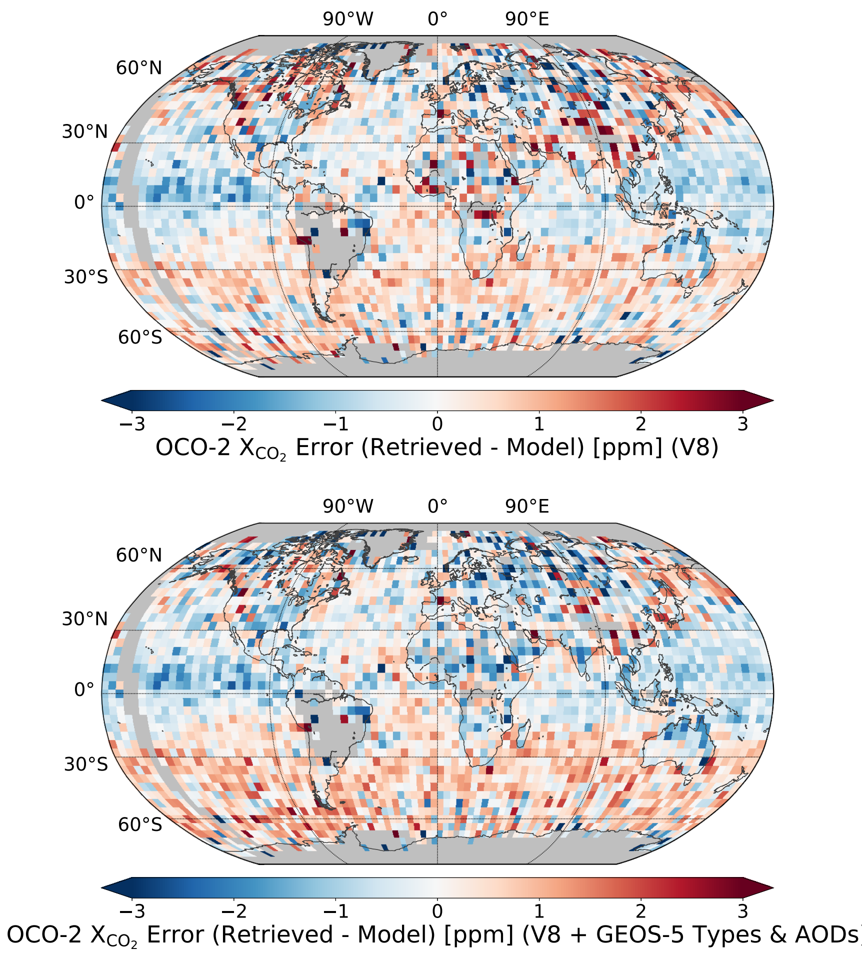

Figure 2.6: Top: 4°x4° binned $X_{\mathrm{CO_2}}$ error against model validation for B8. Bottom: 4°x4° binned $X_{\mathrm{CO_2}}$ error against model validation for the GEOS-5 types & AODs with low uncertainty setup. Grey bins represent no data.

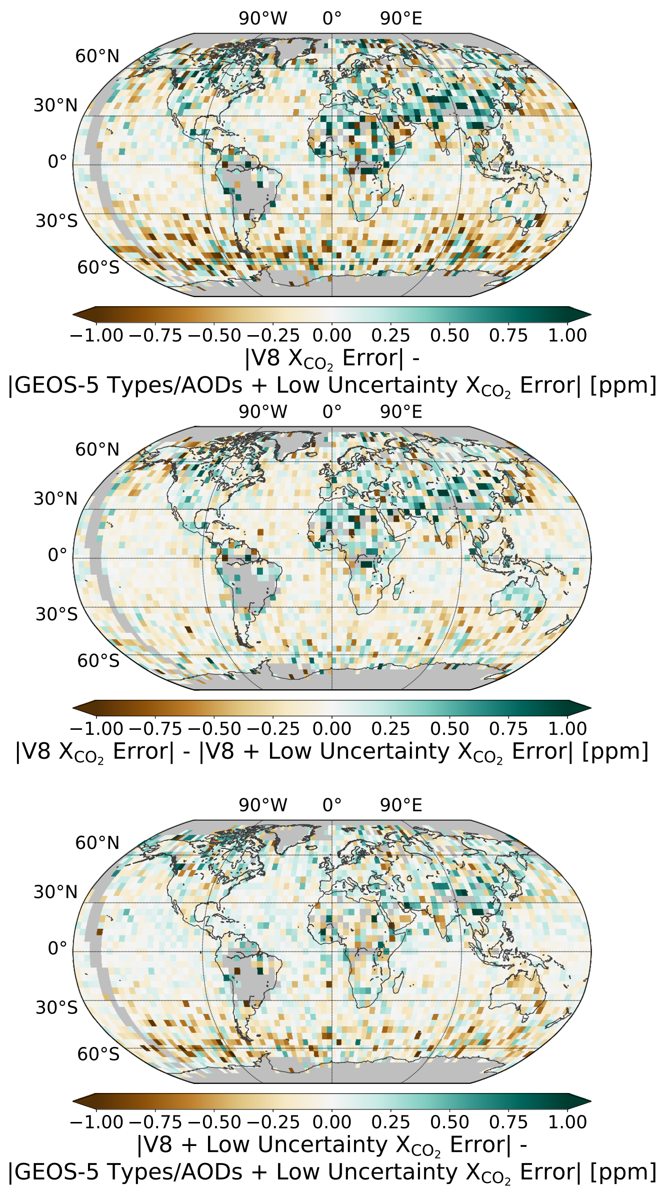

Figure 2.7: Top: 4°x4° binned absolute value of B8 X_{CO_2} error against the model validation minus the absolute value of the GEOS-5 Types & AODs with low uncertainty X_{CO_2} error against the model validation. Middle: 4°x4° binned absolute value of B8 X_{CO_2} error against the model validation minus the absolute value of B8 with low uncertainty X_{CO_2} error against the model validation. Bottom: 4°x4° binned absolute value of B8 with low uncertainty X_{CO_2} error against the model validation minus the absolute value of GEOS-5 Types & AODs with low uncertainty X_{CO_2} error against the model validation. Green grid cells represent an improvement relative to the model validation while brown grid cells represent a worse comparison. Grey bins represent no data.

biased bins have mostly been removed. The difference plot (top panel of Figure 2.7) demonstrates an improvement in the error of around 1 ppm for many grid cells in Northern Africa and Central Asia. An additional regional difference is in the Southern Ocean, where the GEOS-5 aerosol setup develops a new high bias of 0.4 ppm in many of the bins, compared to B8 which has a bias of nearly zero (+0.1 ppm). Over the remaining land and ocean regions there is minimal change in X_{CO_2} between the two datasets. While of interest, comparing retrieval setups over the Amazon and high latitudes is difficult due to the lack of measurements. This is because these regions are typically cloudy around solar noon or lack the necessary amount of reflected sunlight to make an accurate retrieval, respectively, so they have been filtered out.

Regarding the plots just discussed, three factors could be contributing to the regional changes in X_{CO_2} between B8 and the GEOS-5 aerosol prior setup. First, the decrease in prior uncertainty to 25% of B8. Second, the two selected aerosol types. Third, the modified AOD priors of the two aerosol types. In order to isolate the first effect, the middle panel of Figure 2.7 shows a comparison between B8 and B8 with low uncertainty. Here, we can see that the impact of simply reducing the prior uncertainty on the retrieved AODs is substantial and accounts for a considerable portion of the improvement over Northern Africa and Central Asia, with the standard deviation of the error being reduced from 2.12 ppm to 1.92 ppm. The ocean remains nearly unchanged, along with much of the remaining land surface.

Now that we have isolated the impact of reducing uncertainty, we can compare B8 with low uncertainty to GEOS-5 types & AODs with low uncertainty to determine what impact, if any, using the constrained GEOS-5 aerosol types and priors has on the X_{CO_2} error. The bottom panel of Figure 2.7 shows that this change is beneficial over Central Asia ($\sigma_{X_{\mathrm{CO}_2}\ error}$ reduced from 2.07 ppm to 1.94 ppm for measurements over land between latitudes 16 N and 56 N and longitudes 52 E and 152 E), has a minimal effect over the Northern Africa ($\sigma_{X_{\mathrm{CO}_2}\ error}$ changed from 1.63 ppm to 1.62 ppm for measurements over land between latitudes 6 S and 38 N and longitudes 20 W and 52 E), and a detrimental effect over the Southern Ocean ($\sigma_{X_{\mathrm{CO}_2}\ error}$ increased from 1.86 ppm to 1.95 ppm and a positive bias of 0.4 ppm for measurements south of 45 S). This suggests that the improvement in the scatter of the $X_{\mathrm{CO_2}}$ error against model validation over the Northern Africa was primarily due to the reduction in uncertainty in the prior AODs, and not the co-located GEOS-5 aerosol prior types and values themselves. Over Central Asia, however, the improvement seems to be a combination of reducing the uncertainty and using instantaneous types and/or AODs. Over the Southern Ocean, using GEOS-5 types and prior AODs results in an increase in scatter and a high bias of 0.4 ppm.

Next, we attempt to distinguish between the impact of using GEOS-5 aerosol types and using their corresponding AODs as prior information. The areas of interest are Central Asia, where using instantaneous priors improved the $X_{\mathrm{CO_2}}$ retrieval, and the Southern Ocean, where it worsened the $X_{\mathrm{CO_2}}$ retrieval. The top panel of Figure 2.8 shows the binned prior AOD for B8, which is derived from a monthly MERRA-2 climatology (as discussed in Section 1.6.1), while the bottom panel shows the binned prior AOD for our test setup which uses the co-located GEOS-5 modeled data. In general, slightly more variation is seen in the GEOS-5 priors, which is to be expected, as the monthly climatology is a mean of an entire month and thus removes most synoptic variability. The most prominent change, however, is the significant reduction in prior AOD over Northern Africa and Central Asia. The GEOS-5 aerosol setup has a 30% lower mean prior AOD than B8. This is likely because the MERRA-2 climatology was created by simply averaging an entire month of data together, including all instances where the optical depth was large due to dust storms, pollution events, biomass burning, etc. Those scenes, however, are typically removed by OCO-2's pre-screeners (ABP and IDP, described in Section 2.3) before being processed through the retrieval code and thus the GEOS-5 prior map only includes scenes that were determined to be sufficiently clear to perform retrievals on. This suggests that the MERRA-2 monthly climatology aerosol prior may be artificially high and not entirely appropriate for use in the operational retrieval algorithm. This is also seen in Figure 2.2, where there are several MERRA-2 climatology AODs that are significantly high biased against AERONET. Figure 2.2, however, is only data from 13 AERONET sites and is thus not representative of the global differences.

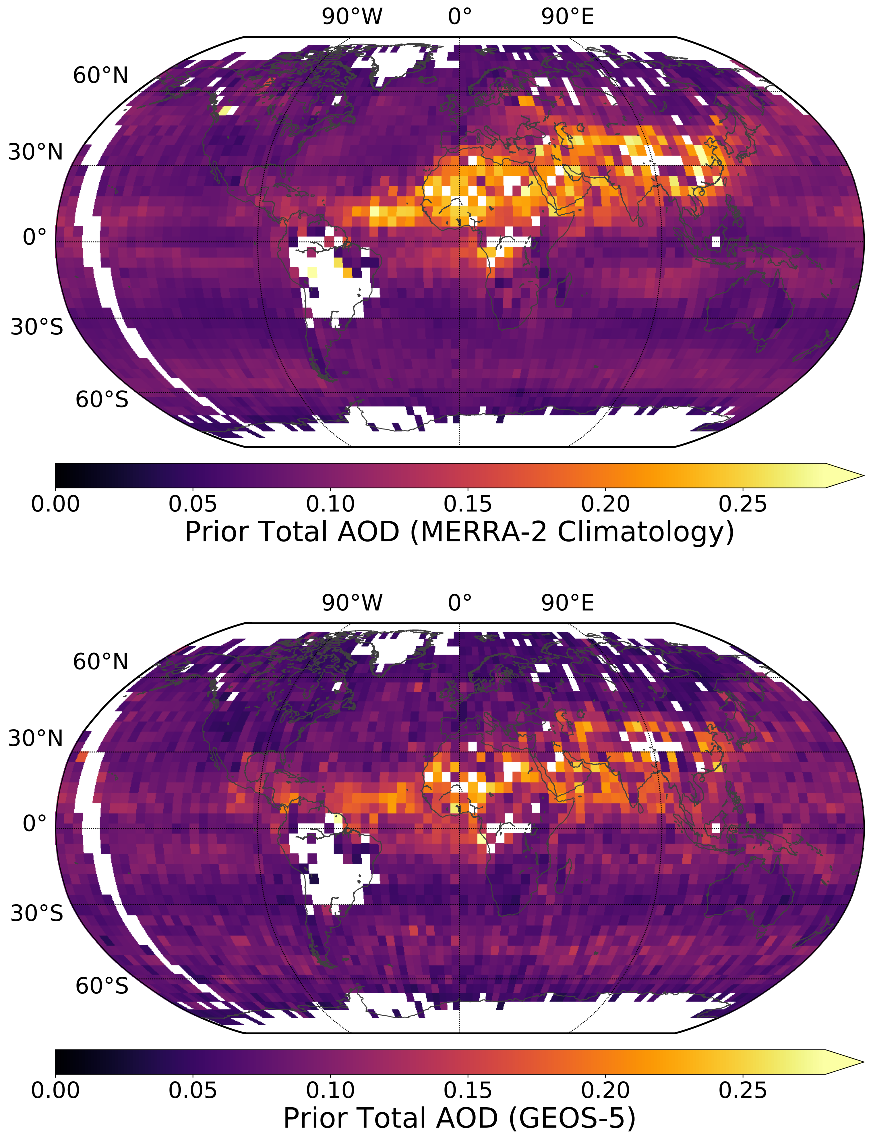

Figure 2.8: Top: 4°x4° binned prior AOD for B8, derived from a MERRA-2 monthly climatology. Bottom: 4°x4° binned prior AOD for B8 + GEOS-5 Types & AODs with low uncertainty, derived from co-located GEOS-5 AODs. White bins represent no data.

In optimal estimation the final, optimized state vector represents a weighted combination of the prior information and the measurement, not just the state of the prior. The top panel of Figure 2.9 shows the retrieved AOD for B8 while the bottom panel shows the retrieved AOD for the GEOS-5 aerosol setup. Here, we see an even more dramatic difference in retrieved AODs over the Northern Africa and Central Asia. Over land in these two regions, the retrieved AOD is 52% lower for the GEOS-5 aerosol setup. This is partially due to the reduced uncertainty on the prior AODs for the GEOS-5 aerosol setup, which prevents it from deviating substantially from the prior.

While the differences in X_{CO_2} over Central Asia correlate with a large difference in the magnitude of the retrieved AOD, the same cannot be said of the X_{CO_2} differences over the Southern Ocean, as those differences in retrieved AOD are small (8.9% increase in the GEOS-5 test setup over the Southern Ocean). Additionally, the middle panel of Figure 2.7 demonstrated that the reduction in uncertainty alone had a minimal impact on this region.

The changing of one or both of the aerosol types when going from the MERRA-2 monthly climatology to the instantaneous GEOS-5 setup could be the explanation for the positive 0.4 ppm bias in X_{CO_2}. Of the 17,355 global retrievals remaining after post-filtering, 32% have one or both aerosol types different while only 0.7% have both aerosol types different. To test this hypothesis, we ran an additional set of retrievals similar to the GEOS-5 types & AODs with low uncertainty, but not changing the types. Figure 2.10 demonstrates that changing the types has almost no effect on the Southern Ocean and overall has a small and sporadic effect (note the reduced scale). The mean difference between ingesting GEOS-5 AODs and types and only ingesting GEOS-5 AODs for retrievals where the type actually changed is about 0.01 ppm with a standard deviation of about 0.2 ppm. Only a small fraction of retrievals had X_{CO_2} differences larger than 0.5 ppm (2.3% of all retrievals). Thus, the selection of an appropriate AOD prior and uncertainty is much more important than the exact aerosol properties in our retrieval parameterization.

After further investigation, the modification to the stratospheric aerosol prior and its corresponding uncertainty is likely the cause of the Southern Ocean 0.4 ppm high bias in the GEOS-5 aerosol setup. As detailed in [60], ACOS B7 contained a high bias over water at high southern

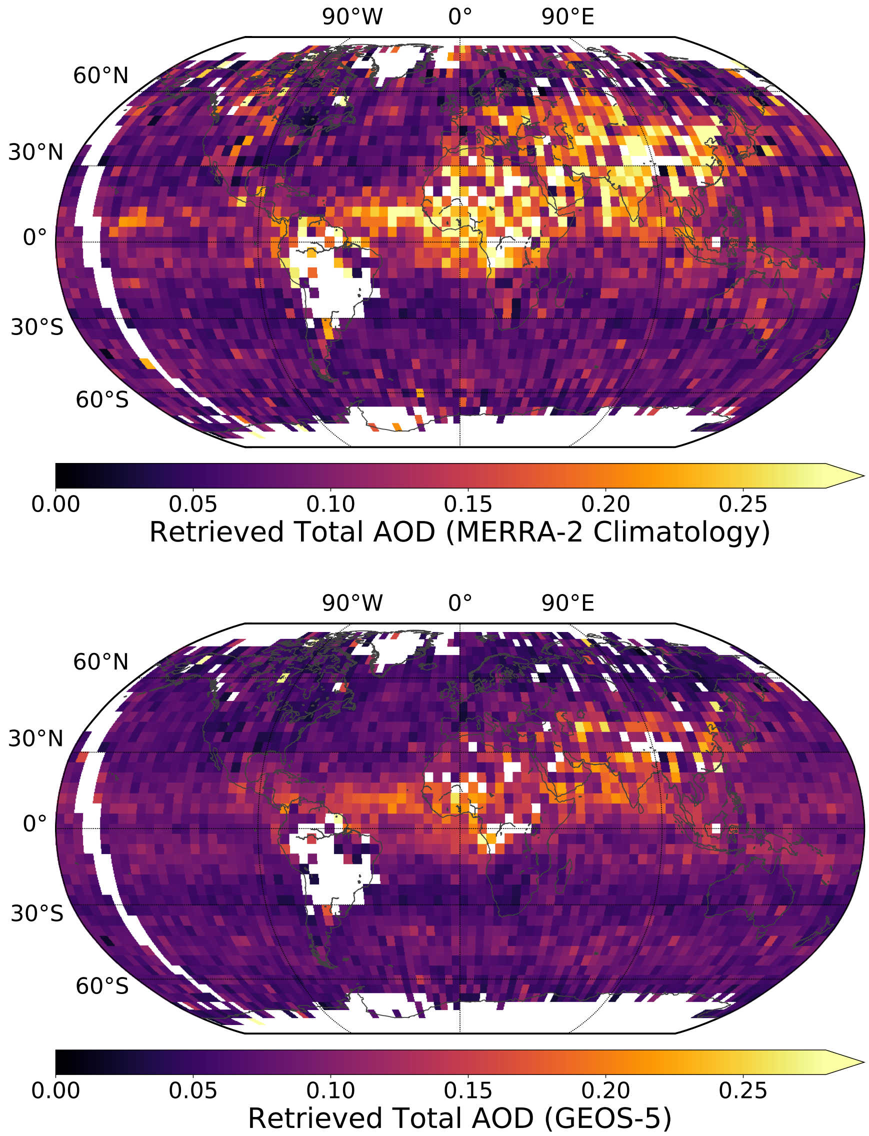

Figure 2.9: Top: 4°x4° binned retrieved AOD for B8. Bottom: 4°x4° binned retrieved AOD for B8 + GEOS-5 Types & AODs with low uncertainty. White bins represent no data.

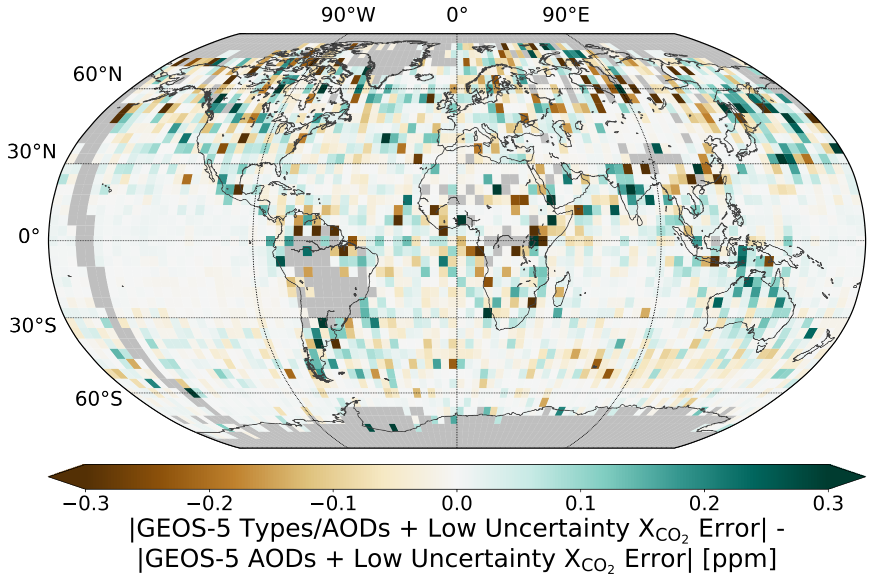

Figure 2.10: 4°x4° binned absolute value of GEOS-5 Types & AODs with low uncertainty $X_{\mathrm{CO_2}}$ error against the model validation minus the absolute value of GEOS-5 AODs with low uncertainty $X_{\mathrm{CO_2}}$ error against the model validation. Green grid cells represent an improvement relative to the model validation while brown grid cells represent a worse comparison to the model validation. Grey bins represent no data.

latitudes due to both the presence of stratospheric aerosol from the Calbuco eruption in 2015 as well as ice build up on the OCO-2 focal plane arrays. Here, we have unintentionally replicated this issue, as the stratospheric aerosol priors from GEOS-5 are near zero (as opposed to a global prior value of 0.006 used in B8). Figure 2.11 demonstrates that when B8 solves for a large stratospheric AOD in the Southern Ocean, GEOS-5 cannot because it starts with a lower prior and is unable to sufficiently increase it. This result in a significant positive bias in $X_{\mathrm{CO_2}}$ (bottom of Figure 2.6). When the retrieved B8 stratospheric AOD is greater than 0.012 in the Southern Ocean, the GEOS-5 aerosol setup incurs a positive bias of approximately 1.4 ppm (compared to the positive 0.4 ppm bias for all Southern Ocean retrievals). This indicates that in measurements where large stratospheric AODs are needed to fit the radiances, the lack of AOD usually appears to lead to a high bias in $X_{\mathrm{CO_2}}$.

To further test this hypothesis, we ran a set of retrievals where we reverted the stratospheric aerosol prior AOD and prior uncertainty back to B8 values (0.006 and a 1-sigma uncertainty on

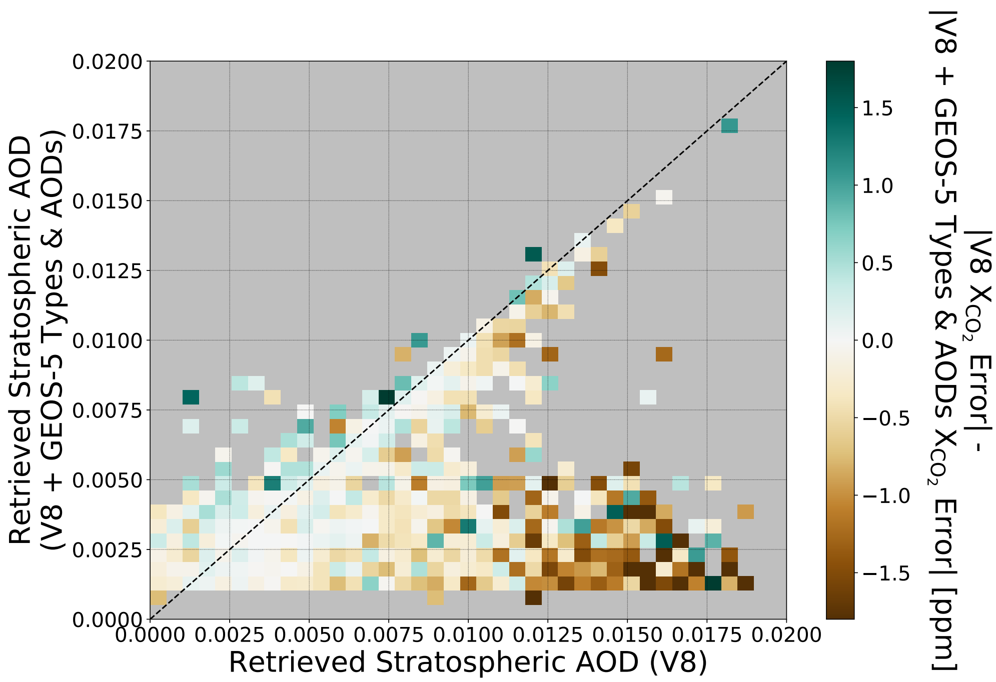

Figure 2.11: Retrieved stratospheric AOD from B8 versus retrieved stratospheric AOD from B8 + GEOS-5 Types & AODs with low uncertainty for the Southern Ocean. Color represents the change in the absolute value of the $X_{\mathrm{CO_2}}$ error between the two retrieval types, where green demonstrates an improvement over B8 and brown represents a worsening.

the ln(AOD) of 1.8). This revealed that the 0.4 ppm bias in the Southern Ocean mostly disappears, as the high bias is reduced back to approximately +0.1 ppm, in agreement with B8.

2.6 Conclusions

In this study we investigated the impact of using better informed aerosol priors in the OCO-2 ACOS X_{CO_2} retrieval algorithm applied to real measurements. We ingested aerosol information from co-located GEOS-5 model data with varying levels of uncertainty and compared to two validation sources, TCCON and a global CO_2 model suite.

We found that ingesting instantaneous AOD information with low uncertainty slightly reduced the standard deviation of the X_{CO_2} error against TCCON from 1.17 ppm to 1.13 ppm. More interestingly, we found that attempting to ingest vertical information from GEOS-5 produced poor results against TCCON, with mean absolute errors more than 50% larger than B8. We hypothesize that this is because accurate vertical placement of aerosol layers still represents a significant challenge in global aerosol models [109]. This is due to the large uncertainty in processes related to how aerosols are distributed vertically, partially because of the lack of constraint by global observations [110]. Additionally, fixing the ingested aerosol information also makes the retrieval compare poorly to TCCON. This is, again, because the priors will always be imperfect, so the OCO-2 ACOS X_{CO_2} retrieval algorithm needs some amount of freedom to adjust the radiances.

A comparison to our model validation dataset reveals an improvement over Northern Africa and Central Asia when using the GEOS-5 types and AODs with low uncertainty compared to B8, with the scatter in X_{CO_2} error being reduced from 2.12 ppm to 1.83 ppm. Additionally, we see a new high bias in X_{CO_2} of 0.4 ppm over the Southern Ocean. These regional differences in OCO-2 B8 compared to the GEOS-5 type and AOD low uncertainty prior test setup are likely caused by one of the three modifications. First, reducing the uncertainty on the prior AODs in B8 results in an improvement over Northern Africa and Central Asia. Figure 2.12 shows that by constraining the prior AODs in B8, we prevent the algorithm from retrieving large AODs. Those retrievals that solved for large AODs in B8 but smaller AODs in the low uncertainty setup generally have smaller

X_{CO_2} errors (green pixels in Figure 2.12). For retrievals where the B8 AOD is greater than 0.4 over Northern Africa and Central Asia, constraining the prior AODs with low uncertainty reduces the X_{CO_2} bias against the validation dataset by 0.55 ppm on average. Some retrievals are outliers, in that they do worse when constrained (brown pixels in Figure 2.12). Around 8% of the retrievals have an X_{CO_2} error increase of greater than 0.5 ppm. This may be because those scenes actually contain large AODs and thus constraining the priors is hindering the retrieval's ability to properly fit the radiances, but further investigation is needed on this topic.

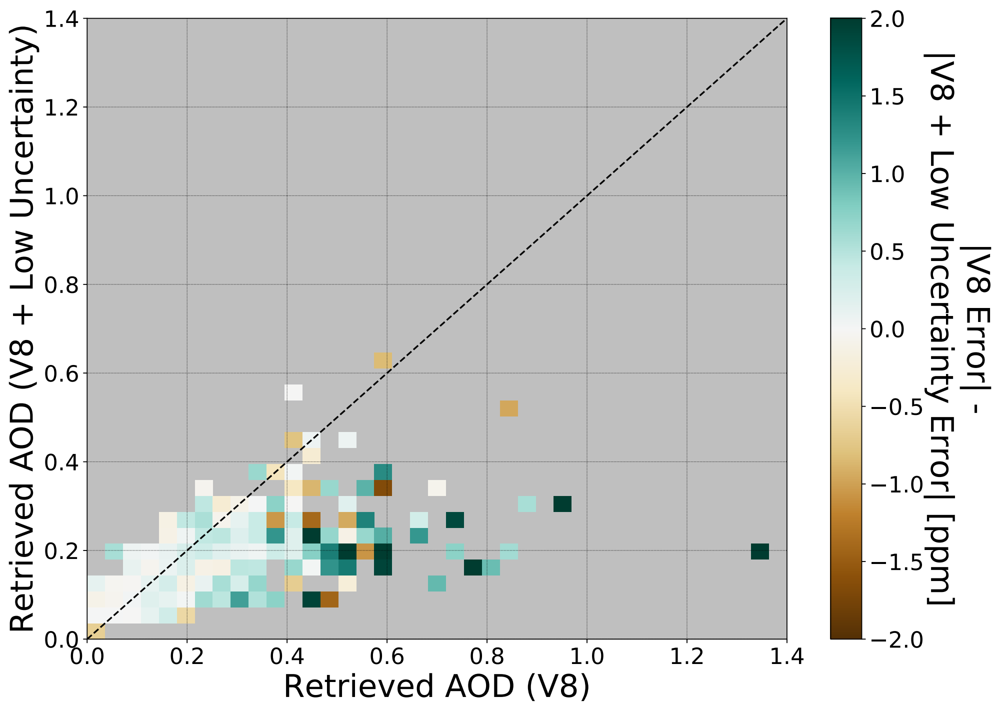

Figure 2.12: Retrieved AOD from B8 versus retrieved AOD from B8 with low uncertainty for North Africa and Central Asia. Color represents the change in the absolute value of the X_{CO_2} error between the two retrieval types, where green demonstrates an improvement over B8 and brown represents a worsening.

Second, some of the high bias seen in B8 (top panel of Figure 2.6) is likely due to the MERRA-2 climatological priors being unrealistically high for the selected OCO-2 measurements. Physically, when there is too much aerosol being retrieved, the CO_2 absorption lines are filled in too much because the retrieval thinks those photons are experiencing a shorter path length than they are in reality. The retrieval then must add more CO_2 to deepen the absorption lines again to match the measured line depths. This results in the observed high bias in B8 over Central Asia, which is mostly removed when smaller, more appropriate AOD priors are taken from the GEOS-5 dataset (bottom panel of Figure 2.7). However, the bottom panel of Figure 2.7 also showed that using lower AOD priors alone had no significant net impact on Northern Africa. This difference may be due to Northern Africa having a higher surface albedo than Central Asia. This results in a larger fraction of the signal coming from the surface and less weight placed on any aerosols present. So long as the retrieved aerosols are not very large, as discussed above, the $X_{\mathrm{CO_2}}$ results over Northern Africa may be less sensitive to the aerosol prior than other regions.

Third, the GEOS-5 types & AODs with low uncertainty setup resulted in a new high bias of 0.4 ppm in $X_{\mathrm{CO_2}}$ relative to B8 over the Southern Ocean. It was initially hypothesized that the change in aerosol types may have caused the high bias, but we showed that changing one or both of the aerosol types has a minimal impact on the $X_{\mathrm{CO_2}}$ in this setup. After additional tests, we found that the GEOS-5 stratospheric AODs in the Southern Ocean were too small to be able to account for actual stratospheric aerosol in the region along with the effects of an ice accumulation artifact in the OCO-2 radiances. Reverting the stratospheric prior and uncertainty back to that of B8 mostly eliminated the high bias in the Southern Ocean. This conclusion highlights the severe impact that even a small amount of aerosols can have on the retrieved $X_{\mathrm{CO_2}}$.

This work is relevant for several missions set to launch in the near future, including OCO-3, GOSAT-2, MicroCarb, TanSat-2, and GeoCarb. Algorithm development teams will have to decide how they will account for clouds and aerosols in order to minimize errors in their CO_2 measurements. While we have shown the benefits and limitations of using instantaneous modeled aerosol data to inform the OCO-2 $X_{\mathrm{CO_2}}$ retrieval, more work is needed to determine the optimal aerosol parameterization for near-infrared measurements of CO_2. These results may be of use in guiding development for the next version of the OCO-2 ACOS $X_{\mathrm{CO_2}}$ retrieval algorithm.

Chapter 3

Simplified Aerosol Parameterizations in Near-Infrared Retrievals of Carbon Dioxide

3.1 Simplified Aerosol Parameterizations

The primary goal of OCO-2 is to use hyperspectral measurements of reflected near-infrared sunlight to retrieve $X_{\mathrm{CO_2}}$ with high accuracy. This is only possible for measurements of scenes nearly free of clouds and aerosols, but as some contamination will always be present, OCO-2 must include aerosols in its state vector. The current OCO-2 retrieval algorithm contains, among other things, nine parameters related to aerosols. However, there are only 2-6 pieces of information about aerosols in the OCO-2 radiances. Figure 3.1, taken from [82], shows the averaging kernels for various retrieved aerosol properties for multiple OCO-2-like instruments. The near-infrared measurements are most sensitive to the aerosol height, effective radius, optical depth ("aerosol column"), and size distribution width.

In this work, we investigate multiple simplified aerosol schemes in an attempt to minimize errors in $X_{\mathrm{CO_2}}$ by reducing the number of retrieved aerosol parameters to be within the range of actual degrees of freedom. The retrieval variations in this chapter solve for between zero and six aerosol parameters, as opposed to the nine in ACOS B8. The previous version of ACOS, B7, did not include a stratospheric aerosol and thus only contained eight scattering parameters.

The expected benefits of a simplified aerosol parameterization are numerous. The first benefit is faster convergence. This is not because the radiative transfer code is running significantly faster than in the operational ACOS retrieval, but because a retrieval with a simplified state vector tends to meet the convergence criteria after fewer iterations. If the simplified aerosol parameterization can produce similar error statistics to the operational ACOS but with faster convergence, it represents an opportunity to save computational resources. The second benefit is that the re-

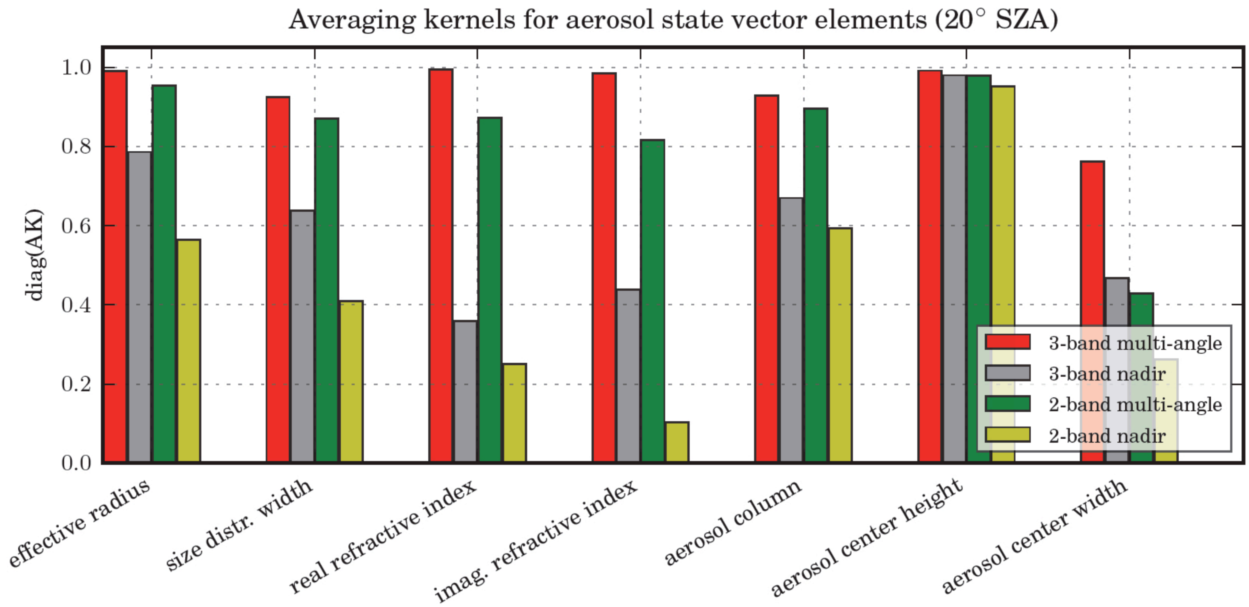

Figure 3.1: Averaging kernel diagonal elements related to aerosols for a solar zenith angle of 20°. Taken from [82].

trieval should be less nonlinear. The retrieval of GHGs from near-infrared measurements is a nonlinear problem, but the ever-growing size of the ACOS state vector [60] has compounded this problem. [111] has shown that small differences in the first guess of certain state vector elements can lead to differences in the final retrieved $X_{\mathrm{CO_2}}$ of several ppm. Reducing the size of the state vector, specifically the number of elements related to aerosols, is hypothesized to reduce the nonlinearity of the forward model. However, we do not explicitly test this hypothesis in this work. The third benefit of a simplified aerosol parameterization is greater throughput. In ACOS B8, around 10-20% of retrievals that had passed the preprocessors (discussed in Section 1.5.2) still fail to converge [60]. Many of these retrievals are unable to find a sufficient minimum in the cost function due to nonlinearity in the forward model. Less nonlinearity could lead to the addition of many successfully retrieved $X_{\mathrm{CO_2}}$ measurements that would have failed to converge otherwise. Additionally, [112] found that nonlinearity in the retrieval system results in $X_{\mathrm{CO_2}}$ errors of 0.9 ppm for synthetic OCO-2 measurements. Finally, a simplified aerosol scheme would lead to more interpretable aerosol results. In the current ACOS scheme, there is significant correlation between the aerosol parameters which means the results are often physically implausible or uninterpretable.

An aerosol parameterization with only a few parameters might allow for a more straightforward validation of the retrieved aerosol variables. Additionally, the bias correction applied to ACOS B8 uses an ad-hoc mixture of several retrieved aerosol parameters. Simplifying this would allow for a simpler bias correction setup.

In the following work, three simplified $X_{\mathrm{CO_2}}$ retrieval aerosol parameterizations are investigated:

- Two-band non-scattering retrieval
- One layer aerosol model
- Two layer aerosol model

The first and most simplistic method tested in this work is a two-band non-scattering retrieval. In this setup, no cloud or aerosol parameters were included in the state vector. Additionally, the O_2 A-band was disabled and the surface pressure was not retrieved. Instead, the surface pressure was fixed at the meteorological prior. This was done because in a non-scattering retrieval, the algorithm will attempt to adjust the surface pressure to account for clouds and aerosols modifying the O_2 A-band radiances. It is forced to do this because it has no cloud or aerosol parameters to tune. Rayleigh scattering is kept on, although the effects are small in the weak and strong CO_2 bands. Previous work [67] has shown that even after heavy screening, a non-scattering retrieval does 20-40% worse than its ACOS “full physics" counterpart, in terms of errors relative to the true $X_{\mathrm{CO_2}}$. Thus, this test is included as a simple baseline against which to compare the other aerosol parameterizations.

The second simplified aerosol parameterization is a one layer model. Here, a single scattering layer is placed in the middle of the atmosphere at 0.5 times the prior surface pressure. The vertical distribution is described by a Gaussian, given by Equation 1.9. The optical depth of a coarse aerosol type (dust) and fine aerosol type (sulfate) are solved for, along with the height of the layer. The types are the aggregated MERRA-2 types, described in Section 1.6.1. The width of the Gaussian, as in B8, remains approximately fixed due to a lack of sensitivity [66, 82]. This results in three aerosol parameters in the state vector. This setup is designed to test the hypothesis that a single scattering layer is sufficient to parameterize the true cloud and aerosol scene observed by OCO-2. Additionally, this setup is similar but not identical to the aerosol parameterization developed by [75], and thus may serve as a useful comparison.

The third method is a two layer model, containing two Gaussian scattering layers. The first aerosol layer is placed in the lower troposphere (0.9 times surface pressure) and is a mixture of a coarse aerosol (dust) and a fine aerosol (sulfate), designed to account for low-level anthropogenic and natural aerosols. The second layer is placed in the stratosphere (0.03 times surface pressure) and is a mixture of a 70 μm ice cloud and sulfate MERRA-2 type, designed to account for cirrus clouds, stratospheric aerosols, and an icing issue on the OCO-2 detectors [113]. For both layers, the algorithm is allowed to solve for the magnitudes of each type and height of the peak of the Gaussian. For example, in the lower tropospheric layer the optical depth of the coarse type, the optical depth of the fine type, and the height of the mixture are solved for. The same is done for the stratospheric layer. This results in a total of six aerosol parameters being solved for, instead of nine in B8. Figure 3.2 shows a schematic of the two layer model setup.

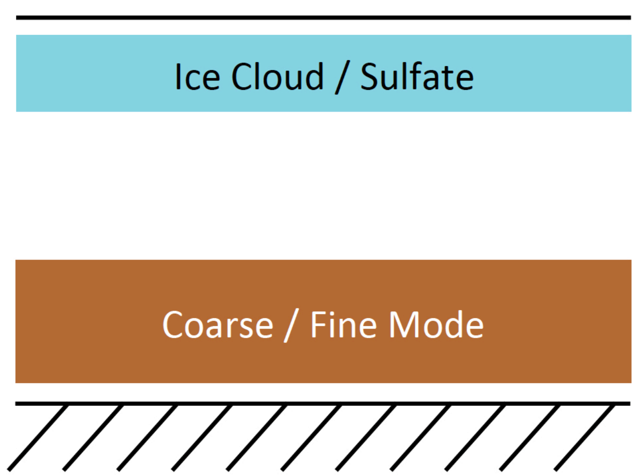

Figure 3.2: Schematic of the two layer aerosol model designed to retrieve fewer aerosol parameters than the operational algorithm.

Table 3.1 describes ACOS B7, B8, and the three simplified aerosol parameterizations used in this work. ACOS B7 is included to further investigate the impact of the stratospheric aerosol component added in ACOS B8.

Table 3.1: Setup of the retrievals used in this work.

Retrieval	Retrieve Aerosols?	# Layers	# Aerosol Parameters
ACOS B7	Yes	4	8
ACOS B8	Yes	5	9
Two-band non-scattering	No	0	0
One layer model	Yes	1	3
Two layer model	Yes	2	6

3.2 Validation Datasets

In order to test these simplified aerosol schemes, two validation experiments were devised. The first was a set of synthetic OCO-2 observations designed to span a range of realistic aerosol profiles, viewing geometries, and surface albedos. The second was a set of real OCO-2 measurements co-located with a highly accurate validation source (TCCON).

3.2.1 Synthetic Dataset

To examine the theoretical expected benefits of simplified aerosol parameterizations, a synthetic OCO-2 dataset was created where the true $X_{\mathrm{CO_2}}$ was known. This synthetic dataset was designed to cover the full range of physical cloud and aerosol optical depths, heights, and types. Additionally, three different surface albedos and three different solar zenith angles were selected. Table 3.2 lists the exact values of the parameters used to create the synthetic observations. For example, the first synthetic observation had an optical depth of 0.0, Gaussian height of 1.0 times the surface pressure, an ice cloud type, a solar zenith angle (SZA) of 25°, and a surface albedo of 0.18 in the O_2 A-band, 0.25 in the weak CO_2 band, and 0.15 in the strong CO_2 band. Note that the height of the Gaussian and scattering type are redundant in this example, because the optical depth is 0.0. Thus, by spanning all the parameters we create a matrix of 2,646 synthetic observations (7 * 6 * 7 * 3 * 3).

Table 3.2: Setup of the synthetic OCO-2 observations. A synthetic observation was created for every possible combination of parameters listed.

Parameter	# of Values	Value(s)
Optical Depth	7	0.0, 0.01, 0.05, 0.1, 0.2, 0.3, 0.5
Gaussian Height[1]	6	1.0, 0.9, 0.5, 0.3, 0.1, 0.01
Gaussian Width	1	Fixed at 0.05
Type	7	Ice cloud, water cloud, dust, sulfate, sea salt, organic carbon, black carbon
Solar Zenith Angle	3	25°, 45°, 60°
Surface Albedo[2]	3	(0.18,0.25,0.15), (0.20,0.20,0.09), (0.21,0.29,0.18)
CO_2 Profile	1	Fixed Profile
H_2O Profile	1	Fixed Profile
O_2 Profile	1	Fixed Profile
Temperature Profile	1	Fixed Profile

[1] Surface pressure multiplier.
[2] Values listed for all three bands. Selected to represent savannah, evergreen broadleaf forest, and cropland.

These parameters were selected to approximately span the full range of expected values for state vector elements that are physically correlated with the scene's cloud and aerosol content. For example, we vary the surface albedo because the $X_{\mathrm{CO_2}}$ retrieval can intermingle the retrieved surface albedo and aerosol properties. Thus, it was deemed important to explore the full range of possibilities. The optical depths range from a perfectly clear scene (optical depth of 0.0) to that of a thin cloud or aerosol layer (optical depth of 0.5). It is assumed that the OCO-2 prescreeners, ABP and IDP, would catch any scene with an optical depth greater than 0.5, although this may not be the case for low level clouds. The heights were selected to range from a Gaussian centered at the surface (1.0 times the surface pressure) to centered in the stratosphere (0.01 times the surface pressure). The types are simply the two clouds retrieved by ACOS (ice and water clouds) along with the five possible aggregated aerosol types from MERRA-2. Three solar zenith angles were selected to span the viewing geometry of the instrument. Three surface albedos were selected to represent a few typical surface types across the earth. Because we were interested in how the results vary for different regional surface characteristics, this study was limited to creating synthetic scenes over land, as the ocean's albedo is effectively only a function of wind speed. The width of the cloud or aerosol layer in these synthetic scenes was held fixed, as previous studies and preliminary work showed that the results were mostly insensitive to the width.

We compare our modified retrievals to ACOS B8 in order to determine any improvement or worsening in the errors. While operationally ACOS decides which aerosol types to use based on a monthly climatology, here we have fixed it so dust and sulfate are the two types chosen in order to simplify the interpretation of the results. All retrievals were bias corrected on the difference between the prior and retrieved surface pressure, which, as expected, was highly correlated with the $X_{\mathrm{CO_2}}$ error. Additionally, the synthetic scenes were run through the ABP and IDP (see Section 2.3 for details) to remove scenes that would have been filtered out from the start.

3.2.2 TCCON Validation Dataset

After examining the synthetic results, the logical next step was to test our aerosol parameterizations on real OCO-2 measurements. The TCCON validation dataset contained 32,175 real OCO-2 measurements taken from 17 September 2014 to 2 May 2016. The sites used in this work are shown in Figure 2.1. We co-located the OCO-2 measurements in time and space with AERONET and TCCON to within 1° latitude/longitude and +/- 30 minutes. The measurements were selected from a set of OCO-2 lite files [89], which had been pre-filtered using the ABP (see Section 2.3). Additional custom filters were also applied in an attempt to remove all scenes contaminated by clouds or aerosols. Thus, all these tests are being done on a mostly clear dataset and conclusions cannot be drawn about how our retrieval modifications impact the results if thick cloud or aerosol layers are present.

The simplified aerosol parameterizations are again compared to ACOS B8 to assess any potential improvements in the errors. The aerosol setup for B8 is described in Section 1.6.1. In addition to ACOS B8, the previous version, ACOS B7, was also compared to the test retrievals. The primary difference between B7 and B8 was the addition of a stratospheric aerosol layer in B8. Thus, this comparison is relevant to this study because it allows us to further investigate whether or not the stratospheric aerosol made a positive or negative impact in the ACOS retrieval.

A simple bias correction was applied to each of the five datasets. As in the previous chapter, a single parameter bias correction was selected for simplicity. The parameter chosen was that which has the largest correlation with the difference between the retrieved $X_{\mathrm{CO_2}}$ and the TCCON $X_{\mathrm{CO_2}}$. The retrieved $X_{\mathrm{CO_2}}$ was bias corrected by removing a linear fit between the $X_{\mathrm{CO_2}}$ error and the selected variable. For ACOS B7, the weak CO_2 band signal to noise ratio (SNR) was used. For B8, the one layer model, and the two layer model the difference between the retrieved surface pressure and the prior surface pressure (dp) was selected. For the two-band non-scattering retrieval, the difference between the surface pressure from ABP and the prior surface pressure was used. This is because the two-band non-scattering retrieval does not retrieve surface pressure itself. Differences in surface pressure result in biases in $X_{\mathrm{CO_2}}$ because, despite our best efforts to perfect the retrieval, they modify the path length in unknown ways. Further investigation is needed to determine why the B7 $X_{\mathrm{CO_2}}$ biases are more correlated with the weak CO_2 band SNR than dp.

3.3 Synthetic OCO-2 Observation Results

In this section we examine the results of running various simplified retrievals on our synthetic measurements. Figure 3.3 shows the main results as a function of optical depth and height. This figure has been filtered to remove scenes where large particles (dust, water clouds, and sea salt) were placed at or above 0.5 times the surface pressure. This was done because retrievals on those scenes gave significantly larger errors and it was determined that such scenes are physically unlikely or would have been removed by various filtering techniques. Further investigation is needed to determine why such scenes were not screened out by the ABP or IDP.

The first conclusion is that the standard deviation of the errors is small when the optical depth (τ) of the synthetic scene is very small (τ equals 0.0 or 0.01). This is unsurprising, as very few particles are being perturbed by the scattering layer. However, once the optical depth reaches 0.05 the errors become considerably larger. This is especially true at heights above 0.5, where the light

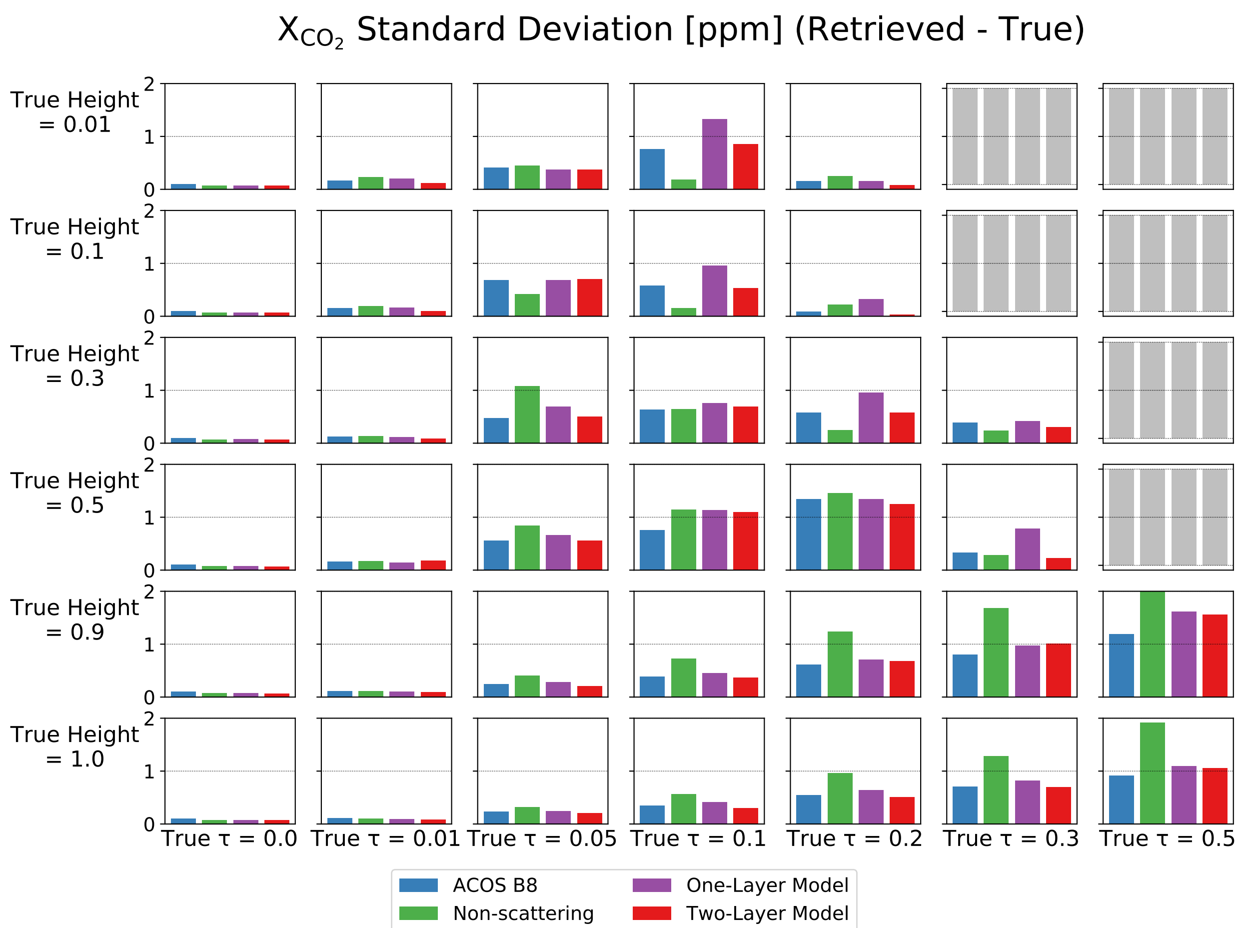

Figure 3.3: Synthetic aerosol matrix showing the standard deviation of the retrieved X_{CO_2} error as a function of the true optical depth (τ) and the true aerosol Gaussian height. ACOS B8 (blue), two-band non-scattering (green), one layer model (purple), and two layer model (red) results are shown by the bars. Grey bars represent tests where no retrievals remained after filtering.

path modification effects of a cloud or aerosol layer become more severe. Interestingly, the errors again become somewhat smaller (less than 0.5 ppm) when the true cloud or aerosol layer is placed in the stratosphere (true height equals 0.01). ACOS B8 and the two layer model are designed with a high-altitude aerosol layer in an attempt to account for these effects, but that does not explain why the errors for the non-scattering and one layer model are also smaller at the highest altitudes. The general trend of errors shows that, as expected, larger optical depths and higher cloud or aerosol layers result in worse $X_{\mathrm{CO_2}}$ errors. Some of the more extreme cases, for example a true optical depth of 0.3 at a true height of 0.1, have smaller error bars because only a few retrievals properly converged.

Several differences can be seen between the four retrievals tested on the synthetic measurement matrix. Generally, the non-scattering retrieval has larger errors for most optical depths and heights. However, a few cases, for example a true optical depth of 0.1 at a height above 0.1, had the non-scattering retrieval perform far better than any of the other retrievals. This requires further investigation, as the non-scattering retrieval has no way to account for the scattering particles and thus should be severely biased in those scenarios.

In general, the one layer model tends to have slightly larger errors than both B8 and the two layer model, which have similar errors for most setups. B8, the one layer model, and the two layer model all have interesting scenarios in which they perform well or poorly. For example, the one layer model does especially poor with a true optical depth of 0.1 at a height of 0.01. Further investigation revealed that this is because the retrieval is unable to move its single layer high enough. Additionally, the one and two layer retrievals do notably worse than B8 when the optical depth is large (τ = 0.5). This may be because B8 includes a low-level water cloud that is able to help fit the radiances better.

Regarding the solar zenith angle used to create the scenes, true SZAs of 25° and 45° have similar errors for all retrieval variants. At 60°, however, all but 7% of the retrievals (for B8) fail to properly converge. This was somewhat expected, as a higher SZA means less signal for the retrieval to work with. Splitting the results by surface albedo produced subtle differences but overall the results seem to be insensitive to the three surface types we selected.

The specific scattering type used in the simulation also impacts the results. For example, all four retrieval variants perform well when the scene contains sulfate particles (Figure 3.4). This is also the case for organic carbon and black carbon. However, the coarse particle types cause problems in the retrievals, especially our test cases, at higher optical depths and higher altitudes. Sea salt, for example, results in a large $X_{\mathrm{CO_2}}$ scatter when it is placed above the middle of the atmosphere. In this case, it should not impact real OCO-2 retrievals because sea salt is mostly confined to near the surface. However, dust and water clouds can often be present at high altitudes and negatively impact the retrievals. Further investigation is needed into why the retrievals perform so poorly when large particles are at high altitudes.

As the two layer model performs about as well as B8 in terms of the standard deviation of the error (Figure 3.3), the other potential benefits can be investigated. Specifically, the speed of the two layer model is expected to be faster because the state vector is smaller, and less nonlinearity in the retrieval should result in fewer iterations needed to find a sufficient minimum in cost function space. Figure 3.5 shows the number of iterations needed to converge for the four retrieval tests as a function of true optical depth and true Gaussian height. As expected, the non-scattering retrieval is unburdened by aerosol radiative transfer calculations and thus is much faster than any of the other tests. However, the one and two layer models also require on average fewer iterations to converge than B8, especially for scenes with low true optical depths. For example, when the true optical depth is 0.01 or 0.0, the one and two layer models take on average almost an entire iteration less to converge (3.8 versus 3.0 iterations). This would result in around a 20% reduction in the amount of processing time needed to retrieve $X_{\mathrm{CO_2}}$. Interestingly, the one layer model requires more iterations than B8 and the two layer model when the true scene contains high-altitude particles with optical depths greater than 0.01. This is likely because the prior retrieved Gaussian aerosol layer height is 0.5 times the surface pressure and the retrieval needs additional iterations to push the scattering layer high enough in the atmosphere.

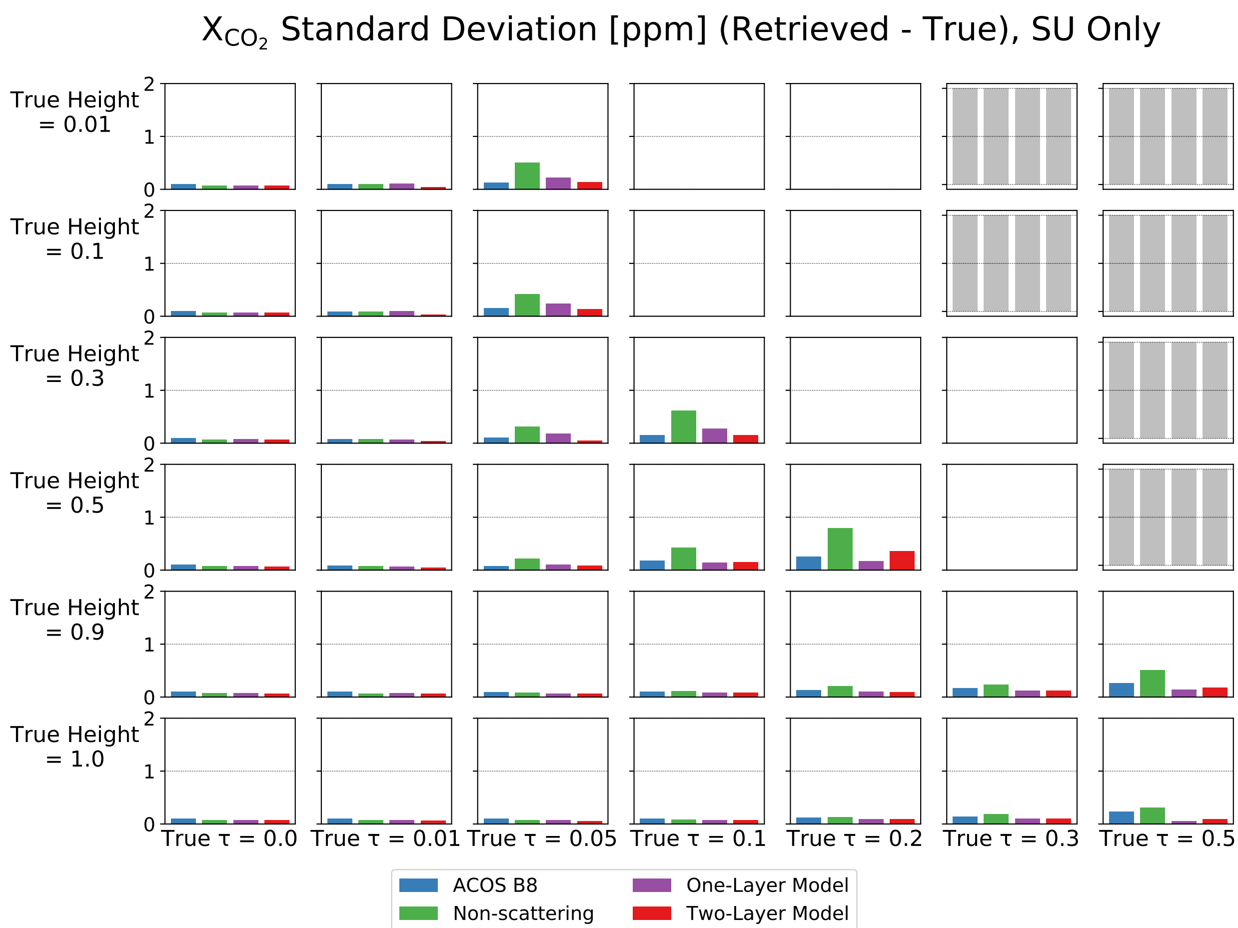

Figure 3.4: Synthetic aerosol matrix showing the standard deviation of the retrieved X_{CO_2} error as a function of the true optical depth (τ) and the true aerosol Gaussian height for scenes created using the MERRA-2 sulfate aerosol type. ACOS B8 (blue), two-band non-scattering (green), one layer model (purple), and two layer model (red) results are shown by the bars. Grey bars and empty white panels represent tests where no retrievals remained after filtering.

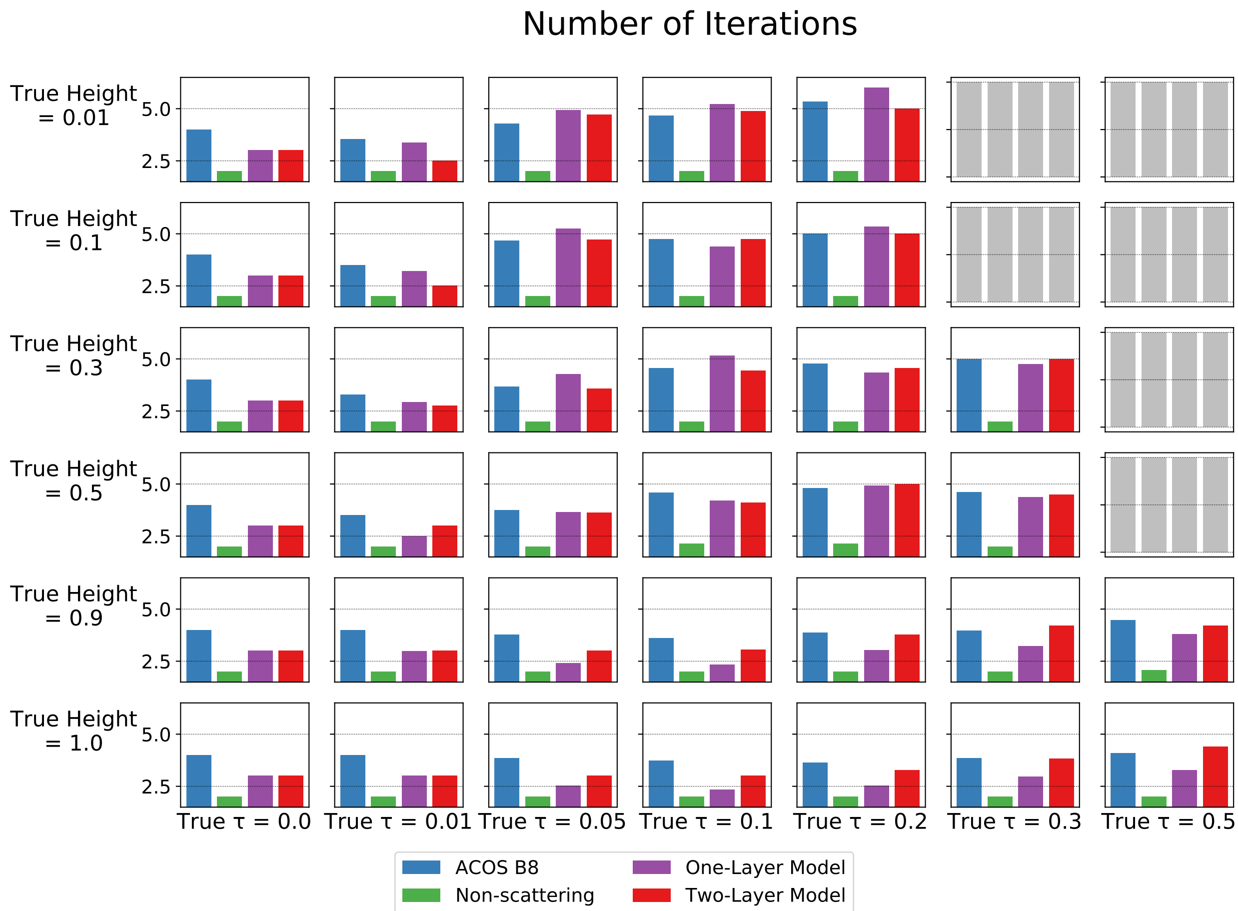

Figure 3.5: Synthetic aerosol matrix showing the number of iterations needed to converge on an X_{CO_2} solution as a function of the true optical depth (τ) and the true aerosol Gaussian height. ACOS B8 (blue), two-band non-scattering (green), one layer model (purple), and two layer model (red) results are shown by the bars. Grey bars represent tests where no retrievals remained after filtering.

3.4 OCO-2 Observation Results

Having examined how the different retrieval variants perform on the synthetic observations, we now move on to real OCO-2 measurements. Figure 3.6 shows the five retrieval types (now including B7) tested on the TCCON validation dataset. ACOS B7 has the lowest correlation coefficient (R), largest standard deviation of the error (σ), and largest mean absolute error (MAE) of any of the tests. Here we can see that ACOS B8 represents a substantial improvement over B7. The addition of the stratospheric aerosol to the state vector, as detailed in [60], results in overall better error statistics against TCCON compared to B7. Most of the high outliers seen in B7 fall much closer to the one-to-one line in the B8 plot.

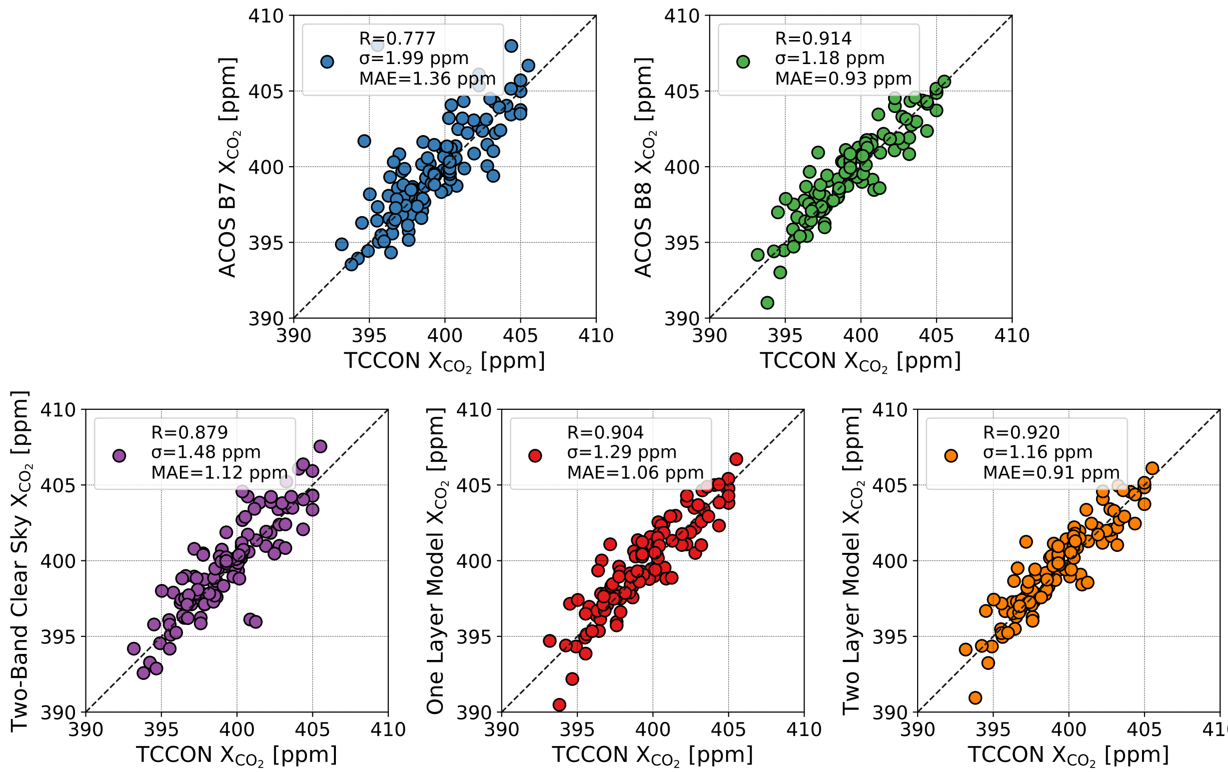

Figure 3.6: TCCON X_{CO_2} compared to retrieved X_{CO_2} values from OCO-2. The top left panel is ACOS B7 (blue), the top right panel is ACOS B8 (green), the bottom left panel is the non-scattering retrieval (purple), the bottom center panel is the one layer model (red), and the bottom right panel is the two layer model (orange). Overpass means are plotted, along with a one-to-one line in black. The correlation coefficient (R), standard deviation of the error (σ), and mean absolute error (MAE) are given for each panel.

3.4.1 Non-Scattering Retrieval

Our hypothesis is that a non-scattering retrieval is not subject to the biases caused by an ineffective aerosol scheme and that, with sufficient filtering, it may perform as well as the operational retrieval. In this test, we have assumed that the prior surface pressure, taken from a model, is sufficient to give us an accurate path length. Additionally, we have disabled the O_2 A-band and are thus assuming that any clouds or aerosols present in the scene do not impact the CO_2 bands substantially.

Figure 3.6 demonstrates that the two-band non-scattering retrieval works moderately well, in agreement with [67]. It has better error statistics than B7, but performs worse than the other three tests. However, the throughput on these non-scattering retrievals is higher than any of the other tests. Of the 32,176 OCO-2 measurements in the validation dataset, which had already been screened to remove most contaminated scenes, only one retrieval failed to converge. B8, the one layer model, and the two layer model all had a few hundred retrievals fail to converge.

3.4.2 One Layer Model

The one layer model was designed to test the hypothesis that including one fine and one coarse mode aerosol types and letting the retrieval mix them and retrieve appropriate AODs along with the layer height should be sufficient to account for any scattering effects in the column. Figure 3.6 suggests that the one layer aerosol parameterization is insufficient in terms of performance when compared to ACOS B8 and the two layer model against TCCON.

The lack of an upper atmospheric layer causes the algorithm to try and move the single layer up to around 0.2 to -0.5 times the surface pressure from a prior position of 0.5 times the surface pressure (note that because we are solving for a Gaussian, the retrieval is allowed to move the retrieved height to less than 0.0 if it thinks only the bottom tail of the Gaussian should be included in the column). This is effectively the top of the atmosphere, which is a clear sign that the retrieval thinks it can fit the radiances better with a high altitude layer compared to a near-surface layer. However, because of this the retrieval lacks a mechanism for accounting for scattering near the surface and thus the retrieved $X_{\mathrm{CO_2}}$ suffers. To further investigate these results, an additional test was done where only a single upper layer was included in the retrieval. This layer consisted of sulfate and an ice type starting in the stratosphere (0.03 times the surface pressure), as in ACOS B8. The hypothesis is that maybe we only need scattering particles in the stratosphere to account for most of the path length modification. The results (not shown) were that a single upper layer model does about as well as the two layer model in terms of R and the scatter of the $X_{\mathrm{CO_2}}$ error, although the initial bias is worse. This indicates that perhaps the retrieval needs a scattering particle in the lower atmosphere, but further investigation is warranted.

3.4.3 Two Layer Model

As shown in Figure 3.6, the two layer model slightly out-performs ACOS B8. It has a lower standard deviation of the $X_{\mathrm{CO_2}}$ error (1.16 ppm vs. 1.18 ppm) and a better correlation coefficient (0.823 vs. 0.818). The hypothesis tested here is that the retrieval needs scattering particles in both the lower and upper atmosphere in order to properly fit the radiances, but that B8 is overly complex. Despite having small optical depths, we need to solve for scattering properties at a high altitude (the stratospheric aerosol and ice cloud layer) because they have a larger impact on the path length modification.

To determine if dust and sulfate were the optimal choices for the lower layer aerosol types, the sensitivity of the retrieval to the selected type was briefly tested. We ran an additional set of retrievals where we used sea salt instead of dust as the coarse particle type in the lower layer. The results (not shown) indicate that the retrieval performs approximately as well as the original two layer model in terms of both scatter and correlation versus TCCON. This suggests that the exact scattering properties of our chosen cloud and aerosol types may matter less than other factors. An additional test to determine if we could simplify the retrieval futher was also performed. We fixed the upper layer at its prior height instead of allowing it to move. This resulted in a slight worsening of error statistics, suggesting that it is important to allow the heights to be solved for in the retrieval in order for the radiance residuals to be optimally minimized.

As shown in Section 3.3, the simplified retrievals performed on synthetic radiances showed a small reduction in the number of iterations needed to converge on an X_{CO_2} solution. Interestingly, the computational benefit on real retrievals is less prominent. The mean number of iterations taken in the two layer model is approximately 3.9, compared to 4.1 for ACOS B8. The one layer model actually takes more iterations, at 4.5 per retrieval. This is likely because the layer starts in the middle of the atmospheric column and frequently needs additional iterations to move to the top of the atmosphere, as discussed in Section 3.4.2. The two-band non-scattering retrieval, as in the synthetic study, took the smallest average number of iterations, at 2.7.

In addition to the TCCON validation dataset, a test was run on the model validation dataset described in Section 2.2.2 to look for regional differences between the two layer model and B8. Figure 3.7 shows the results. While there are grid cells where the two layer model does better and worse than B8, there are no obvious regional patterns in the X_{CO_2} error. The primary feature is that Northern Africa and Central Asia seem to be most sensitive to modifications to the aerosol parameterization, which is in agreement with the results of Chapter 2.

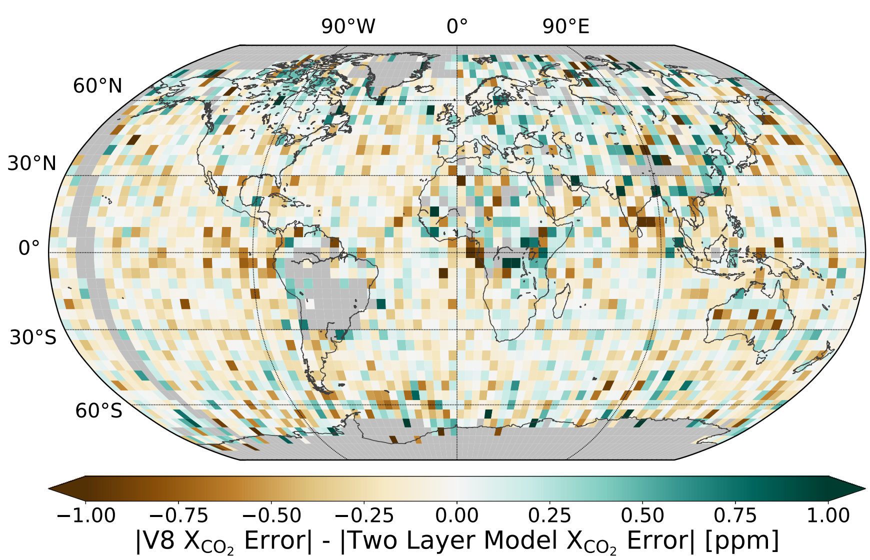

Figure 3.7: 4°x4° binned absolute value of the two layer model X_{CO_2} error against the model validation minus the absolute value of the ACOS B8 X_{CO_2} error against the model validation. Green grid cells represent an improvement relative to the model validation while brown grid cells represent a worse comparison to the model validation. Grey bins represent no data.

3.5 Retrieving Aerosol Properties

As discussed in Section 3.1, the near infrared measurements made by OCO-2 are sensitive to specific properties of a given scattering layer. The total amount of aerosol, height above the ground of the particles, and size distribution of the particles all can significantly impact the measured radiances. Because of this, some research groups retrieve specific aerosol properties such as the single-scattering albedo and effective radius (see Section 1.6). In this section, we test a modified version of ACOS that retrieves the optical depth, height, and effective radius of a single aerosol layer. The hypothesis is that by allowing ACOS to retrieve information about the scattering particle's size instead of fixing it, the retrieval will have more freedom to fit the radiances and retrieve an accurate $X_{\mathrm{CO_2}}$.

We tested this methodology on a single synthetic orbit created by the Colorado State University (CSU) Orbit Simulator [114]. For simplicity, we set the prior height to 0.5 times the surface pressure, the width of the layer to 0.1 times the surface pressure, and the prior optical depth to 0.1 and gave the retrieval sufficient freedom to solve for the height and optical depth. The prior effective radius was set to 4.0 μm with a 1-sigma uncertainty of 2.0 μm. The Cloud-Aerosol Lidar and Infrared Pathfinder Satellite Observations (CALIPSO; [115]) dust type was selected to represent the layer. This selection was somewhat arbitrary, but may have an impact on the results as the different aerosol types all have unique properties independent of the effective radius, such as the refractive index.

Figure 3.8 shows the results after applying a one-parameter bias correction. The most correlated parameter for all four retrieval variants was the H_2O ratio from the IDP. It is unclear why this parameter was chosen instead of dp, which is usually selected. It may be an issue with the exact setup of the synthetic retrievals, but further investigation would be required. Here we can see that the two layer model and ACOS B8 are nearly identical, in agreement with the previous results. The one layer model appears to have slightly more scatter against the true $X_{\mathrm{CO_2}}$, again in agreement with the previous work. The effective radius retrieval, however, shows a much larger scatter in $X_{\mathrm{CO_2}}$ as well as large, latitude-dependent biases. Further work is needed to investigate the source of these issues. Potential causes include the selection of dust as the aerosol type and the fidelity at which the scattering properties were computed. It is likely that running a two layer model where the optical depth, height, and effective radius are solved for in a lower and upper layer could result in reduced X_{CO_2} errors. Previous results have shown the importance of having a scattering type in the upper atmosphere, so this parameterization would adhere to those conclusions.

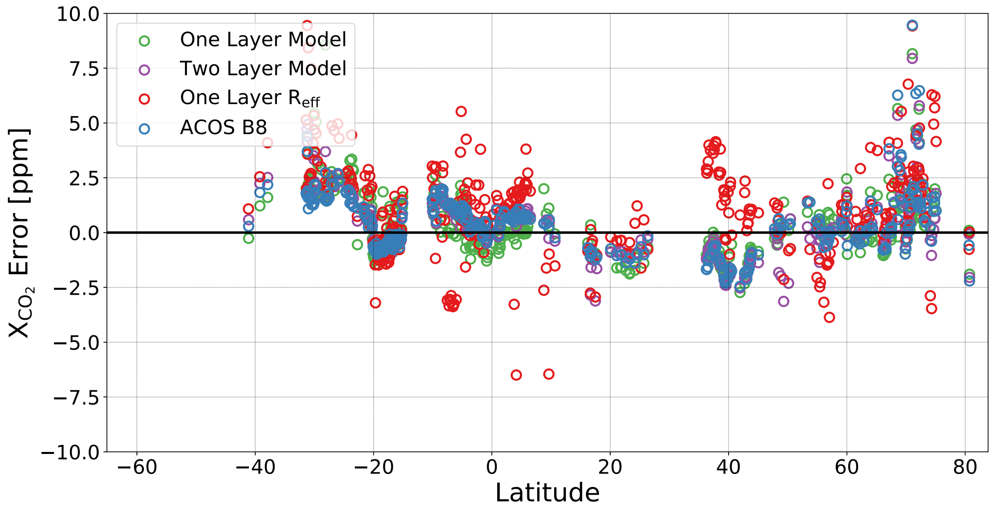

Figure 3.8: X_{CO_2} error of the four retrieval types for one synthetic OCO-2 orbit as a function of latitude: ACOS B8 (blue), the one layer model (green), the two layer model (purple), and the one layer effective radius (red).

3.6 Conclusions

In this work, we have tested multiple simplified aerosol parameterizations on both real and synthetic near-infrared measurements from the Orbiting Carbon Observatory-2. A non-scattering (or “clear sky") retrieval, one layer model, two layer model, and one layer effective radius retrieval were all investigated in terms of throughput and error against validation.

From our synthetic retrieval study (Section 3.3), it was found that the non-scattering retrieval has better throughput than the other retrieval variants. Of the 2,646 measurements in our synthetic aerosol matrix, several hundred failed to converge for all retrieval variants. These were the synthetic measurements in the upper right of Figure 3.3, with large optical depths and high altitudes. However, 1,436 of the total measurements (54%) converged using the non-scattering retrieval, compared to 47-48% for ACOS B8, the one layer model, and the two layer model.

The two layer model was often able to perform about as well as ACOS B8 in terms of the scatter of the X_{CO_2} error, although there are exceptions. For the entire synthetic matrix, ACOS B8 has a standard deviation of the error of 0.60 ppm, compared to the non-scattering retrieval (1.22 ppm), one layer model (0.73 ppm), and two layer model (0.67 ppm). However, these results vary if the true optical depths or heights are subset. For example, if we only look at true optical depths less than 0.1, ACOS B8 has a scatter of 0.30 ppm while the two layer model has a scatter of 0.32 ppm. The retrieval errors were also a function of the synthetic aerosol type, with the fine mode aerosols resulting in smaller errors relative to the coarse mode aerosols (Figure 3.4). This suggests that future work should be focused on screening and parameterizing coarse aerosol types.

One of the expected benefits of a simplified aerosol scheme is enhanced computational performance due to a simplified state vector. Figure 3.5 demonstrates a small improvement in the overall number of iterations needed to converge using the one and two layer models, relative to ACOS B8. This improvement is more pronounced at low true optical depths; when the true optical depth is less than 0.05 the one and two layer models take 20% fewer iterations than ACOS B8.

Investigating retrievals performed on real OCO-2 measurements led to similar conclusions to that of the synthetic study. In terms of convergence, the dataset was already pre-screened to remove most contaminated observations. However, only one non-scattering retrieval failed to converge for our TCCON validation set (Section 3.4), compared to a few hundred for ACOS B8 and the one and two layer models. Specifically, 473 retrievals fail for ACOS B8 and 331 fail for the two layer model.

In terms of correlation, scatter of the X_{CO_2} error, and MAE against TCCON, the two layer model performs slightly better than ACOS B8 (Figure 3.6). The correlation coefficient improves from 0.914 to 0.920, the standard deviation of the error is reduced from 1.18 ppm to 1.16 ppm, and the MAE is improved from 0.93 ppm to 0.91 ppm. The one layer model performs marginally worse against TCCON compared to ACOS B8 and the two layer model. This is likely because the single layer is sent to the upper atmosphere and the retrieval thus has no way to account for any tropospheric scattering particles. The two-band non-scattering retrieval also performs marginally worse, due to its inability to account for any scattering effects. As with the throughput statistics, this work would benefit from an analysis on an unfiltered validation dataset to determine if some retrievals that failed with ACOS B8 could be salvaged using the simplified aerosol parameterizations.

Overall, the two layer model performs about as well as ACOS B8. The expected benefits, including a reduction in iterations and throughput improvements, appear to be limited. Further studies include making improvements to the effective radius retrieval. Designing and testing a two layer model with the effective radius being retrieved for both the lower tropospheric and stratospheric layer could prove more promising, as the retrieval would be solving for the most important aerosol characteristics while also including the important high altitude scattering layer.

Chapter 4

Conclusions and Discussion

4.1 Summary of Results

In this work we have developed and tested numerous aerosol parameterizations with the goal of enhancing the precision and accuracy of near-infrared measurements of total column CO_2 made by the Orbiting Carbon Observatory-2. Because the current ACOS X_{CO_2} retrieval algorithm is relatively mature, large performance gains were not expected. However, this work shows promise and it will hopefully be of use to future ACOS updates as well as other retrieval algorithms maintained by several research groups across the globe for not only OCO-2 measurements but also the several planned future greenhouse gas measurement missions.

Chapter 2 investigated the potential for improved aerosol priors and how it impacts the retrieved X_{CO_2} from real near-infrared measurements from OCO-2. Aerosol information was ingested from co-located GEOS-5 model data with varying levels of uncertainty and compared to both TCCON and a global CO_2 model validation suite. It was found that ingesting instantaneous GEOS-5 aerosol types and AODs with low uncertainty slightly reduced the standard deviation of the X_{CO_2} error against TCCON from 1.17 ppm to 1.13 ppm. Attempting to ingest vertical information from the models produced poor results against TCCON, likely because accurate vertical placement of aerosol layers still represents a significant challenge in global aerosol models. Additionally, fixing the prior aerosol information also yielded poor X_{CO_2} values. This is because modeled aerosols are imperfect and thus the X_{CO_2} retrieval needs some amount of freedom to adjust the aerosol parameters in order to match the observed radiances. When comparing to the global CO_2 model validation dataset, we found that the GEOS-5 setup performs better than ACOS B8 over Northern Africa and Central Asia, due to a combination of smaller prior aerosol optical depths and a lower prior aerosol optical depth uncertainty. The lower prior uncertainty, specifically, prevents the algorithm from retrieving very large AODs and helps prevent the X_{CO_2} from being biased high. Over Northern

Africa and Central Asia, use of the MERRA-2 climatology in B8 results in too large of an AOD prior. This issue is correlated with a small $X_{\mathrm{CO_2}}$ high bias over Central Asia. Finally, our work reiterated the importance of the stratospheric aerosol component introduced in ACOS B8, especially over the Southern Ocean. Overall, the use of better informed aerosol priors shows promise but is restricted by the accuracy and limitations of global aerosol models. This work, specifically the implementation of aerosol type and AOD priors from GEOS-5, has contributed to the development of the ACOS retrieval algorithm for both OCO-2 and OCO-3, due to be launched in March of 2019 and installed on the International Space Station shortly thereafter.

Chapter 3 presented our study on simplifying the ACOS $X_{\mathrm{CO_2}}$ retrieval aerosol parameterization with the hopes of improved throughput, better error statistics, and increased computational speed. We examined retrievals run on both synthetic and real near-infrared measurements. The synthetic retrievals revealed that the two layer model, where only six aerosol parameters were included in the state vector instead of nine, performed slightly worse than ACOS B8, with a standard deviation of the $X_{\mathrm{CO_2}}$ error of 0.67 ppm compared to 0.60 ppm. These results varied depending on the exact true optical depth and true aerosol layer height of the scene. The retrieval errors were also a function of the specific aerosol type, with the fine mode aerosols resulting in smaller $X_{\mathrm{CO_2}}$ errors relative to coarse mode aerosols. Regarding computational speed, there was a small improvement in the number of iterations needed to converge using the two layer model on the synthetic radiances. Examining the simplified retrievals run on real OCO-2 measurements and validated against TCCON showed that the two layer model performs slightly better than ACOS B8, with a reduction in the standard deviation of the $X_{\mathrm{CO_2}}$ error from 1.18 ppm to 1.16 ppm. The two-band non-scattering retrieval and one layer model perform marginally worse, implying that neither parameterization is complex enough to sufficiently capture the impact of scattering particles on the measured radiances. Overall, the two layer model performs about as well as ACOS B8 in terms of error against the validation sources, throughput, and computational speed. Additional studies include testing on an unfiltered validation dataset and working to improve the effective radius retrieval.

4.2 The Future of Space-Based Measurements of CO_2

The world is beginning to understand the direness of climate change and many nations and organizations are investing millions of dollars into new instruments and missions designed to measure greenhouse gases from space. Some of these include OCO-3, GOSAT-2, GOSAT-3, MicroCarb, TanSat-2, TROPOMI [116], and GeoCarb. The funding of these missions is predicated upon the assumption that retrieval errors will continue to improve and that the defined accuracy and precision requirements will be met. However, atmospheric scattering effects remain an unsolved problem in the near-infrared retrieval community and thus many of these research groups will need to continue to investigate how to best handle this issue in order to minimize their measurement errors. This is especially true for current and future GHG missions that have large-scale mapping capabilities because aerosol plume biases may masquerade as real GHG signals. Studying GHG emissions over megacities and power plants will also be hindered because of co-located anthropogenic aerosols and cloudy regions, such as tropical rainforests, may also contain significant biases.

One strategy to try and solve this problem is to include additional instruments on the same platform as a GHG sensor. GOSAT and GOSAT-2, for example, also have cloud and aerosol imagers onboard, but so far these have primarily been used for screening. The ESA's Sentinel-7, currently in development, will contain a multi-angle polarimeter designed to reduce aerosol induced X_{CO_2} errors. Sentinel-7 will also contain an NO_2 detector to retrieve the plume shape of CO_2 point sources in order to estimate their emission rate. Finally, discussions of future mission concepts typically include a near-infrared sensor combined with a cloud and aerosol lidar. This would allow for new methods of screening and the ability to ingest accurate vertical cloud and aerosol information into the GHG retrievals, but such a mission would be relatively expensive. The vertical cloud profiles would be especially useful, as little work has been done on trying to use observations or models to try to improve the cloud priors, due to the small-scale nature of clouds. Some preliminary work has investigated combining measurements from CALIPSO and OCO-2, both in the NASA Afternoon-Train, but sensitivity and co-location issues proved difficult to overcome. Studies are also being performed on the 3-dimensional effects of cloud and aerosol layers on the $X_{\mathrm{CO_2}}$ retrievals [117] and on averaging multiple OCO-2 measurements together, both with the goal of reducing small-scale biases.

Regarding the results of this work, further studies are needed to determine the optimal cloud and aerosol parameterization for retrievals of $X_{\mathrm{CO_2}}$ performed on near-infrared measurements. Future work on improving the aerosol priors and their associated uncertainties should be combined with any updates to the parameterization, but significant enhancements to the precision and accuracy of the $X_{\mathrm{CO_2}}$ retrievals are unlikely, in part because the current ACOS retrieval is relatively mature.

Bibliography

[1] Svante Arrhenius. Xxxi. on the influence of carbonic acid in the air upon the temperature of the ground. *The London, Edinburgh, and Dublin Philosophical Magazine and Journal of Science*, 41(251):237–276, 1896.

[2] IPCC. *Climate Change 2013: The Physical Science Basis. Contribution of Working Group I to the Fifth Assessment Report of the Intergovernmental Panel on Climate Change*. Cambridge University Press, Cambridge, United Kingdom and New York, NY, USA, 2013.

[3] Corinne Le Quéré, R. M. Andrew, P. Friedlingstein, S. Sitch, J. Hauck, J. Pongratz, P. A. Pickers, J. I. Korsbakken, G. P. Peters, J. G. Canadell, A. Arneth, V. K. Arora, L. Barbero, A. Bastos, L. Bopp, F. Chevallier, L. P. Chini, P. Ciais, S. C. Doney, T. Gkritzalis, D. S. Goll, I. Harris, V. Haverd, F. M. Hoffman, M. Hoppema, R. A. Houghton, G. Hurtt, T. Ilyina, A. K. Jain, T. Johannessen, C. D. Jones, E. Kato, R. F. Keeling, K. K. Goldewijk, P. LandschÃijtzer, N. Lefévre, S. Lienert, Z. Liu, D. Lombardozzi, N. Metzl, D. R. Munro, J. E. M. S. Nabel, S.-I. Nakaoka, C. Neill, A. Olsen, T. Ono, P. Patra, A. Peregon, W. Peters, P. Peylin, B. Pfeil, D. Pierrot, B. Poulter, G. Rehder, L. Resplandy, E. Robertson, M. Rocher, C. RÃűdenbeck, U. Schuster, J. Schwinger, R. Séférian, I. Skjelvan, T. Steinhoff, A. Sutton, P. P. Tans, H. Tian, B. Tilbrook, F. N. Tubiello, I. T. van der Laan-Luijkx, G. R. van der Werf, N. Viovy, A. P. Walker, A. J. Wiltshire, R. Wright, S. Zaehle, and B. Zheng. Global carbon budget 2018. *Earth Syst. Sci. Data*, 10:2141–2194, 2018.

[4] C. Beer, M. Reichstein, E. Tomelleri, P. Ciais, M. Jung, N. Carvalhais, C. Rodenbeck, M. A. Arain, D. Baldocchi, G. B. Bonan, A. Bondeau, A. Cescatti, G. Lasslop, A. Lindroth, M. Lomas, S. Luyssaert, H. Margolis, K. W. Oleson, O. Roupsard, E. Veenendaal, N. Viovy, C. Williams, F. I. Woodward, and D. Papale. Terrestrial gross carbon dioxide uptake: global distribution and covariation with climate. *Science*, page 1184984, 2010.

[5] P. Ciais, C. Sabine, G. Bala, L. Bopp, V. Brovkin, J. Canadell, A. Chhabra, R. DeFries, J. Galloway, M. Heimann, C. Jones, C. Le Quéré, R.B. Myneni, S. Piao, and P. Thornton. *Carbon and Other Biogeochemical Cycles*. Cambridge University Press, Cambridge, United Kingdom and New York, NY, USA, 2013.

[6] Corinne Le Quéré, Robbie M. Andrew, Pierre Friedlingstein, Stephen Sitch, Julia Pongratz, Andrew C. Manning, Jan Ivar Korsbakken, Glen P. Peters, Josep G. Canadell, Robert B. Jackson, Thomas A. Boden, Pieter P. Tans, Oliver D. Andrews, Vivek K. Arora, Dorothee C. E. Bakker, Leticia Barbero, Meike Becker, Richard A. Betts, Laurent Bopp, Frédéric Chevallier, Philippe Chini, Louise P. an Ciais, Catherine E. Cosca, Jessica Cross, Kim Currie, Thomas Gasser, Ian Harris, Judith Hauck, Vanessa Haverd, Richard A. Houghton, Christopher W. Hunt, George Hurtt, Tatiana Ilyina, Atul K. Jain, Etsushi Kato, Markus Kautz, Ralph F. Keeling, Kees Klein Goldewijk, Arne Körtzinger, Peter Landschützer, Nathalie Lefèvre, Andrew Lenton, Sebastian Lienert, Ivan Lima, Danica Lombardozzi, Nicolas Metzl, Frank Millero, Pedro M. S. Monteiro, David R. Munro, Julia E. M. S. Nabel, Shin-ichiro Nakaoka, Yukihiro Nojiri, X. Antoni Padín, Anna Peregon, Benjamin Pfeil, Denis Pierrot, Benjamin Poulter, Gregor Rehder, Janet Reimer, Christian Rödenbeck, Jörg Schwinger, Roland Séférian, Ingunn Skjelvan, Benjamin D. Stocker, Hanqin Tian, Bronte Tilbrook, Ingrid T. van der Laan-Luijkx, Guido R. van der Werf, Steven van Heuven, Nicolas Viovy, Nicolas Vuichard, Anthony P. Walker, Andrew J. Watson, Andrew J. Wiltshire, Sönke Zaehle, and Dan Zhu. Global carbon budget 2017. *Earth Syst. Sci. Data*, 10:405–448, 2018.

[7] Corinne Le Quéré, M. R. Raupach, J. G. Canadell, G. Marland, Laurent Bopp, Philippe Ciais, Thomas J. Conway, Scott C. Doney, Richard A. Feely, Pru Foster, Pierre Friedlingstein, Kevin Gurney, Richard A. Houghton, Joanna I. House, Chris Huntingford, Peter E. Levy, Mark R. Lomas, Joseph Majkut, Nicolas Metzl, Jean P. Ometto, Glen P. Peters, I. Colin Prentice, James T. Randerson, Steven W. Running, Jorge L. Sarmiento, Ute Schuster, Stephen Sitch, Taro Takahashi, Nicolas Viovy, Guido R. van der Werf, and F. Ian Wood-

ward. Trends in the sources and sinks of carbon dioxide. *Nature Geoscience*, 2:831–836, 2009.

[8] P. J. Rayner and D. M. O'Brien. The utility of remotely sensed co_2 concentration data in surface source inversions. *Geophysical Research Letters*, 28:175–178, 2001.

[9] D. F. Baker, H. Bösch, S. C. Doney, D. O'Brien, and D. S. Schimel. Carbon source/sink information provided by column co_2 measurements from the orbiting carbon observatory. *Atmospheric Chemistry and Physics*, 10:4145–4165, 2010.

[10] F. Chevallier, F.-M. Bréon, and P. J. Rayner. Contribution of the orbiting carbon observatory to the estimation of co_2 sources and sinks: Theoretical study in a variational data assimilation framework. *Journal of Geophysical Research*, 112:D09307, 2007.

[11] F. Chevallier, S. Maksyutov, P. Bousquet, F.-M. Bréon, R. Saito, Y. Toshida, and T. Yokota. On the accuracy of the co_2 surface fluxes to be estimated from the gosat observations. *Geophysical Research Letters*, 36:L19807, 2009.

[12] T. Yokota, Y. Yoshida, N. Eguchi, Y. Ota, T. Tanaka, H. Watanabe, and S. Maksyutov. Global concentrations of co_2 and ch_4 retrieved from gosat: First preliminary results. *Scientific Online Letters on the Atmosphere*, 5:160–163, 2009.

[13] Greet Janssens-Maenhout, Monica Crippa, Diego Guizzardi, Marilena Muntean, Edwin Schaaf, Frank Dentener, Peter Bergamaschi, Valerio Pagliari, J. G. J. Olivier, J. A. H. W. Peters, J. A. van Aardenne, S. Monni, U. Doering, and A. M. R. Petrescu. Edgar v4. 3.2 global atlas of the three major greenhouse gas emissions for the period 1970–2012. *Earth Syst. Sci. Data Discuss*, 2017.

[14] Thomas A Boden, Robert J Andres, and Gregg Marland. Global, regional, and national fossil-fuel co_2 emissions (1751-2010)(v. 2013). Technical report, Carbon Dioxide Information Analysis Center (CDIAC), Oak Ridge National Laboratory (ORNL), Oak Ridge, TN (United States), 2013.

[15] Tomohiro Oda and Shamil Maksyutov. A very high-resolution (1 km$\times$ 1 km) global fossil fuel co_2 emission inventory derived using a point source database and satellite observations of nighttime lights. *Atmospheric Chemistry and Physics*, 11(2):543–556, 2011.

[16] Tomohiro Oda, Shamil Maksyutov, and Robert J Andres. The open-source data inventory for anthropogenic co_2, version 2016 (odiac2016): a global monthly fossil fuel co_2 gridded emissions data product for tracer transport simulations and surface flux inversions. *Earth System Science Data*, 10(1):87–107, 2018.

[17] P. Ciais, A. J. Dolman, A. Bombelli, R. Duren, A. Peregon, P. J. Rayner, C. Miller, N. Gobron, G. Kinderman, G. Marland, N. Gruber, F. Chevallier, R. J. Andres, G. Balsamo, L. Bopp, F.-M. Bréon, G. Broquet, R. Dargaville, T. J. Battin, A. Borges, H. Bovensmann, M. Buchwitz, J. Butler, J. G. Canadell, R. B. Cook, R. DeFries, R. Engelen, K. R. Gurney, C. Heinze, M. Heimann, A. Held, M. Henry, B. Law, S. Luyssaert, J. Miller, T. Moriyama, C. Moulin, R. B. Myneni, C. Nussli, M. Obersteiner, D. Ojima, Y. Pan, J.-D. Paris, S. L. Piao, B. Poulter, S. Plummer, S. Quegan, P. Raymond, M. Reichstein, L. Rivier, C. Sabine, D. Schimel, O. Tarasova, R. Valentini, R. Wang, G. van der Werf, D. Wickland, M. Williams, and C. Zehner. Current systematic carbon-cycle observations and the need for implementing a policy-relevant carbon observing system. *Biogeosciences*, 11:3547–3602, 2014.

[18] WMO. The state of greenhouse gases in the atmosphere based on global observations through 2016. *WMO Greenhouse Gas Bulletin*, 13, 2017.

[19] P. Bergamaschi, A. Danila, R. F. Weiss, P. Ciais, R. L. Thompson, D. Brunner, I. Levin, Y. Meijer, F. Chevallier, G. Janssens-Maenhout, H. Bovensmann, D. Crisp, S. Basu, E. Dlugokencky, R. Engelen, C. Gerbig, D. Günther, S. Hammer, S. Henne, S. Houweling, U. Karstens, E. Kort, M. Maione, A. J. Manning, J. Miller, S. Montzka, S. Pandey, W. Peters, P. Peylin, B. Pinty, M. Ramonet, S. Reimann, T. Röckmann, M. Schmidt, M. Strogies, J. Sussams, O. Tarasova, J. van Aardenne, A. T. Vermeulen, and F. Vogel:. *Atmospheric*

monitoring and inverse modelling for verification of greenhouse gas inventories. Office of the European Union, 2018.

[20] S Houweling, F-M Breon, I Aben, C Rödenbeck, M Gloor, M Heimann, and P Ciais. Inverse modeling of co_2 sources and sinks using satellite data: a synthetic inter-comparison of measurement techniques and their performance as a function of space and time. *Atmospheric Chemistry and Physics*, 4(2):523–538, 2004.

[21] Frédéric Chevallier. Impact of correlated observation errors on inverted co_2 surface fluxes from oco measurements. *Geophysical Research Letters*, 34(24), 2007.

[22] C. E. Miller, D. Crisp, P. L. DeCola, S. C. Olsen, J. T. Randerson, A. M. Michalak, A. Alkhaled, P. Rayner, D. J. Jacob, P. Suntharalingam, D. B. A. Jones, A. S. Denning, M. E. Nicholls, S. C. Doney, S. Pawson, H. Boesch, B. J. Connor, I. Y. Fung, D. O'Brien, R. J. Salawitch, S. P. Sander, B. Sen, P. Tans, G. C. Toon, P. O. Wennberg, S. C. Wofsy, Y. L. Yung, and R. M. Law. Precision requirements for space-based x_{co_2} data. *Journal of Geophysical Research*, 112:D10314, 2007.

[23] L. Feng, P. I. Palmer, H. Bösch, and S. Dance. Estimating surface co_2 fluxes from space-borne co_2 dry air mole fraction observations using an ensemble kalman filter. *Atmospheric Chemistry and Physics*, 9(8):2619–2633, 2009.

[24] P. I. Palmer, L. Feng, and H. Bösch. Spatial resolution of tropical terrestrial co_2 fluxes inferred using space-borne column co_2sampled in different earth orbits: the role of spatial error correlations. *Atmospheric Measurement Techniques*, 4(9):1995–2006, 2011.

[25] S. Basu, S. Guerlet, A. Butz, S. Houweling, O. Hasekamp, I. Aben, P. Krummel, P. Steele, R. Langenfelds, M. Torn, S. Biraud, B. Stephens, A. Andrews, and D. Worthy. Global co_2 fluxes estimated from gosat retrievals of total column co_2. *Atmospheric Chemistry and Physics*, 13:8695–8717, 2013.

[26] O Schneising, J Heymann, M Buchwitz, M Reuter, H Bovensmann, and J. P. Burrows. Anthropogenic carbon dioxide source areas observed from space: assessment of regional enhancements and trends. *Atmospheric Chemistry and Physics*, 13(5):2445–2454, 2013.

[27] M. Reuter, M. Buchwitz, M. Hilker, J. Heymann, O. Schneising, D. Pillai, H. Bovensmann, J. P. Burrows, Hartmut Boesch, Robert Parker, A. Butz, O. Hasekamp, C. W. O'Dell, Y. Yoshida, C. Gerbig, T. Nehrkorn, N. M. Deutscher, T. Warneke, J. Notholt, F. Hase, R. Kivi, R. Sussmann, T. Machida, H. Matsueda, and Y Sawa. Satellite-inferred european carbon sink larger than expected. *Atmospheric Chemistry and Physics*, 14(24):13739–13753, 2014.

[28] Janne Hakkarainen, Iolanda Ialongo, and Johanna Tamminen. Direct space-based observations of anthropogenic co_2 emission areas from oco-2. *Geophysical Research Letters*, 43(21), 2016.

[29] J Heymann, M Reuter, M Buchwitz, O Schneising, H Bovensmann, J. P. Burrows, S Massart, J. W. Kaiser, and D Crisp. Co_2 emission of indonesian fires in 2015 estimated from satellite-derived atmospheric co_2 concentrations. *Geophysical Research Letters*, 44(3):1537–1544, 2017.

[30] A. Chatterjee, M. M. Gierach, A. J. Sutton, R. A. Feely, D. Crisp, A. Eldering, M. R. Gunson, C. W. O'Dell, B. B. Stephens, and D. S. Schimel. Influence of el niño on atmospheric co_2 over the tropical pacific ocean: Findings from nasaâĂŹs oco-2 mission. *Science*, 358(6360):eaam5776, 2017.

[31] Junjie Liu, Kevin W Bowman, David S Schimel, Nicolas C Parazoo, Zhe Jiang, Meemong Lee, A Anthony Bloom, Debra Wunch, Christian Frankenberg, Ying Sun, C. W. O'Dell, K. R. Gurney, D Menemenlis, M Gierach, D Crisp, and A Eldering. Contrasting carbon cycle responses of the tropical continents to the 2015–2016 el niño. *Science*, 358(6360), 2017.

[32] Ray Nassar, Timothy G Hill, Chris A McLinden, Debra Wunch, Dylan Jones, and David Crisp. Quantifying co_2 emissions from individual power plants from space. *Geophysical Research Letters*, 44(19), 2017.

[33] Florian M Schwandner, Michael R Gunson, Charles E Miller, Simon A Carn, Annmarie Eldering, Thomas Krings, Kristal R Verhulst, David S Schimel, Hai M Nguyen, David Crisp, C. Frankenberg, M. Gunson, and H. Pollock. Spaceborne detection of localized carbon dioxide sources. *Science*, 358(6360):eaam5782, 2017.

[34] H Lindqvist, C. W. O'Dell, S Basu, H Boesch, F Chevallier, N Deutscher, L Feng, B Fisher, F Hase, M Inoue, R. Kivi, I. Morino, P. I. Palmer, R. Parker, M. Schneider, R. Sussmann, and Y. Yoshida. Does gosat capture the true seasonal cycle of x_{co_2}? *Atmospheric Chemistry and Physics*, 15(11), 2015.

[35] Christian Frankenberg, Susan S Kulawik, Steven C Wofsy, Frédéric Chevallier, Bruce Daube, Eric A Kort, Christopher O'dell, Edward T Olsen, and Gregory Osterman. Using airborne hiaper pole-to-pole observations (hippo) to evaluate model and remote sensing estimates of atmospheric carbon dioxide. *Atmospheric Chemistry and Physics*, 16(12):7867–7878, 2016.

[36] Debra Wunch, Paul O Wennberg, Gregory Osterman, Brendan Fisher, Bret Naylor, Coleen M Roehl, Christopher O'Dell, Lukas Mandrake, Camille Viatte, Matthäus Kiel, D. G. Feist, S. G. Arnold, K. Strong, J. Mendonca, R. Kivi, P. Heikkinen, L. Iraci, J. Podolske, P. W. Hillyard, S. Kawakami, M. K. Dubey, H. A. Parker, E. Sepulveda, O. E. G. Rodriguez, Y. Te, P. Jeseck, M. R. Gunson, D. Crisp, and A. Eldering. Comparisons of the orbiting carbon observatory-2 (oco-2) x_{co_2} measurements with tccon. *Atmospheric Measurement Techniques*, 10(6):2209–2238, 2017.

[37] A. Chédin, S. Serrar, N. A. Scott, C. Pierangelo, and P. Ciais. Impact of tropical biomass burning emissions on the diurnal cycle of upper tropospheric co_2 retrieved from noaa 10 satellite observations. *Journal of Geophysical Research: Atmospheres*, 110(D11), 2005.

[38] W. L. Smith, H. M. Woolf, C. M. Hayden, D. Q. Wark, and L. M. McMillin. the tiros-n operational vertical sounder. *Bulletin of the American Meteorological Society*, 60:1177–1187, 1979.

[39] R. J. Engelen and G. L. Stephens. Information content of infrared satellite sounding measurements with respect to co_2. *Journal of Applied Meteorology*, 43(2):373–378, 2004.

[40] H. Bovensmann, J. P. Burrows, M. Buchwitz, J. Frerick, S. Noël, V. V. Rozanov, K. V. Chance, and A. P. H. Goede. Sciamachy: Mission objectives and measurement modes. *Journal of the atmospheric sciences*, 56(2):127–150, 1999.

[41] M. Buchwitz, R. de Beek, S. Noël, J. P. Burrows, H. Bovensmann, H. Bremer, P. Bergamaschi, S. Körner, and M. Heimann. Carbon monoxide, methane and carbon dioxide columns retrieved from sciamachy by wfm-doas: year 2003 initial data set. *Atmospheric Chemistry and Physics*, 5(12):3313–3329, 2005.

[42] O Schneising, M Buchwitz, J Burrows, H Bovensmann, Markus Reuter, Justus Notholt, Ronald Macatangay, and Thorsten Warneke. Three years of greenhouse gas column-averaged dry air mole fractions retrieved from satellite - part 1: Carbon dioxide. *Atmospheric Chemistry and Physics*, 8(14):3827–3852, 2008.

[43] T. S. L'Ecuyer and J. H. Jiang. Touring the atmosphere aboard the a-train. *Physics Today*, 63:36–41, 2010.

[44] Dongxu Yang, Yi Liu, Zhaonan Cai, Xi Chen, Lu Yao, and Daren Lu. First global carbon dioxide maps produced from tansat measurements. *Advances in Atmospheric Sciences*, 35(6):621–623, 2018.

[45] Joel Susskind, Christopher D Barnet, and John M Blaisdell. Retrieval of atmospheric and surface parameters from airs/amsu/hsb data in the presence of clouds. *IEEE Transactions on Geoscience and Remote Sensing*, 41(2):390–409, 2003.

[46] N Pougatchev, T August, X Calbet, T Hultberg, O Oduleye, P Schlüssel, B Stiller, K. S. Germain, and G Bingham. Iasi temperature and water vapor retrievals–error assessment and validation. *Atmospheric Chemistry and Physics*, 9(17):6453–6458, 2009.

[47] S. S. Kulawik, D. B. A Jones, R. Nassar, F. W. Irion, J. R. Worden, K. W. Bowman, T. Machida, H. Matsueda, Y. Sawa, S. C. Biraud, M. L. Fischer, and A. R. Jacobson. Characterization of tropospheric emission spectrometer (tes) co_2 for carbon cycle science. *Atmospheric Chemistry and Physics*, 10(12):5601–5623, 2010.

[48] Peter F Bernath, Charles Thomas McElroy, MC Abrams, Christopher D Boone, Mike Butler, Claude Camy-Peyret, Michel Carleer, Cathy Clerbaux, P-F Coheur, Réginald Colin, P. DeCola, M. DeMaziÃÍre, J. R. Drummond, D. Dufour, W. F. J. Evans, H. Fast, D. Fussen, K. Gilbert, D. E. Jennings, E. J. Llewellyn, R. P. Lowe, E. Mahieu, J. C. McConnell, M. McHugh, S. D. McLeod, R. Michaud, C. Midwinter, R. Nassar, F. Nichitiu, C. Nowlan, C. P. Rinsland, Y. J. Rochon, N. Rowlands, K. Semeniuk, P. Simon, R. Skelton, J. J. Sloan, M.âĂŘA. Soucy, K. Strong, P. Tremblay, D. Turnbull, K. A. Walker, I. Walkty, D. A. Wardle, V. Wehrle, R. Zander, and J. Zou. Atmospheric chemistry experiment (ace): mission overview. *Geophysical Research Letters*, 32(15), 2005.

[49] D. Crisp, H. Bösch, L. Brown, R. Castano, M. Christi, B. Connor, C. Frankenberg, J. McDuffie, C. E. Miller, V. Natraj, C. O'Dell, D. O'Brien, I. Polonsky, F. Oyafuso, D. Thompson, G. Toon, and R. Spurr. Oco (orbiting carbon observatory)-2 level 2 full physics retrieval algorithm theoretical basis, tech. rep. oco d-65488. Technical report, NASA Jet Propulsion Laboratory, California Institute of Technology, Pasadena, CA, 2010. version 1.0 Rev 4, https://docserver.gesdisc.eosdis.nasa.gov/public/project/OCO/OCO-2_L2_FP_ATBD_v1_rev4_Nov10.pdf, (last access: October 2018).

[50] C. Cox and W. Munk. Measurement of the roughness of the sea surface from photographs of the sun's glitter. *Journal of the Optical Society of America*, 44(11):838–850, 1954.

[51] D. Wunch, G. C. Toon, J.-F. L. Blavier, R. A. Washenfelder, J. Notholt, B. J. Connor, D. W. T. Griffith, V. Sherlock, and P. O. Wennberg. The total carbon column observing network. *Philosophical Transactions of the Royal Society A*, 369:2087–2112, 2011.

[52] A. Eldering, T. E. Taylor, C. W. OD́ell, and R. Pavlick. The oco-3 mission; measurement objectives and expected performance based on one year of simulated data. *Atmos. Meas. Tech. Discuss.*, 2018.

[53] I. N. Polonsky, D. M. O'Brien, J. B. Kumer, and C. W. O'Dell. Performance of a geostationary mission, geocarb, to measure co_2, ch_4 and co column-averaged concentrations. *Atmospheric Measurement Techniques*, 7(4):959–981, 2014.

[54] Berrien Moore, Sean Crowell, Peter Rayner, Jack Kumer, Christopher O'Dell, Denis O'Brien, Steven Utembe, Igor Polonsky, David Schimel, and James Lemen. The potential of the geostationary carbon cycle observatory (geocarb) to provide multi-scale constraints on the carbon cycle in the americas. *Frontiers in Environmental Science*, 6:109, 2018.

[55] D. Crisp, C. E. Miller, and P. L. DeCola. Nasa orbiting carbon observatory: measuring the column averaged carbon dioxide mole fraction from space. *Journal of Applied Remote Sensing*, 2, 2008.

[56] C. W. O'Dell, B. Conner, H. Bösch, D. O'Brien, C. Frankenberg, R. Castano, M. Christi, D. Eldering, B. Fisher, M. Gunson, J. McDuffie, C. E. Miller, V. Natraj, F. Oyafuso, I. Polonsky, M. Smyth, T. Taylor, G. C. Toon, P. O. Wennberg, and D. Wunch. The acos co_2 retrieval algorithm - part 1: Description and validation against synthetic observations. *Atmospheric Measurement Techniques*, 5:99–121, 2012.

[57] C. D. Rodgers. *Inverse Methods for Atmospheric Sounding: Theory and Practice*. World Scientific, Singapore, 2000.

[58] R. J. D. Spurr, T. P. Kurosu, and K. V. Chance. A linearized discrete ordinate radiative transfer model for atmospheric remote-sensing retrieval. *Journal of Quantitative Spectroscopy and Radiative Transfer*, 68(6):689–735, 2001.

[59] R. J. D. Spurr. Simultaneous derivation of intensities and weighting functions in a general pseudo-spherical discrete ordinate radiative transfer treatment. *Journal of Quantitative Spectroscopy and Radiative Transfer*, 75(2):129–175, 2002.

[60] C. W. O'Dell, A. Eldering, P. O. Wennberg, D. Crisp, M. R. Gunson, B. Fischer, C. Frankenberg, M. Kiel, H. Lindqvist, L. Mandrake, A. Merrelli, V. Natraj, R. R. Nelson, G. B. Osterman, V. H. Payne, T. E. Taylor, D. Wunch, B. J. Drouin, F. Oyafuso, A. Chang, J. McDuffie, M. Smyth, D. F. Baker, S. Basu, F. Chevallier, S. M. R. Crowell, L. Feng, P. I. Palmer, M. Dubey, O. E. García, D. W. T. Griffith, F. Hase, L. T. Iraci, R. Kivi, I. Morino, J. Notholt, H. Ohyama, C. Petri, C. M. Roehl, M. K. Sha, K. Strong, R. Sussmann, Y. Te, O. Uchino, and V. A. Velazcu. Improved retrievals of carbon dioxide from the orbiting carbon observatory-2 with the version 8 acos algorithm. *Atmospheric Measurement Techniques*, 11:6539–6576, 2018.

[61] C. Frankenberg, C. O'Dell, J. Berry, L. Guanter, J. Joiner, P. Köhler, R. Pollock, and T. E. Taylor. Prospects for chlorophyll fluorescence remote sensing from the orbiting carbon observatory-2. *Remote Sensing of Enviornment*, 147:1–12, 2013.

[62] M. M. Rienecker, Max J. Suarez, R. Todling, J. Bacmeister, L. Takacs, H.-C. Liu, W. Gu, M. Sienkiewicz, R. D. Koster, R. Gelaro, I. Stajner, and J. E. Nielsen. The geos-5 data assimilation system-documentation of versions 5.0.1, 5.1.0, and 5.2.0. Technical report, NASA Goddard Space Flight Center, Greenbelt, MD, 2008. https://ntrs.nasa.gov/archive/nasa/casi.ntrs.nasa.gov/20120011955.pdf.

[63] B. J. Connor, H. Boesch, G. Toon, B. Sen, C. Miller, and D. Crisp. Orbiting carbon observatory: Inverse method and prospective error analysis. *Journal of Geophysical Research*, 113:D05305, 2008.

[64] D. M. O'Brien and P. J. Rayner. Global observations of the carbon budget 2. co_2 column from differential absorption of reflected sunlight in the 1.61 μm band of co_2. *Journal of Geophysical Research*, 107(D18):ACH–6, 2002.

[65] I. Aben, O. Hasekamp, and W. Hartmann. Uncertainties in the space-based measurements of co_2 columns due to scattering in the earth's atmosphere. *Journal of Quantiterative Spectroscopy & Radiative Transfer*, 104:450–459, 2007.

[66] A. Butz, O. P. Hasekamp, C. Frankenberg, and I. Aben. Retrievals of atmospheric co_2 from simulated space-borne measurements of backscattered near-infrared sunlight: accounting for aerosol effects. *Applied Optics*, 48:3322–3336, 2009.

[67] Robert R Nelson, Christopher W O'Dell, Thomas E Taylor, Lukas Mandrake, and Mike Smyth. The potential of clear-sky carbon dioxide satellite retrievals. *Atmospheric Measurement Techniques*, 9(4):1671–1684, 2016.

[68] S. Oshchepkov, A. Bril, T. Yokota, P. O. Wennberg, N. M. Deutscher, D. Wunch, G. C. Toon, Y. Yoshida, C. W. OâĂŹDell, D. Crisp, C. E. Miller, C. Frankenberg, A. Butz, I. Aben, S. Guerlet, O. Hasekamp, H. Boesch, A. Cogan, R. Parker, D. Griffith, R. Macatangay, J. Notholt, R. Sussmann, M. Rettinger, V. Sherlock, J. Robinson, E. Kyrö, P. Heikkinen, D. G. Feist, I. Morino, N. Kadygrov, D. Belikov, S. Maksyutov, T. Matsunaga, O. Uchino, and H. Watanabe. Effects of atmospheric light scattering on spectroscopic observations of greenhouse gases from space: Validation of ppdf-based co_2 retrievals from gosat. *Journal of Geophysical Research: Atmospheres*, 117(D12), 2012.

[69] S. Guerlet, A. Butz, D. Schepers, S. Basu, O. P. Hasekamp, A. Kuze, T. Yokota, J.-F. Blavier, N. M. Deutscher, D. W. T. Griffith, F. Hase, E. Kyro, I. Morino, V. Sherlock, R. Sussmann, A. Galli, and I. Aben. Impact of aerosol and thin cirrus on retrieving and validating xco_2 from gosat shortwave infrared measurements. *Journal of Geophysical Research*, 118:1–19, 2013.

[70] David Crisp, Yasjka Meijer, Rosemary Munro, Kevin Bowman, Abhishek Chatterjee, David Baker, Frederic Chevallier, Ray Nassar, Paul I. Palmer, Anna Agusti-Panareda, Jay Al-Saadi, Yotam Ariel, Sourish Basu, Peter Bergamaschi, Hartmut Boesch, Philippe Bousquet, Heinrich Bovensmann, FranÃğois-Marie BrÃľon, Dominik Brunner, Michael Buchwitz, Francois Buisson, John P. Burrows, Andre Butz, Philippe Ciais, Cathy Clerbaux, Paul Counet, Cyril Crevoisier, Sean Crowell, Philip L. DeCola, Carol Deniel, Mark Dowell, Richard Eckman, David Edwards, Gerhard Ehret, Annmarie Eldering, Richard Engelen, Brendan Fisher, Stephane Germain, Janne Hakkarainen, Ernest Hilsenrath, Kenneth Holmlund, Sander Houweling, Haili Hu, Daniel Jacob, Greet Janssens-Maenhout, Dylan Jones, Denis Jouglet, Fumie Kataoka, MatthÃd'us Kiel, Susan S. Kulawik, Akihiko Kuze, Richard L. Lachance, Ruediger Lang, Jochen Landgraf, Junjie Liu, Yi Liu, Shamil Maksyutov, Tsuneo Matsunaga, Jason McKeever, Berrien Moore, Masakatsu Nakajima, Vijay Natraj, Robert R. Nelson, Yosuke Niwa, Tomohiro Oda, Christopher W. OâĂŹDell, Leslie Ott, Prabir Patra, Steven Pawson, Vivienne Payne, Bernard Pinty, Saroja M. Polavarapu, Christian Retscher, Robert Rosenberg, Andrew Schuh, Florian M. Schwandner, Kei Shiomi, Wenying Su, Johanna Tamminen, Thomas E. Taylor, Pepijn Veefkind, Ben Veihelmann, Stephen Wofsy, John Worden, Debra Wunch, Dongxu Yang, Peng Zhang, and Claus Zehner. A constellation architecture for monitoring carbon dioxide and methane from space. Technical report, Committee on Earth Observation Satellites, 2018.

[71] Thomas E Taylor, Christopher W O'Dell, Christian Frankenberg, Philip T Partain, Heather Q Cronk, Andrey Savtchenko, Robert R Nelson, Emily J Rosenthal, Albert Y Chang, Brenden Fisher, Gregory B Osterman, Randy H Pollock, David Crisp, Annmarie Eldering, and Michael R Gunson. Orbiting carbon observatory-2 (oco-2) cloud screening algorithms: Validation against collocated modis and caliop data. *Atmospheric Measurement Techniques*, 9(3):973–989, 2016.

[72] C. Frankenberg, U. Platt, and T. Wagner. Iterative maximum a posteriori (imap)-doas for retrieval of strongly absorbing trace gases: Model studies for ch_4 and co_2 retrieval from

near infrared spectra of sciamachy onboard envisat. *Atmospheric Chemistry and Physics*, 5:9–22, 2005.

[73] Y. J. Kaufman, D. Tanré, L. A. Remer, E. F. Vermote, A. Chu, and B. N. Holben. Operational remote sensing of tropospheric aerosol over land from eos moderate resolution imaging spectroradiometer. *Journal of Geophysical Research: Atmospheres*, 102(D14):17051–17067, 1997.

[74] Zhiming Kuang, Jack Margolis, Geoffrey Toon, David Crisp, and Yuk Yung. Spaceborne measurements of atmospheric co_2 by high-resolution nir spectrometry of reflected sunlight: An introductory study. *Geophysical Research Letters*, 29(15):11–1, 2002.

[75] A. Butz, S. Guerlet, O. Hasekamp, D. Schepers, A. Galli, Ilse Aben, C. Frankenberg, J-M Hartmann, H. Tran, A. Kuze, G. Keppel-Aleks, G. Toon, D. Wunch, P. Wennberg, N. Deutscher, D. Griffith, R. Macatangay, J. Messerschmidt, J. Notholt, and T. Warneke. Toward accurate co_2 and ch_4 observations from gosat. *Geophysical Research Letters*, 38(14), 2011.

[76] R. Parker, H. Bösch, and A. Cogan. Algorithm theoretical basis document version 2 (atbdv2) the university of leicester full-physics retrieval algorithm for the retrieval of x_{co_2} and x_{ch_4}. Technical report, University of Leicester, Leicester, UK, 2011. Version 2.

[77] M. Reuter, H. Bovensmann, M. Buchwitz, J. P. Burrows, J. Heymann, and O. Schneising. Algorithm theoretical basis document version 5 (atbdv5) - the bremen optimal estimation doas (besd) algorithm for the retrieval of x_{co_2}. Technical report, Institute of Environmental Physics (IUP) University of Bremen, Bremen, Germany, 2016. Version 5.

[78] Sergey Oshchepkov, Andrey Bril, and Tatsuya Yokota. Ppdf-based method to account for atmospheric light scattering in observations of carbon dioxide from space. *Journal of Geophysical Research*, 113(D23), 2008.

[79] Maximilian Reuter, Michael Buchwitz, Oliver Schneising, Stefan Noël, Heinrich Bovensmann, and John P. Burrows. A fast atmospheric trace gas retrieval for hyperspectral instruments approximating multiple scatteringâĂŤpart 2: Application to x_{co_2} retrievals from oco-2. *Remote Sensing*, 9(11):1102, 2017.

[80] B. N. Holben, T. F. Eck, I. Slutsker, D. Tanré, J.P. Buis, A. Setzer, E. Vermote, J. A. Reagan, Y. J. Kaufman, T. Nakajima, F. Lavenu, I. Jankowiak, and A. Smirnov. Aeronet - a federated instrument network and data archive for aerosol characterization. *Remote Sensing of Environment*, 66:1–16, 1998.

[81] Michele M Rienecker, Max J Suarez, Ronald Gelaro, Ricardo Todling, Julio Bacmeister, Emily Liu, Michael G Bosilovich, Siegfried D Schubert, Lawrence Takacs, Gi-Kong Kim, Stephen Bloom, Junye Chen, Douglas Collins, Austin Conaty, Arlindo da Silva, Wei Gu, Joanna Joiner, Randal D Koster, Robert Lucchesi, Andrea Molod, Tommy Owens, Steven Pawson, Philip Pegion, Christopher R Redder, Rolf Reichle, Franklin R Robertson, Albert G Ruddick, Meta Sienkiewicz, and Jack Woollen. Merra: Nasa's modern-era retrospective analysis for research and applications. *Journal of Climate*, 24(14):3624–3648, 2011.

[82] C. Frankenberg, O. Hasekamp, C. O'Dell, S. Sanghavi, A. Butz, and J. Worden. Aerosol information content analysis of multi-angle high spectral resolution measurements and its benefit for high accuracy greenhouse gas retrievals. *Atmospheric Measurement Techniques*, 5:1809–1821, 2012.

[83] Bryan A Baum, Ping Yang, Andrew J Heymsfield, Aaron Bansemer, Benjamin H Cole, Aronne Merrelli, Carl Schmitt, and Chenxi Wang. Ice cloud single-scattering property models with the full phase matrix at wavelengths from 0.2 to 100 μm. *Journal of Quantitative Spectroscopy and Radiative Transfer*, 146:123–139, 2014.

[84] R. R. Nelson and C. W. O'Dell. The impact of improved aerosol priors on near-infrared measurements of carbon dioxide. *Atmospheric Measurement Techniques Discussions*, 2018. in review.

[85] R. R. Nelson, C. W. O'Dell, and T. E. Taylor. Simplified aerosol parameterizations in near-infrared retrievals of carbon dioxide. *Atmospheric Measurement Techniques Discussions*, 2019. in prep.

[86] Robert R Nelson, David Crisp, Lesley E Ott, and Christopher W O'Dell. High-accuracy measurements of total column water vapor from the orbiting carbon observatory-2. *Geophysical Research Letters*, 43(23), 2016.

[87] Graham W Mann, Kenneth S Carslaw, Carly L Reddington, Kirsty J Pringle, Michael Schulz, Ari Asmi, Dominick V Spracklen, David A Ridley, Matthew T Woodhouse, Lindsay A Lee, K Zhang, S. J. Ghan, R. C. Easter, X. Liu, P. Stier, Y. H. Lee, P. J. Adams, H. Tost, J. Lelieveld, S. E. Bauer, K. Tsigaridis, T. P. C. van Noije, A. Strunk, E. Vignati, N. Bellouin, M. Dalvi, C. E. Johnson, T. Bergman, H. Kokkola, K. von Salzen, F. Yu, G. Luo, A. Petzold, J. Heintzenberg, A. Clarke, J. A. Ogren, J. Gras, U. Baltensperger, U. Kaminski, S. G. Jennings, C. D. O'Dowd, R. M. Harrison, D. C. S. Beddows, M. Kulmala, Y. Viisanen, V. Ulevicius, N. Mihalopoulos, V. Zdimal, M. Fiebig, H.-C. Hansson, E. Swietlicki, and J. S. Henzing. Intercomparison and evaluation of global aerosol microphysical properties among aerocom models of a range of complexity. *Atmospheric Chemistry and Physics*, 14(9):4679–4713, 2014.

[88] O. Dubovik, T. Lapyonok, Y. J. Kaufman, M. Chin, P. Ginoux, R. A. Kahn, and A. Sinyuk. Retrieving global aerosol sources from satellites using inverse modeling. *Atmospheric Chemistry and Physics*, 8(2):209–250, 2008.

[89] G. Osterman, A. Eldering, L. Mandrake, C. O'Dell, D. Wunch, P. O. Wennberg, B. Fischer, and Y. Marchetti. Orbiting carbon observatory-2 (oco-2) lite files, bias correction, and warn level. Technical report, NASA Jet Propulsion Laboratory, California Institute of Technology, Pasadena, CA, 2017. version 2.0.

[90] D. G. Feist, S. G. Arnold, N. John, and M. C. Geibel. TCCON data from Ascension Island (SH), Release GGG2014.R0. TCCON Data Archive, hosted by CaltechDATA, 2014.

[91] P. O. Wennberg, D. Wunch, C. Roehl, J.-F. Blavier, G. C. Toon, and N. Allen. TCCON data from Caltech (US), Release GGG2014.R1. TCCON Data Archive, hosted by CaltechDATA, 2015.

[92] D. W. T. Griffith, N. M. Deutscher, V. A. Velazco, P. O. Wennberg, Y. Yavin, G. Keppel-Aleks, R. Washenfelder, G. C. Toon, J.-F. Blavier, C. Paton-Walsh, N. B. Jones, G. C. Kettlewell, B. Connor, R. C. Macatangay, C. Roehl, M. Ryczek, J. Glowacki, T. Culgan, and G. Bryant. TCCON data from Darwin (AU), Release GGG2014.R0. TCCON Data Archive, hosted by CaltechDATA, 2014.

[93] L. T. Iraci, J. Podolske, P. W. Hillyard, C. Roehl, P. O. Wennberg, J.-F. Blavier, N. Allen, D. Wunch, G. Osterman, and R. Albertson. TCCON data from Edwards (US), Release GGG2014.R1. TCCON Data Archive, hosted by CaltechDATA, 2016.

[94] R. Sussmann and M. Rettinger. TCCON data from Garmisch (DE), Release GGG2014.R0. TCCON Data Archive, hosted by CaltechDATA, 2014.

[95] F. Hase, T. Blumenstock, S. Dohe, J. Gross, and M. Kiel. TCCON data from Karlsruhe (DE), Release GGG2014.R1. TCCON Data Archive, hosted by CaltechDATA, 2015.

[96] P. O. Wennberg, D. Wunch, C. Roehl, J.-F. Blavier, G. C. Toon, and N. Allen. TCCON data from Lamont (US), Release GGG2014.R1. TCCON Data Archive, hosted by CaltechDATA, 2016.

[97] M. Dubey, H. Parker, B. Henderson, D. Green, Z. Butterfield, G. Keppel-Aleks, N. Allen, J.-F. Blavier, C. Roehl, D. Wunch, and R. Lindenmaier. TCCON data from Manaus (BR), Release GGG2014.R0. TCCON Data Archive, hosted by CaltechDATA, 2014.

[98] T. Warneke, J. Messerschmidt, J. Notholt, C. Weinzierl, N. M. Deutscher, C. Petri, P. Grupe, C. Vuillemin, F. Truong, M. Schmidt, M. Ramonet, and E. Parmentier. TCCON data from Orléans (FR), Release GGG2014.R0. TCCON Data Archive, hosted by CaltechDATA, 2014.

[99] Y. Te, P. Jeseck, and C. Janssen. TCCON data from Paris (FR), Release GGG2014.R0. TCCON Data Archive, hosted by CaltechDATA, 2014.

[100] P. O. Wennberg, C. Roehl, D. Wunch, G. C. Toon, J.-F. Blavier, R. Washenfelder, G. Keppel-Aleks, N. Allen, and J. Ayers. TCCON data from Park Falls (US), Release GGG2014.R0. TCCON Data Archive, hosted by CaltechDATA, 2014.

[101] S. Kawakami, H. Ohyama, K. Arai, H. Okumura, C. Taura, T. Fukamachi, and M. Sakashita. TCCON data from Saga (JP), Release GGG2014.R0. TCCON Data Archive, hosted by CaltechDATA, 2014.

[102] R. Kivi and P. Heikkinen. Fourier transform spectrometer measurements of column co_2 at sodankylä, finland. *Geoscientific Instrumentation, Methods and Data Systems*, 5(2):271–279, 2016.

[103] W. Peters, A. R. Jacobson, C. Sweeney, A. E. Andrews, T. J. Conway, K. Masarie, J. B. Miller, L. M. P. Bruhwiler, G. Pétron, A. I. Hirsch, D. E. J. Worthy, G. R. van der Werf, J. T. Randerson, P. O. Wennberg, M. C. Krol, and P. P. Tans. An atmospheric perspective on north american carbon dioxide exchange: Carbontracker. *Proceedings of the National Academy of Science of the United States of America*, 104(48):18925–18930, nov 2007.

[104] L. Feng, P. I. Palmer, Y. Yang, R. M. Yantosca, S. R. Kawa, J.-D. Paris, H. Matsueda, and T. Machida. Evaluating a 3-d transport model of atmospheric co_2 using ground-based, aircraft, and space-borne data. *Atmospheric Chemistry and Physics*, 11(6):2789–2803, 2011.

[105] S. M. R. Crowell, S. R. Kawa, E. V. Browell, Dorit M. Hammerling, Berrien Moore, Kevin Schaefer, and Scott C. Doney. On the ability of space-based passive and active remote sensing observations of co_2 to detect flux perturbations to the carbon cycle. *Journal of Geophysical Research: Atmospheres*, 123(2):1460–1477, 2018.

[106] Christian Rödenbeck. Estimating co_2 sources and sinks from atmospheric mixing ratio measurements using a global inversion of atmospheric transport. Technical Report 6, Max Planck Institue für Biogeochemie, 2005. Technical Report 6.

[107] Antje Inness, Frank Baier, Angela Benedetti, Idir Bouarar, Simon Chabrillat, Hannah Clark, Cathy Clerbaux, P Coheur, R. J. Engelen, Quentin Errera, J. Flemming, M. George, C. Granier, J. Hadji-Lazaro, V. Huijnen, D. Hurtmans, L. Jones, J. W. Kaiser, J. Kapsomenakis, K. Lefever, J. Leitao, M. Razinger, A. Richter, M. G. Schultz, A. J. Simmons, M. Suttie, O. Stein, J.-N. Thépaut, V. Thouret, M. Vrekoussis, and C. Zerefos. The macc reanalysis: an 8 yr data set of atmospheric composition. *Atmospheric Chemistry and Physics*, 13:4073–4109, 2013.

[108] John V Martonchik, David J Diner, Ralph A Kahn, Thomas P Ackerman, Michel M Verstraete, Bernard Pinty, and Howard R Gordon. Techniques for the retrieval of aerosol properties over land and ocean using multiangle imaging. *IEEE Transactions on Geoscience and Remote Sensing*, 36(4):1212–1227, 1998.

[109] Brigitte Koffi, Michael Schulz, François-Marie Bréon, Frank Dentener, Birthe Marie Steensen, Jan Griesfeller, David Winker, Yves Balkanski, Susanne E Bauer, Nicolas Bellouin, T Bernsten, H Bian, M Chin, T Diehl, R Easter, S Ghan, D. A. Hauglustaine, T. Iversen, A. Kirkevåg, X. Liu, U. Lohmann, G. Myhre, P. Rasch, Ø Seland, R. B. Skeie, S. D. Steenrod, P. Stier, J. Tackett, T. Takemura, K. Tsigaridis, M. R. Vuolo, J. Yoon, and K. Zhang. Evaluation of the aerosol vertical distribution in global aerosol models through comparison against caliop measurements: Aerocom phase ii results. *Journal of Geophysical Research: Atmospheres*, 121(12):7254–7283, 2016.

[110] Zak Kipling, Philip Stier, Colin E Johnson, Graham W Mann, Nicolas Bellouin, Susanne E Bauer, Tommi Bergman, Mian Chin, Thomas Diehl, Steven J. Ghan, T. Iversen, A. Krikevåg, H. Kokkola, X. Liu, G. Luo, T. van Noije, K. J. Pringle, K. von Salzen, M. Schulz, Ø Seland, R. B. Skeie, T. Takemura, K. Tsigaridis, and K. Zhang. What controls

the vertical distribution of aerosol? relationships between process sensitivity in hadgem3–ukca and inter-model variation from aerocom phase ii. *Atmospheric Chemistry and Physics*, 16(4):2221–2241, 2016.

[111] R. R. Nelson. The impact of aerosols on space-based retrievals of carbon dioxide. Master's thesis, Colorado State University, 2015.

[112] S. S. Kulawik, C. O'Dell, R. R. Nelson, and T. E. Taylor. Validation of oco-2 error analysis using simulated retrievals. *Atmos. Meas. Tech. Discuss.*, 2018. in review.

[113] David Crisp, Harold R Pollock, Robert Rosenberg, Lars Chapsky, Richard AM Lee, Fabiano A Oyafuso, Christian Frankenberg, Christopher W O'Dell, Carol J Bruegge, Gary B Doran, A. Eldering, B. M. Fisher, D. Fu, M. R. Gunson, L. Mandrake, G. B. Osterman, F. M. Schwandner, K. Sun, T. E. Taylor, P. O. Wennberg, and D. Wunch. The on-orbit performance of the orbiting carbon observatory-2 (oco-2) instrument and its radiometrically calibrated products. *Atmospheric Measurement Techniques*, 10(1):59–81, 2017.

[114] D. M. O'Brien, I. Polonsky, C. O'Dell, and A. Carheden. Orbiting carbon observatory (oco), algorithm theoretical basis document: The oco simulator issn 0737-5352-85. Technical report, Cooperative Institute for Research in the Atmosphere, Colorado State University, 2009.

[115] D. M. Winker, M. A. Vaughan, A. Omar, Y. Hu, and K. A. Powell. Overview of the calipso mission and caliop data processing algorithms. *Journal of Atmospheric and Oceanic Technology*, 26:2310–2323, 2009.

[116] J. P. Veefkind, I. Aben, K. McMullan, H. Förster, J. De Vries, G. Otter, J. Claas, H. J. Eskes, J. F. De Haan, Q. Kleipool, M. van Weele, O. Hasekamp, R. Hoogeveen, J. Landgraf, R. Snel, P. Tol, P. Ingmann, R. Voors, B. Kruizinga, R. Vink, H. Visser, and P.F. Levelt. Tropomi on the esa sentinel-5 precursor: A gmes mission for global observations of the at-

mospheric composition for climate, air quality and ozone layer applications. *Remote Sensing of Environment*, 120:70–83, 2012.

[117] Steven T Massie, K Sebastian Schmidt, Annmarie Eldering, and David Crisp. Observational evidence of 3-d cloud effects in oco-2 co_2 retrievals. *Journal of Geophysical Research Atmospheres*, 122(13):7064–7085, 2017.

[118] Frank J Wentz and Roy W Spencer. Ssm/i rain retrievals within a unified all-weather ocean algorithm. *J. Atmos. Sci.*, 55(9):1613–1627, 1998.

[119] Hal J Bloom. The cross-track infrared sounder (cris): a sensor for operational meteorological remote sensing. *Geoscience and Remote Sensing Symposium, 2001. IGARSS'01. IEEE 2001 International*, 3:1341–1343, 2001.

[120] John J Bates and Darren L Jackson. Trends in upper-tropospheric humidity. *Geophys. Res. Lett.*, 28(9):1695–1698, 2001.

[121] Bo-Cai Gao and Yoram J Kaufman. Water vapor retrievals using moderate resolution imaging spectroradiometer (modis) near-infrared channels. *J. Geophys. Res. Atmos.*, 108(D13), 2003.

[122] P Albert, R Bennartz, R Preusker, R Leinweber, and J Fischer. Remote sensing of atmospheric water vapor using the moderate resolution imaging spectroradiometer. *J. Atmos. Ocean Tech.*, 22(3):309–314, 2005.

[123] Ralf Bennartz and Jürgen Fischer. Retrieval of columnar water vapour over land from backscattered solar radiation using the medium resolution imaging spectrometer. *Remote Sens. Environ.*, 78(3):274–283, 2001.

[124] R Lindstrot, R Preusker, H Diedrich, L Doppler, R Bennartz, and J Fischer. 1d-var retrieval of daytime total columnar water vapour from meris measurements. *Atmos. Meas. Tech.*, 5(3):631–646, 2012.

[125] M. Grossi, P. Valks, D. Loyola, B. Aberle, S. Slijkhuis, T. Wagner, S. Beirle, and R. Lang. Total column water vapour measurements from gome-2 metop-a and metop-b. *Atmos. Meas. Tech.*, 8:1111–1133, 2015.

[126] I. Gordon. personal communication, 2012.

[127] Laurence S Rothman, Iouli E Gordon, Yury Babikov, Alain Barbe, D Chris Benner, Peter F Bernath, Manfred Birk, Luca Bizzocchi, Vincent Boudon, Linda R Brown, A. Campargue, K. Chance, E. A. Cohen, L. H. Coudert, V. M. Devi, B. J. Drouin, A. Fayt, J.-M. Flaudk, R. R. Gamache, J. J. Harrison, J.-M. Hartmann, C. Hill, J. T. Hodges, D. Jacquemart, A. Jolly, J. Lamouroux, R. J. Le Roy, G. Li, D. A. Long, O. M. Lyuli, C. J. Mackie, S. T. Massie, S. Mikhailenko, H. S. P. Müller, O. V. Naumenko, A. V. Nikitin, J. Orphal, V. Perevalov, A. Perrin, E. R. Polovtseva, C. Richard, M. A. H. Smith, E. Starikova, K. Sung, S.Tashkun, J. Tennyson, G. C. Toon, Vl. G. Tyuterev, and G. Wagner. The hitran2012 molecular spectroscopic database. *Journal of Quantitative Spectroscopy and Radiative Transfer*, 130:4–50, 2013.

[128] Eli J Mlawer, Vivienne H Payne, Jean-Luc Moncet, Jennifer S Delamere, Matthew J Alvarado, and David C Tobin. Development and recent evaluation of the mt_ckd model of continuum absorption. *Philosophical Transactions of the Royal Society of London A: Mathematical, Physical and Engineering Sciences*, 370(1968):2520–2556, 2012.

[129] C. Frankenberg, R. Pollock, R. A. M. Lee, R. Rosenberg, J.-F. Blavier, D. Crisp, C. W. O'Dell, G. B. Osterman, C. Roehl, P. O. Wennberg, and D. Wunch. The orbiting carbon observatory (oco-2): spectrometer performance evaluation using pre-launch direct sun measurements. *Atmospheric Measurement Techniques*, 8:301–313, 2015.

[130] ECMWF. Ecmwf ifs documentation. Technical report, European Centre for Medium-Range Weather Forecasts, 2015. Last access: February 2016.

[131] T. E. Taylor, C. W. O'Dell, D. M. O'Brien, N. Kikuchi, T. Yokotaand T. Y. Nakajima, H. Ishida, D. Crisp, and T. Nakajima. Comparison of cloud-screening methods applied to gosat near-infrared spectra. *IEEE Transactions on Geoscience and Remote Sensing*, 50:295–309, 2012.

[132] Eugenia Kalnay, Masao Kanamitsu, Robert Kistler, William Collins, Dennis Deaven, Lev Gandin, Mark Iredell, Suranjana Saha, Glenn White, John Woollen, Y. Zhu, M. Chelliah, W. Ebisuzaki, W. Higgins, J. Janowiak, K. C. Mo, C. Ropelewski, J. Wang, A. Leetmaa, R. Reynolds, Roy Jenne, and Dennis Joseph. The ncep/ncar 40-year reanalysis project. *B. Am. Meteorol. Soc.*, 77(3):437–471, 1996.

[133] Randolph H Ware, David W Fulker, Seth A Stein, David N Anderson, Susan K. Avery, Richard D. Clark, Kelvin K. Droegemeier, Joachim P. Kuettner, J. Bernard Minster, and Soroosh Sorooshian. Suominet: A real-time national gps network for atmospheric research and education. *B. Am. Meteorol. Soc.*, 81(4):677, 2000.

[134] Imke Durre, Russell S Vose, and David B Wuertz. Overview of the integrated global radiosonde archive. *J. Climate*, 19(1):53–68, 2006.

[135] K. Imaoka, M. Kachi, M. Kasahara, N. Ito, K. Nakagawa, and T. Oki. Instrument performance and calibration of amsr-e and amsr2. *Int. Arch. Photogram. Rem. Sens. Spatial Inform. Sci.*, 38(8):13–18, 2010.

[136] J. A. Reagan, K. Thome, B. Herman, and R. Gall. Water vapour measurements in the 0.94 μm absorption band: calibration measurements and data applications. *Proceedings of the International Geoscience Remote on Sensing Symposium IEEE*, 87:2434–9, 1987.

[137] B. Schmid, K. J. Thorne, Philippe Demoulin, R. Peter, C. Mätzler, and J. Sekler. Comparison of modeled and empirical approaches for retrieving columnar water vapor from solar transmittance measurements in the 0.94-μm region. *J. Geophys. Res. Atmos.*, 101(D5):9345–9358, 1996.

[138] J. J. Michalsky, J. C. Liljegren, and L. C. Harrison. A comparison of sun photometer derivations of total column water vapor and ozone to standard measures of same at the southern great plains atmospheric radiation measurement site. *J. Geophys. Res. Atmos.*, 100(D12):25995–26003, 1995.

[139] Hungjui Yu, Paul E Ciesielski, Junhong Wang, Hung-Chi Kuo, Holger Vömel, and Ruud Dirksen. Evaluation of humidity correction methods for vaisala rs92 tropical sounding data. *J. Atmos. Ocean Tech.*, 32(3):397–411, 2015.

[140] Junhong Wang, Liangying Zhang, Aiguo Dai, Franz Immler, Michael Sommer, and Holger Vömel. Radiation dry bias correction of vaisala rs92 humidity data and its impacts on historical radiosonde data. *J. Atmos. Ocean Tech.*, 30(2):197–214, 2013.

[141] David I Duncan and Christian D Kummerow. A 1dvar retrieval applied to gmi: Algorithm description, validation, and sensitivities. *J. Geophys. Res. Atmos.*, 121:7415âĂŞ–7429, 2016.

[142] F. J. Wentz, T. Meissner, C. Gentemann, K. A. Hilburn, and J. Scott. Remote sensing systems gcom-w1 amsr2 daily environmental suite on 0.25 deg grid, version 7.2. Technical report, Remote Sensing Systems, Santa Rosa, CA., 2014. Last access: 19 April 2016.

[143] Zhenhong Li, Jan-Peter Muller, and Paul Cross. Comparison of precipitable water vapor derived from radiosonde, gps, and moderate-resolution imaging spectroradiometer measurements. *J. Geophys. Res. Atmos.*, 108(D20), 2003.

[144] H. Diedrich, R. Preusker, R. Lindstrot, and J. Fischer. Retrieval of daytime total columnar water vapour from modis measurements over land surfaces. *Atmos. Meas. Tech.*, 8(2):823–836, 2015.

[145] Lukas Mandrake, Chris O'Dell, Debra Wunch, Paul O. Wennberg, Brendan Fisher, Gregory B. Osterman, and Annmarie Eldering. Lite files, warn level and bias correction deter-

mination. Technical report, Jet Propulsion Laboratory, California Institute of Technology, Pasadena, California, 2015.

[146] L. Mandrake, C. Frankenberg, C. W. O'Dell, G. Osterman, P. Wennberg, and D. Wunch. Semi-autonomous sounding selection for oco-2. *Atmospheric Measurement Techniques*, 6:2851–2864, 2013.

[147] M. G. Bosilovich, Santha Akella, Lawrence Coy, Richard Cullather, Clara Draper, Ronald Gelaro, Robin Kovach, Qing Liu, Andrea Molod, Peter Norris, Krzysztof Wargan, Winston Chao, Rolf Reichle, Lawrence Takacs, Yury Vikhliaev, Steve Bloom, Allison Collow, Stacey Firth, Gordon Labow, Gary Partyka, Steven Pawson, Oreste Reale, Siegfried D. Schubert, and Max Suarez. Merra-2: Initial evaluation of the climate. *NASA Technical Report Series on Global Modeling and Data Assimilation, NASA/TM-2015*, 104606, 2015.

[148] Daniel Pérez-Ramírez, David N Whiteman, Alexander Smirnov, Hassan Lyamani, Brent N Holben, Rachel Pinker, Marcos Andrade, and Lucas Alados-Arboledas. Evaluation of aeronet precipitable water vapor versus microwave radiometry, gps, and radiosondes at arm sites. *J. Geophys. Res. Atmos.*, 119(15):9596–9613, 2014.

[149] D. Crisp. Measuring atmospheric carbon dioxide from space with the orbiting carbon observatory-2 (oco-2). *Proc. SPIE*, pages 960702–960702, 2015.

Appendix A

High-Accuracy Measurements of Total Column Water Vapor from the Orbiting Carbon Observatory-2

A.1 The Importance of Water Vapor

While the primary measurement of OCO-2 is column CO_2, numerous other products are being developed and validation, one of which is total column water vapor (TCWV). These measurements are an ancillary product of the primary ACOS retrieval algorithm, with information coming from three highly resolved spectral bands. Water vapor is important in how it influences the radiation budget, hydrologic cycle, weather patterns, and climate change. Improved knowledge of water vapor could lead to an enhanced understanding in all of these fields. Currently, global spaced-based information on water vapor comes from a number of satellite instruments. First, there are sensors that operate at microwave wavelengths such as the Special Sensor Microwave Imager [118], the Advanced Microwave Scanning Radiometer Earth Observing System, the Advanced Microwave Scanning Radiometer 2 (AMSR2), the Tropical Rainfall Measuring Mission Microwave Imager, and the Global Precipitation Measurement Microwave Imager. Second, sensors that operate at thermal infrared wavelengths such as the Atmospheric Infrared Sounder (AIRS; [45]), the Infrared Atmospheric Sounding Interferometer (IASI; [46]), the Cross-track Infrared Sounder [119], and the High-resolution Infrared Radiation Sounder [120]. Third, sensors that operate at near-infrared wavelengths such as MODIS [121, 122] and the MEdium Resolution Imaging Spectrometer (MERIS) [123, 124]. Finally, sensors that operate at visible wavelengths such as the Global Ozone Monitoring Experiment-2 [125]. Over ocean, microwave and infrared sensors are typically used, as the surface temperature and emissivity are relatively well-known. Over land, emissivity constraints result in a preference towards near-infrared sensors.

At the near-infrared wavelengths that OCO-2 observes, there are many H_2O lines present. If these absorption features and H_2O's foreign broadening impact on the CO_2 lines are not accounted for, biases are introduced into the X_{CO_2} retrieval. Thus, one of the retrieved variables in the ACOS algorithm is total column water vapor (TCWV), which is defined as the total gaseous water contained in a vertical column of atmosphere. The unit of TCWV throughout this work is the millimeter (mm), where 1 mm is equal to 1 kg/m^2. Absorption coefficient tables (ABSCO v4.2) were created using H_2O lines from a custom list, similar to the line list used in the HIgh-resolution TRANsmission molecular absorption database compilation (HITRAN2012; [126, 127]). The H_2O continuum model used is a custom version of the Mlawer-Tobin-Clough-Kneizys-Davies model [128]. These ABSCO tables are used to supply absorption cross section values for the retrieved gases and are critically important in retrieving nearly bias-free measurements. The inclusion of TCWV in the ACOS retrieval leads to the following question: how well can OCO-2 retrieve H_2O information?

A.2 Theoretical Basis

As water is a nonlinear molecule with a net dipole moment, many rotational and vibrational absorption features exist throughout the electromagnetic spectrum. OCO-2 resolves a number of strong H_2O absorption features in both its 1.61 and 2.06 μm bands. Figure A.1 shows an example of absorption features in these bands, as seen through the OCO-2 spectral response function. While the majority of the lines are due to carbon dioxide, many water vapor lines are also evident. In an atmosphere devoid of clouds and aerosols, the relative line depth is directly related to TCWV. The lines are well-resolved, and because of OCO-2's high signal-to-noise ratio of several hundred to greater than 1000 [129], even small changes in the relative line depth can be detected.

The ACOS algorithm uses the European Centre for Medium-Range Weather Forecasts Integrated Forecast System (ECMWF IFS; [130]) for meteorological *a priori* information on temperature, water vapor, and surface pressure and retrieves a single scaling factor applied to the ECMWF water vapor profile. This is done to reduce possible correlations between the retrieved X_{CO_2} and

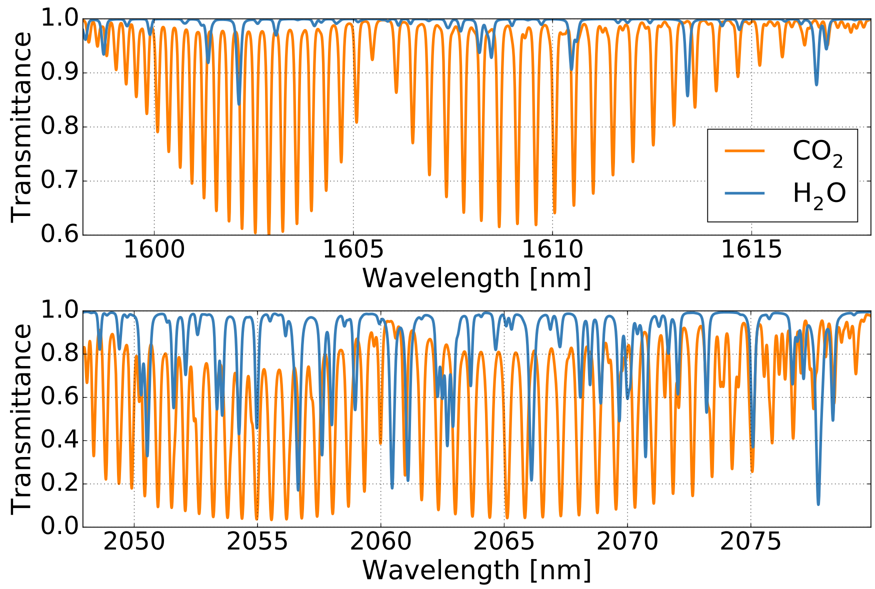

Figure A.1: Simulated OCO-2 1.61 μm band (top panel) and 2.06 μm band (bottom panel) transmittance spectra in a typical downward-looking observation, demonstrating the prevalence of water vapor absorption features (blue) within the CO_2| absorption bands (orange).

water vapor. Because the ACOS algorithm is given the precise spectral response function and SNR of the instrument, the optimal estimation approach produces an estimate of the uncertainty in its retrieved TCWV. This estimate is typically only 0.1-0.2 mm and includes errors due to both instrument noise as well as cross-talk errors due to other retrieved variables such as aerosols and carbon dioxide. However, the estimate does not include errors in the prescribed ECMWF vertical profile of water vapor and may not fully account for errors due to clouds and aerosols, so it may be an underestimate. This theoretical uncertainty therefore serves as a useful lower limit of the actual TCWV retrieval error.

We next improve on this estimate by performing retrievals on simulated spectra in realistic atmospheres created using the CSU Orbit Simulator [114]. These simulations include realistic representations of the viewing geometry and surface reflectance, profiles of clouds and aerosols from the Cloud–Aerosol Lidar with Orthogonal Polarization (CALIOP) instrument onboard the Cloud-Aerosol Lidar and Infrared Pathfinder Satellite Observations (CALIPSO; [115]), and meteorology from ECMWF. Gaussian instrument noise is also added to the spectra. For more details on the methodology, see [56]. Scenes contaminated by clouds and aerosols are rejected via a spectral-based cloud-screening technique [71, 131], as OCO-2 is only able to make accurate retrievals in scenes nearly free of cloud and aerosol contamination. However, scenes passing this pre-filter may still contain some clouds and aerosols, typically with an optical depth less than 0.3.

ACOS retrievals were then performed on scenes passing the cloud and aerosol pre-filter. To challenge our retrieval, we set the prior meteorological data to be from the National Centers for Environmental Prediction/National Center for Atmospheric Research (NCEP/NCAR) Reanalysis-1 [132], rather than from ECMWF, as a proxy for realistic errors in water vapor amount and vertical distribution, as well as errors in the temperature profile and surface pressure. Despite these errors sources, we were able to retrieve TCWV values with an almost perfect correlation with the true water vapor (R=0.999) and effectively no bias (-0.08 mm) compared to the true TCWV used to create the synthetic measurements (Figure A.2). The root mean squared deviation (RMSD) between the retrieved TCWV and true TCWV was reduced from about 4 mm (7 mm) in the prior (Table A.1) to 0.39 mm (0.75 mm) in the retrieval over land (ocean) (see Tables S1 and S2 in the supplementary material). This mean error of about 0.6 mm is higher than the simple theoretical estimate of approximately 0.1-0.2 mm likely because of additional cloud and aerosol light path modification effects but also potentially because of errors in the prior temperature profile, surface pressure, and water vapor profile shape.

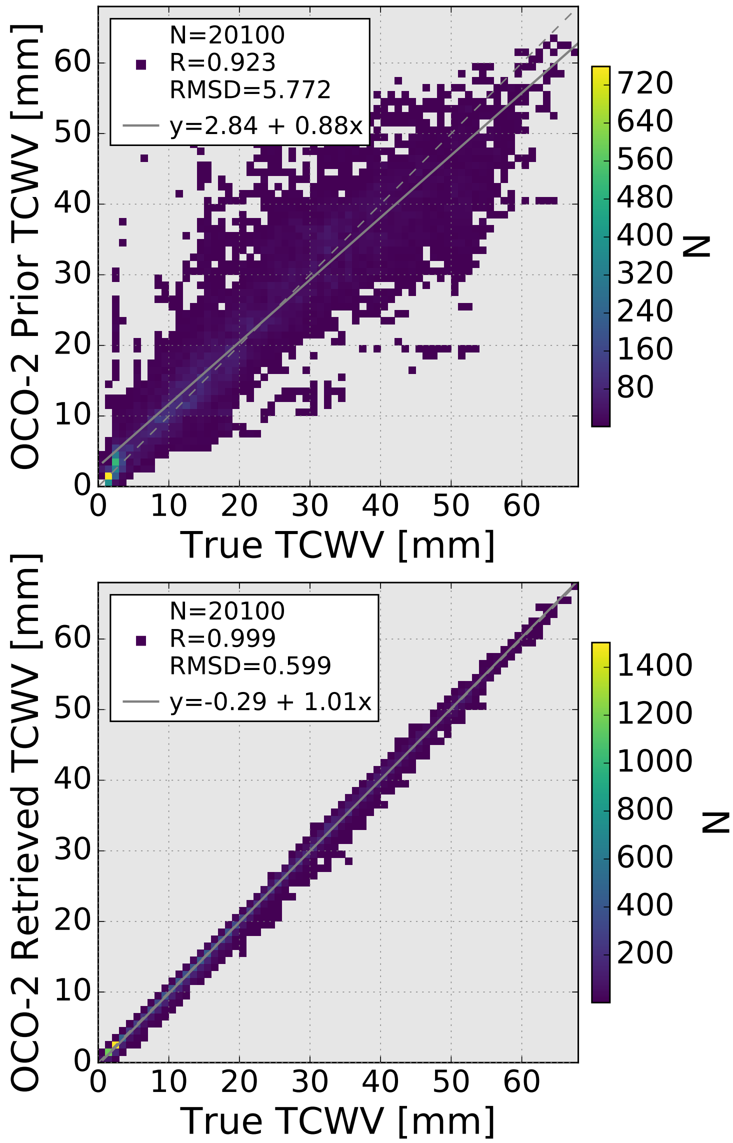

Figure A.2: The top panel shows a heatmap comparison of the prior OCO-2 TCWV, taken from the NCEP/NCAR reanalysis, to the true synthetic TCWV (created using ECMWF). The bottom panel shows a heatmap comparison of the retrieved OCO-2 TCWV to the true synthetic TCWV.

Table A.1: OCO-2 Prior TCWV Validation: Simulations.

Validation	Mode	N	Surface	Bias (mm)	σ (mm)	$\sigma\mu$ (%)	RMSD (mm)
True Scene	N&G	21000	Land & Ocean	0.44	5.75	27.7	5.77
	N	9813	Land	0.88	4.01	29.3	4.11
	G	10287	Ocean	0.02	7.00	25.4	7.00

Table A.2: OCO-2 Retrieved TCWV Validation: Simulations

Validation	Mode	N	Surface	Bias (mm)	σ (mm)	$\sigma\mu$ (%)	RMSD (mm)	Variance Reduced (%)
True Scene	N&G	21000	Land & Ocean	-0.10	0.59	2.9	0.60	98.9
	N	9813	Land	-0.13	0.36	2.9	0.39	99.2
	G	10287	Ocean	-0.08	0.74	2.7	0.75	98.9

A.3 Data

We now extend our analysis to real OCO-2 data by comparing OCO-2 TCWV measurements to four TCWV validation sources: SuomiNet [133], the AErosol RObotic NETwork (AERONET) [80], the Integrated Global Radiosonde Archive (IGRA) [134], and the Advanced Microwave Scanning Radiometer 2 (AMSR2) [135]. SuomiNet is a ground-based Global Positioning System (GPS) network that measures TCWV concentrations using the time delay in the 1.6 and 1.2 GHz GPS signals. As a GPS satellite passes overhead, the transmitted signal is slowed by Earth's atmosphere and the time it takes to reach a given SuomiNet instrument on the ground is recorded. The delay in this time is a function of how much water vapor is in the column of air, the temperature profile, etc. Using a simple equation, TCWV can then be retrieved with an estimated accuracy of 1-2 mm [133]. AERONET is a ground-based sun-photometer network primarily designed to measure aerosol properties. Each AERONET instrument tracks the sun as it travels across the sky and uses measured radiances to infer column values of several quantities, including water vapor (using a band around 0.94 μm via the Direct Sun Algorithm version 2) [136, 137] with a reported accuracy of better than 2 mm [138]. IGRA is a collection of radiosonde and pilot balloon observations from over 1,500 globally distributed stations. While primarily used for operational weather forecasting, radiosonde observations have also been used for other applications including the verification of satellite measurements. [139] found mean differences in TCWV between radiosondes and a ground-based microwave radiometer of 0.9 mm. An exponential fit to each IGRA profile was used to account for any water vapor present above the altitude at which the radiosonde stopped taking data. Only Vaisala RS92s were used in this study, as they have been extensively validated (e.g. [139, 140]). We also required each profile to contain at least 30 vertical measurements. The primary limitation of these three ground-based networks is their lack of coverage over ocean and sparse coverage over land, which restricted the number of co-locations as OCO-2's orbit track is less than 10 km wide and has a repeat cycle of approximately 16 days. Additionally, the infrequent launch times of radiosondes (typically only 0Z and 12Z) further restrict the number of available co-locations of IGRA with OCO-2. The fourth validation source, AMSR2, is a radiometer that measures water vapor at microwave wavelengths over ocean using horizontally and vertically polarized channels at 18.7, 23.8, and 36.5 GHz. It flies in the Afternoon Constellation a few minutes behind OCO-2 and thus provides a substantial number of co-located measurements. [141] found a RMSD between AMSR2 and a radiosonde dataset of 2.6 mm. For this work, the Remote Sensing Systems 0.25° gridded TCWV product was used (version 7.2; [142]). The MODIS instrument on NASA's Aqua satellite, despite being in the Afternoon Constellation with OCO-2, was not selected as a validation source, as its water vapor errors are likely larger than those from OCO-2 (e.g. [121, 143]). While a custom retrieval has been shown to have smaller errors than the operational algorithm [144], our previously described validation sources over land were considered sufficient.

To compare to OCO-2 TCWV measurements to SuomiNet and AERONET, co-location criteria of 30 minutes in time and 0.1° latitude (about 11 km) in space were chosen. We examined the potential of expanding the co-location thresholds in order to increase the number of matched measurements but found that the differences between the OCO-2 and validation TCWV values increased substantially for larger thresholds, indicating that the spatial and temporal variability of water vapor imposes limits on the chosen co-location thresholds. Figure A.3 shows a minimum in RMSD between OCO-2 and SuomiNet TCWV using a co-location distance threshold of about 0.1° latitude. Smaller spatial co-location thresholds than about 0.1° have a larger RMSD because there are too few remaining SuomiNet measurements. In an attempt to increase the number of IGRA co-locations, we allowed radiosondes within 0.1° to have been launched up to an hour before the corresponding OCO-2 measurement, as radiosonde balloons typically take 1-2 hours to ascend through the atmosphere. We also applied a station surface pressure or station altitude difference threshold to ensure that OCO-2 was not measuring substantially shorter or longer path lengths (and thus retrieving less or more water vapor, which is concentrated near the surface). Against SuomiNet and IGRA, a surface pressure difference threshold of less than 10 hPa was used while against AERONET an altitude difference threshold of less than 100 m was used. The chosen thresholds removed expected biases that were appearing when OCO-2 measurements were sampling columns of air much higher or lower in elevation than the nearby SuomiNet, AERONET, or IGRA station. We chose to reject data instead of trying to apply a custom water vapor correction because water vapor is highly concentrated near the surface and thus any errors or uncertainty in the correction could represent a disproportionately large fraction of the total TCWV.

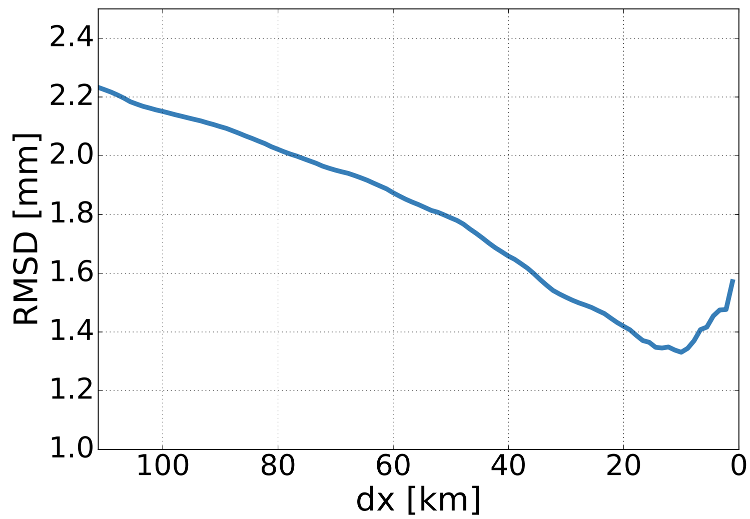

Figure A.3: RMSD between OCO-2 TCWV and SuomiNet TCWV as a function of co-location distance threshold (dx).

OCO-2 measurements (ACOS B7 lite files; [145]) from 6 September 2014 to 10 February 2016 were used for this study. As was done for the simulated measurements, the pre-filter of [71, 131] was used to eliminate scenes contaminated by clouds and aerosols. Despite this, some poor retrievals remain in the dataset, typically due to uncorrected cloud and aerosol effects. The ACOS B7 “lite" files used at the time of this writing only include data passing an additional “warn-level" based filter (warn level less than 17, see [146] for details).

OCO-2 nadir and glint measurements over land and glint measurements over ocean were used for this study. Glint geometry, where the satellite views a surface footprint near the sun-glint spot on the earth’s surface, is primarily used over oceans but, due to satellite maneuvering restrictions, is also used over land. Land has a sufficiently strong surface reflectance in glint geometry and thus enables the use of glint measurements along with nadir (downward looking) measurements.

Target mode measurements, where OCO-2 dithers across a specific target and gathers thousands of measurements, were excluded from the main analysis. This was to avoid having the statistics overly influenced by a large number of measurements co-located with a small number of validation measurements. The target mode measurements, however, agreed with our overall conclusions (Table A.3). Figure A.4 shows the location of the 282 SuomiNet stations, 83 AERONET stations, 12 IGRA stations, and 229,390 0.25°x0.25° AMSR2 grid cells that had at least one co-located OCO-2 measurement for this study.

Table A.3: OCO-2 TCWV Validation

Validation	Mode	N	Surface	Bias (mm)	σ (mm)	$\sigma\mu$ (%)	RMSD (mm)	Variance Reduced (%)
SuomiNet	N&G	13306	Land	0.34	1.29	7.2	1.34	65.7
	N	8026	Land	0.31	1.24	7.5	1.28	60.7
	G	5280	Land	0.38	1.37	6.7	1.42	69.1
	T	24787	Land	0.75	1.03	7.8	1.27	-23.4
AERONET	N&G	2703	Land	1.42	1.51	9.0	2.07	68.7
	N	1365	Land	1.41	1.28	7.6	1.90	74.7
	G	1338	Land	1.43	1.72	10.1	2.24	63.6
	T	34223	Land	0.97	1.95	13.7	2.18	-26.5
IGRA	N&G	639	Land	0.41	1.74	8.6	1.79	55.0
	N	416	Land	0.79	1.51	8.3	1.70	69.4
	G	223	Land	-0.30	1.90	8.0	1.93	-9.1
AMSR2	G	8923137	Ocean	-0.44	0.81	2.8	0.92	86.6

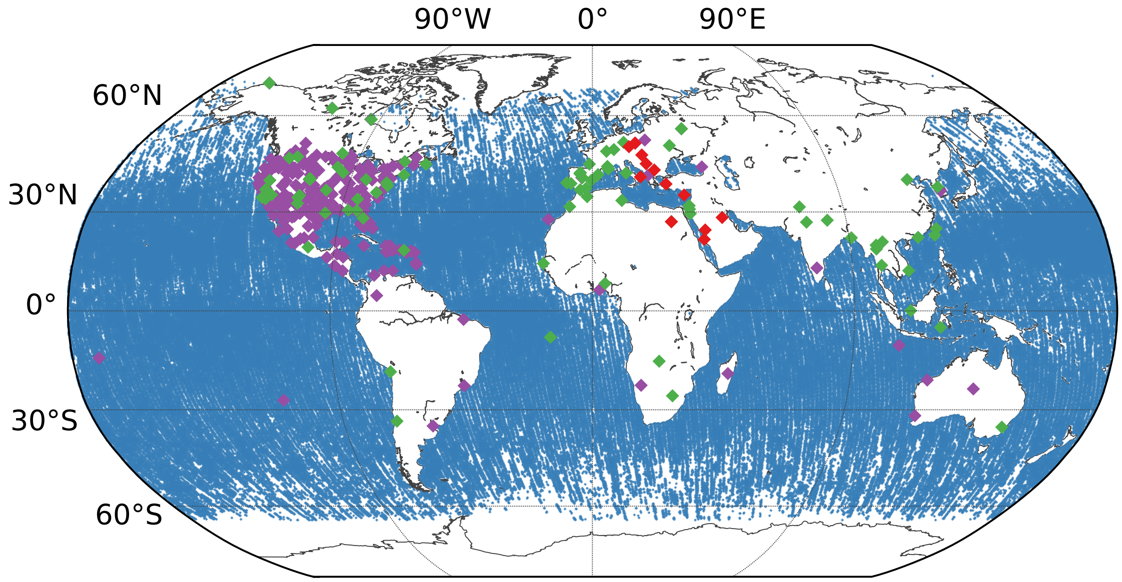

Figure A.4: Location of SuomiNet sites (purple), AERONET sites (green), IGRA sites (red), and AMSR2 grid cells (blue) that have a valid OCO-2 measurement co-located in time and space from 6 September 2014 to 10 February 2016.

As previously stated, OCO-2 uses ECMWF model output as its meteorological prior. This gave us an opportunity to see if the OCO-2 retrieval is able to improve upon model output, which would indicate that OCO-2 TCWV measurements may be useful in improving numerical prediction models. Additionally, we co-located OCO-2 TCWV measurements with the Modern-Era Retrospective analysis for Research and Applications Version 2 (MERRA-2; [147]), to provide a model comparison independent of the OCO-2 retrieval framework. MERRA-2 is a 3-hourly, 0.625°x0.5° atmospheric reanalysis produced by the NASA Global Modeling and Assimilation Office.

A.4 Validation

Comparing OCO-2 TCWV measurements to our four validation sources, Figure A.5 demonstrates that ACOS is able to retrieve TCWV with relatively high accuracy and small biases. The ECMWF TCWV values, used as the prior, have RMSDs of about 2.2 mm, 3.4 mm, 2.6 mm, and 2.3 mm relative to SuomiNet, AERONET, IGRA, and AMSR2, respectively (Figure A.6 and Table A.4). The OCO-2 retrievals (Figure A.5) are able to reduce these RMSDs down to about 1.3

mm, 2.1 mm, 1.8 mm, and 0.9 mm. The correlation coefficients relative to the prior are improved against all four validation sources and represent a reduction in error variance of 66%, 69%, 55%, and 87% for SuomiNet, AERONET, IGRA, and AMSR2, respectively. The mean bias relative to SuomiNet, IGRA, and AMSR2 are 0.3, 0.4 mm, and -0.4 mm, respectively, while the AERONET TCWV measurements appear to be low biased by approximately 1.4 mm (see Table S3 in the supplementary material). The slope of the best-fit line for AERONET is about 1.07 which equates to a low bias of 7% relative to the retrieved OCO-2 TCWV values.

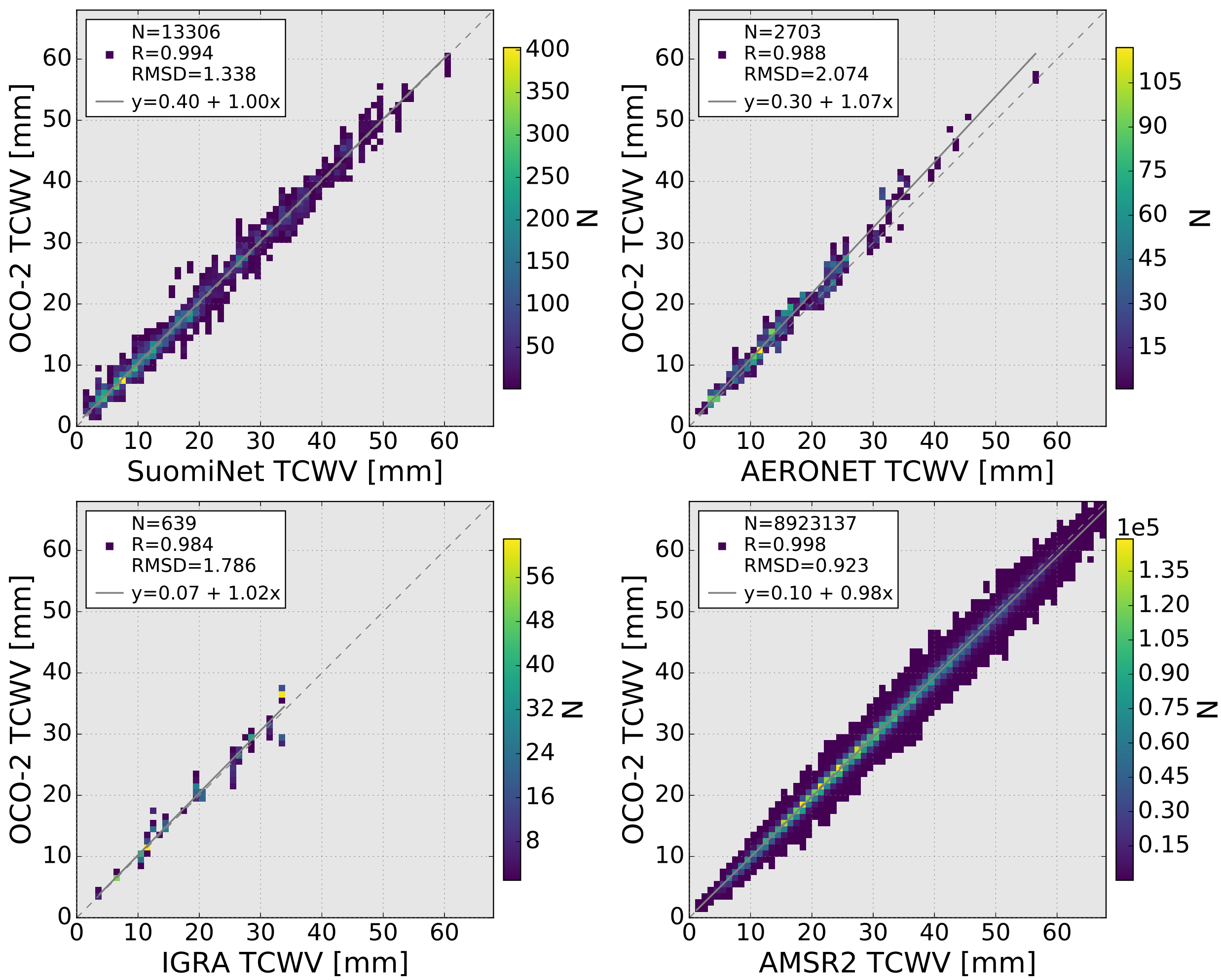

Figure A.5: Heatmap comparison of the retrieved OCO-2 TCWV to SuomiNet, AERONET, IGRA, and AMSR2 TCWV measurements.

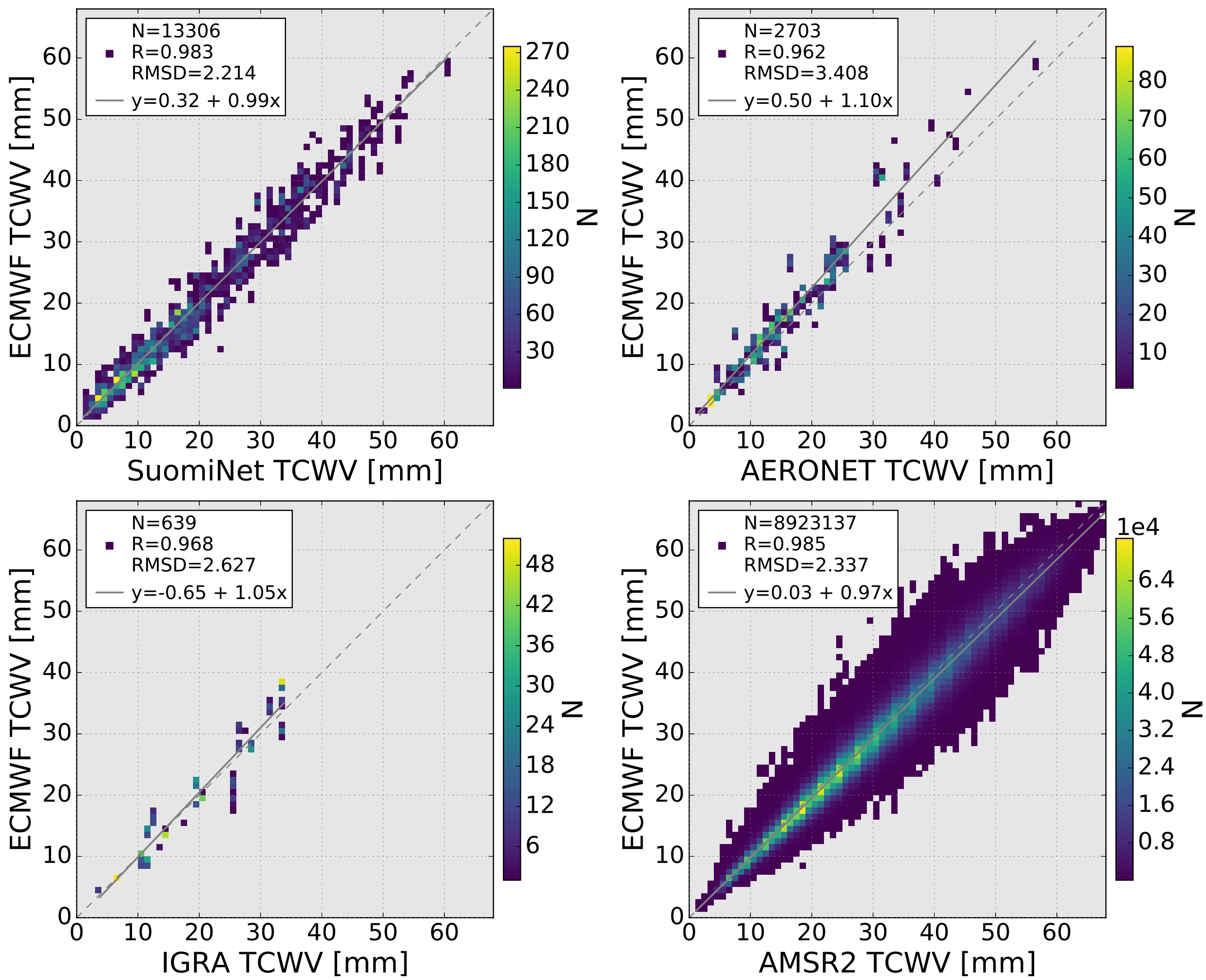

Figure A.6: Heatmap comparison of ECMWF TCWV to SuomiNet, AERONET, IGRA, and AMSR2 TCWV measurements.

Table A.4: ECMWF TCWV Validation

Validation	Mode	N	Surface	Bias (mm)	σ (mm)	$\sigma\mu$ (%)	RMSD (mm)
SuomiNet	N&G	13306	Land	0.11	2.21	12.4	2.21
	N	8026	Land	-0.16	1.98	12.3	1.99
	G	5280	Land	0.53	2.46	12.0	2.51
	T	24787	Land	-0.15	0.93	7.5	0.94
AERONET	N&G	2703	Land	2.07	2.70	15.4	3.41
	N	1365	Land	1.92	2.54	14.7	3.18
	G	1338	Land	2.24	2.86	16.0	3.63
	T	34223	Land	0.12	1.73	12.9	1.74
IGRA	N&G	639	Land	0.43	2.59	12.8	2.63
	N	416	Land	1.04	2.73	14.8	2.93
	G	223	Land	-0.70	1.82	7.8	1.95
AMSR2	G	8923137	Ocean	-0.74	2.22	7.6	2.34

In addition to ECMWF, MERRA-2 was also found to have worse error statistics than OCO-2, relative to the validation sources. We found RMSDs of 2.8 mm, 3.4 mm, 3.3 mm, and 2.8 mm relative to SuomiNet, AERONET, IGRA, and AMSR2, respectively (Figure A.7 and Table A.5). A summary of the RMSDs between MERRA-2, ECMWF, and OCO-2 and the four validation sources is shown in Figure A.8.

Table A.5: MERRA-2 TCWV Validation

Validation	Mode	N	Surface	Bias (mm)	σ (mm)	$\sigma\mu$ (%)	RMSD (mm)
SuomiNet	N&G	10827	Land	0.75	2.65	14.0	2.75
	N	6881	Land	0.43	2.35	13.6	2.39
	G	3947	Land	1.29	3.03	13.8	3.29
AERONET	N&G	2003	Land	1.84	2.90	16.2	3.43
	N	1160	Land	1.66	2.48	14.8	2.98
	G	843	Land	2.10	3.37	17.3	3.97
IGRA	N&G	584	Land	-0.80	3.19	16.1	3.29
	N	382	Land	-0.50	3.54	20.1	3.58
	G	202	Land	-1.39	2.28	9.5	2.67
AMSR2	G	8853389	Ocean	-0.32	2.81	9.5	2.83

Regional biases were difficult to examine for SuomiNet, AERONET, and IGRA due to their limited global coverage. The comparison of OCO-2 to AMSR2, however, showed small latitudinal biases (<5%) in TCWV, with AMSR2 having larger TCWV values, especially in the tropics and

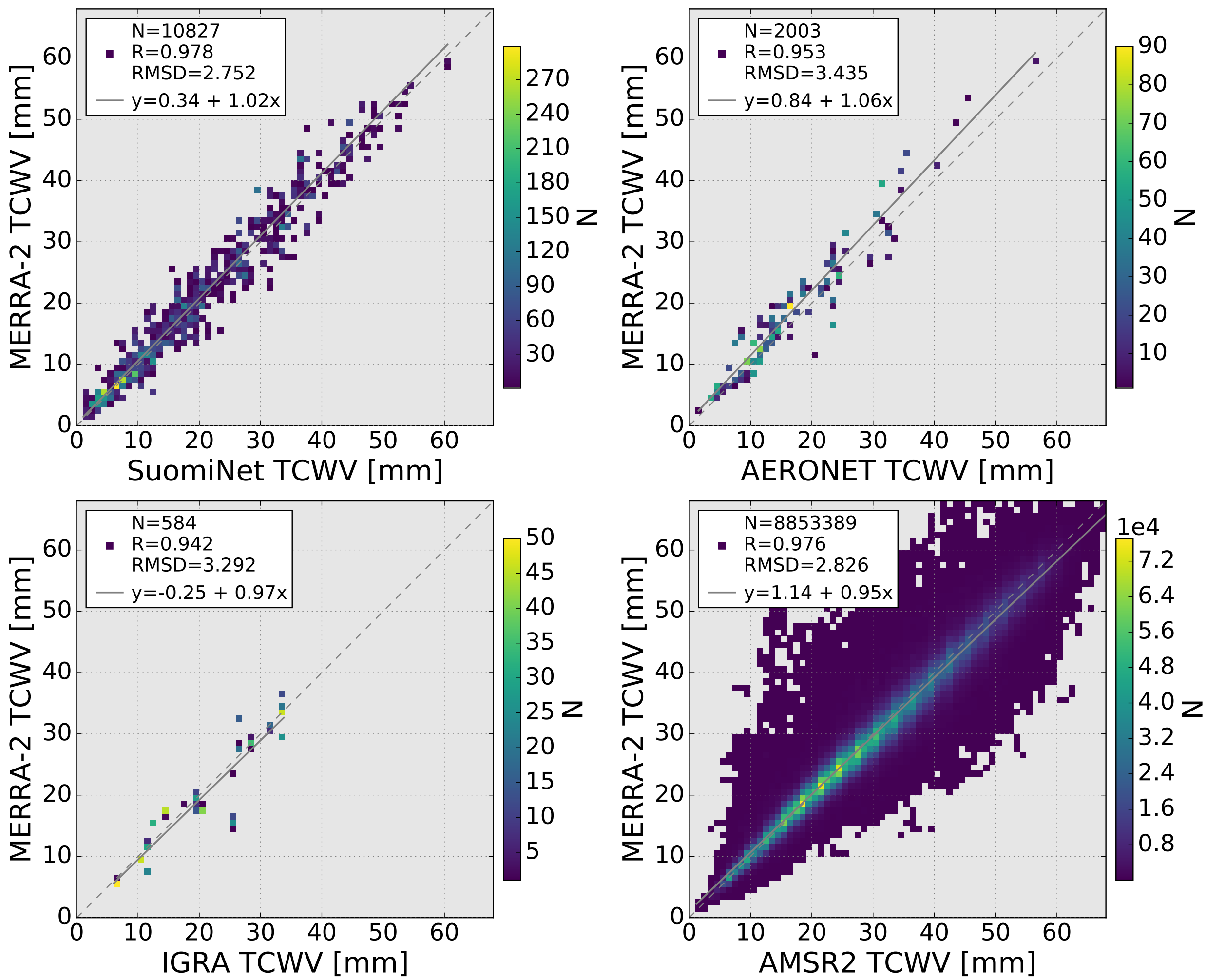

Figure A.7: Heatmap comparison of MERRA-2 TCWV to SuomiNet, AERONET, IGRA, and AMSR2 TCWV measurements.

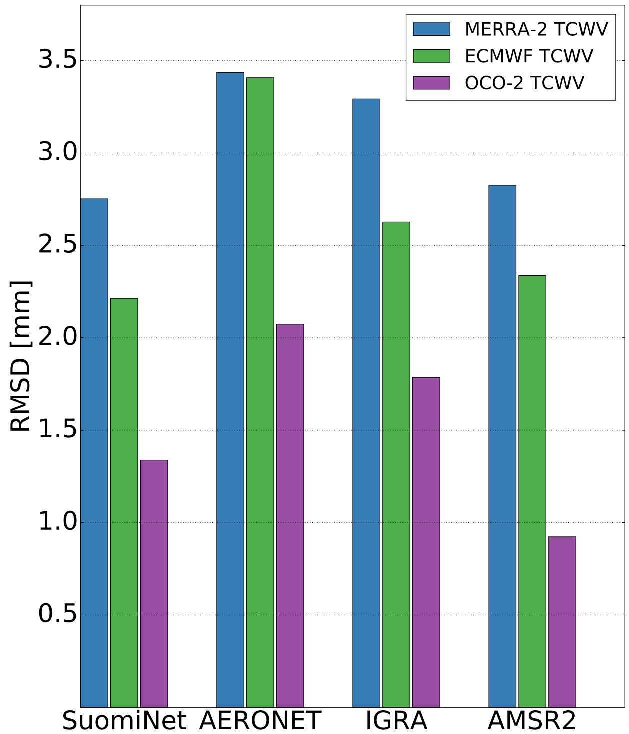

Figure A.8: RMSD between MERRA-2, ECMWF, and OCO-2 TCWV and all four validation sources: SuomiNet, AERONET, IGRA, and AMSR2.

far southern latitudes (Figure A.9). Additional study is needed to identify the source of these differences.

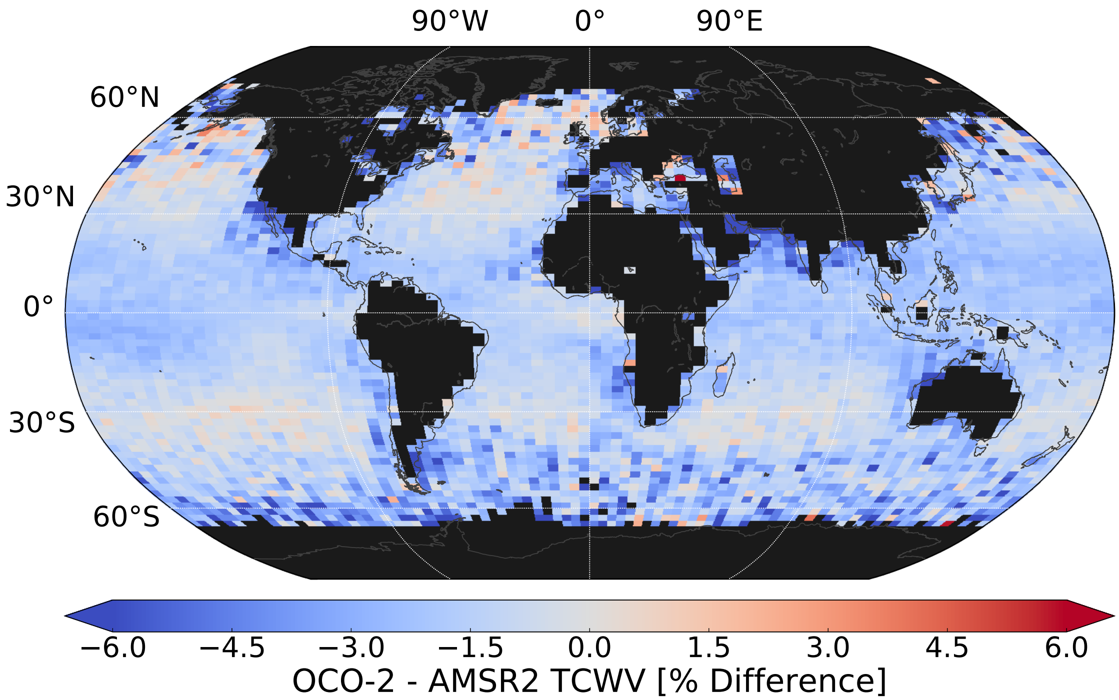

Figure A.9: 2°x4° binned percent difference in TCWV between OCO-2 (E1) and AMSR2 (E2): ((E1 - E2)/(0.5 * (E1 + E2)) * 100). Black grid cells contain no data.

Finally, our results were not significantly dependent on the observation mode (nadir, glint, target) of OCO-2 nor were they dependent on the quality flag (a binary flag derived from several metrics, which indicates the overall quality of the final $X_{\mathrm{CO_2}}$ product) or warn level. For example, the RMSD between OCO-2 and SuomiNet TCWV for all quality flags is 1.38 mm, compared to 1.34 mm for only "good" quality flags. This indicates that potentially many more OCO-2 measurements with "low quality" $X_{\mathrm{CO_2}}$ values may still have a TCWV measurement with comparably small errors. This is partly because the precision requirements for TCWV are less stringent than $X_{\mathrm{CO_2}}$, i.e. about 1 part in 10-60 (1 mm precision for a typical range of TCWV values) vs. 1 part in 200 for $X_{\mathrm{CO_2}}$ (2 ppm precision for typical $X_{\mathrm{CO_2}}$ values).

A.5 Water Vapor Conclusions

Our initial analysis of retrievals performed on synthetic measurements demonstrated that ACOS can accurately retrieve TCWV in simulated conditions and that improvement over the prior in real retrievals is to be expected. The comparison of OCO-2 TCWV measurements to four independent validation sources revealed that OCO-2 is able to accurately and precisely measure TCWV. Small biases and standard deviations were found when OCO-2 TCWV was compared to SuomiNet, IGRA, and AMSR2, while it was found that AERONET may have a mean low bias of approximately 1.4 mm (7%). This is approximately in agreement with the 5-6% low bias in AERONET found by [148]. The small biases between OCO-2 and SuomiNet (+0.34 mm), IGRA (+0.41 mm) and AMSR2 (-0.44 mm) may partly be a result of biases in SuomiNet, IGRA and AMSR2 themselves, as absolute water vapor calibration is difficult to achieve. However, these bias and scatter estimates, comprised of errors in OCO-2, errors in the validation sources, and spatial and temporal co-location errors, still provide a useful upper limit on the true OCO-2 TCWV errors. Using the most accurate validation source over land (SuomiNet) and our sole validation source over ocean (AMSR2) leads to a TCWV RMSD upper limit of 0.9-1.3 mm. This range is larger than that predicted by our simulated tests. Potential reasons for the larger TCWV RMSDs between OCO-2 and the validation sources include imperfect spectroscopy, aerosol and cloud contamination, other forward model errors, and co-location errors. The comparison of OCO-2 to the four validation sources suggests that the error statistics of the OCO-2 TCWV product are not substantially different over land and ocean. This is in contrast to other operational instruments that perform poorly over certain surface types. MERIS, for example, is sensitive to aerosols and their distribution over ocean surfaces, which can result in large errors ($\geq$5 mm, [124]). OCO-2, however, is able to continuously view sun-glint during its orbits over ocean, resulting in high signal-to-noise ratios and thus less sensitivity to aerosol layers.

As this study was done with the operational ACOS algorithm, which was designed for CO_2 and only contained H_2O as an ancillary product, improvements specifically related to water vapor might enable even more accurate H_2O retrievals from OCO-2. Upgrades to the water vapor spectroscopy, improved aerosol parameterizations, and more elaborate water vapor retrieval schemes could all result in more information about water vapor being extracted from the measured radiances. For example, above-cloud retrievals of water vapor are likely possible with OCO-2, which would vastly increase the number of valid measurements (as cloudy scenes are currently screened out). This analysis, however, is beyond the scope of this study.

Our results give evidence that OCO-2 may be accurate enough to be used as a validation source for reanalysis products as well as other methods of measuring TCWV (e.g. MODIS, MERIS, the Suomi National Polar-orbiting Partnership, AIRS, IASI). Additionally, OCO-2 coverage, while limited by its narrow yet dense ground-track, covers both land and ocean over much of the low- and mid-latitudes. This means these TCWV measurements may be useful in improving numerical weather prediction models, which are dependent on the assimilation of accurate water vapor measurements. However, further work must be done to determine if measurements from OCO-2 can provide water vapor information not already measured by other instruments. Besides showing how OCO-2 is able to improve upon the ECMWF prior, we also briefly compared the MERRA-2 reanalysis product to our validation sources and found that OCO-2 would be able to improve upon MERRA-2 as well. These model RMSDs, visualized in Figure A.8, are considerably larger than the RMSDs between OCO-2 and the validation sources, which provides additional evidence that OCO-2 TCWV measurements may be useful for numerical weather prediction and data assimilation applications over land and ocean.

The results of this study show that OCO-2 is the first space-based instrument to accurately measure the most important natural greenhouse gas (water vapor) simultaneously with the most important anthropogenic greenhouse gas (carbon dioxide) [149], at high spatial resolution (1.3x2.3 km^2). These OCO-2 TCWV measurements may be useful regarding the improvement of numerical weather prediction models and reanalysis products along with acting as a validation source for other instruments. Additionally, future satellites with OCO-2-like capabilities, such as OCO-3, MicroCarb, GOSAT-2, and GeoCarb, may be able to measure water vapor with the same or better accuracy than OCO-2.